UNIVERSITY OF LIVERPOOL

Development and Application of Lattice Boltzmann Method for Complex Axisymmetric Flows

Thesis submitted in accordance with the requirements of the University of Liverpool for the degree of Doctor in Philosophy

by

Wei Wang (BEng, MSc)

January 2015

Abstract

The lattice Boltzmann method (LBM) has become an effective numerical technique for computational fluid dynamics (CFD) in recent years. It has many advantages over the conventional computational methods like finite element and finite difference methods. The method is characterised by simplicity, easy treatment of boundary conditions and parallel feature in programming that makes it ideal for solving large-scale real-life problems. This thesis presents the development and applications of a lattice Boltzmann model for both steady and unsteady two-dimensional axisymmetric flows. The axisymmetric flows are described by three-dimensional (3D) Navier-Stokes equations, which can be solved by three-dimensional (3D) lattice Boltzmann method. If cylindrical coordinates are applied, such 3D equations become 2D axisymmetric flow equations. However, they cannot be solved using the 2D standard LBM. In order to study more complicated axisymmetric flow problems by 2D LBM, in this thesis, firstly, the revised axisymmetric lattice Boltzmann D2Q9 model (AxLAB®) is applied and tested for some benchmark for axisymmetric laminar flows and more complicated flows including 3D Womersley flow and forced axisymmetric cold-flow jets, and flows with swirl such as the cylindrical cavity flows and the swirling flow in a closed cylinder with rotating top and bottom. Secondly, the AxLAB® is extended to simulate turbulent flows and non-Newtonian fluid flows. A well-known power-law scheme is incorporated into the AxLAB® to simulate the non-Newtonian fluid flow: the Taylor Couette flows for Newtonian and non-Newtonian fluids are simulated and compared. The combined effects of the Reynolds number, the radius ratio, and the power-law index on the flow characteristics are analysed and compared with other literatures. All the numerical results are also compared with the existing numerical results or experimental data reported in the literature to demonstrate the accuracy of the model. Thirdly, a further developed AxLAB® is presented to simulate the turbulent flows. The turbulent flow is efficiently and naturally simulated through incorporation of the standard subgrid-scale stress (SGS) model into the axisymmetric lattice Boltzmann equation in a consistent manner with the lattice gas dynamics. The model is verified by applying it

to several typical cases in engineering: (i) pipe flow through an abrupt axisymmetric constriction, (ii) axisymmetric separated and reattached flow and (iii) pulsatile flows in a stenotic vessel. All the numerical results obtained using the present methods are compared with experimental data and other available numerical solutions, indicating good agreements. This shows that the improved AxLAB® is simple and is able to predict axisymmetric turbulent, non-Newtonian complicated flows at good accuracy.

Acknowledgement

I would like to express my sincere thanks to my supervisor, Dr. Jian Guo Zhou, for his encouragement, guidance and support to me throughout the PhD project. His patience, motivation, enthusiasm and immense knowledge not only helped me in all stages of the research and writing up of the PhD thesis, but also set an example that I aim to achieve some day.

It has been a pleasure to share time with my office mates, Li Yaru, Yin Yue, Zheng Peng and Li Xiaorong for their helpful discussions and enjoyable time during the long hours in the office.

My deepest gratitude goes to my parents, my wife and my daughter who are the source of my strength. Without their encouragement, understanding and love, it would have been impossible for me to complete this work.

Finally, I would like to thank all who have supported me during my PhD study.

Publications

1. W. Wang and J. G. Zhou. Lattice Boltzmann Method for Axisymmetric Turbulent Flows. *International Journal of Modern Physics C*, **26**(9): 1550099, 2015.

2. W. Wang and J. G. Zhou. Enhanced Lattice Boltzmann Modelling of Axisymmetric Flows. *Proceedings of ICE: Engineering and Computational Mechanics*, **167**: 156-166, 2014.

3. W. Wang and J. G. Zhou, Simulations of Taylor Couette flow and Cold-flow Jets using an axisymmetric lattice Boltzmann method. *35th IAHR World Congress*, Chengdu, China, 2013.

Contents

List of Figures

List of Tables

List of Abbreviations and Symbols

Abbreviations

1D	One dimensional
2D	Two dimensional
3D	Three dimensional
AxLAB	Axisymmetric lattice Boltzmann method by Zhou.
AxLAB®	Revised Axisymmetric lattice Boltzmann method by Zhou.
BGK	the single time relaxation approximation designed by Bhatnagar, Gross and Krook
BGK-LBM	Lattice Boltzmann method using BGK scheme
CFD	Computational fluid dynamics
CBE	The continuous Boltzmann equation
CA	Cellular automata
D2Q4	4-speed square lattice
D2Q7	7-speed square lattice
D2Q9	9-speed square lattice
DNS	Direct numerical simulation
FDM	Finite difference methods
FEM	Finite element methods
FH	Method proposed by Filippova and Hanel
FHP	Model designed by Frisch, Hasslacher and Pomeau

FVM	Finite volume methods
HPP	Model designed by Hardy, de Pazzis and Pomeau
LABSWE	The lattice Boltzmann model for shallow water equations
LABSWE^{TM}	The lattice Boltzmann model for shallow water equations with turbulence modelling
LABSWE^{MRT}	The lattice Boltzmann model for shallow water equations with multiple relaxation-time
LBM	Lattice Boltzmann method
LES	Large-eddy simulation
LGA	Lattice gas automaton
LGCA	Lattice gas cellular automata
MRT	Lattice Boltzmann method with multiple-relaxation-time
N-S	Navier-Stokes
PDF	Particle Distribution Function
SGS	Subgrid-Scale Stress model

Symbols

n_α	is a Boolean variable,
Ω_α	is the collision operator,
M	is the number of directions of the particle velocities at each node,
p	is the pressure,
i , j	are space direction indices,

f_i	is the body force per unit,
e_r, e_φ, e_z	are the standard orthonormal unit vectors,
φ	is the azimuth,
r, x	are the index standing for the coordinates in radial and axial directions,
δ_{ij}	is the Kronecker function,
k	is the turbulent kinetic energy ,
ε	is the turbulent dissipation rate,
$\overline{u_i}$	is the space-filtered velocity component in i direction,
G	is a spatial filter function,
τ_{ij}	is the subgrid-scale,
v_e	is the eddy viscosity,
C_s	is the Smagorinsky constant,
l_s	is the characteristic length scale,
S_{ij}	is the magnitude of the large scale strain-rate tensor,
$\overline{u_i' u_j'}$	is the Reynolds stress tensor,
f_α	is the distribution function of the particles,
f'	is the value before the stream,
e_α	is the velocity vector of a particle in the α link,
Δt	is the time step,

x is the space vector,

Δx is the lattice size,

f_{α}^{eq} is the local equilibrium distribution function,

ζ is a relaxation time,

f^{eq} is the Maxwell-Boltzmann equilibrium distribution function,

ω_{α} is the weight,

θ is the source or sink term,

F_i is the force term,

$e_{\alpha i}$ is the component of e_{α}, which is the velocity vector of a particle in the α link,

τ_{α} is the relaxation time,

ν is the Newtonian fluid kinematic viscosity,

τ is the Newtonian fluid relaxation time,

ν_{tm} is the non-Newtonian fluid kinematic viscosity,

τ_{tm} is the non-Newtonian fluid relaxation time,

γ is the local shear rate,

n is the power-law exponent,

ρ is the fluid density,

u_i is the velocity,

F_{it} is the force term of non-Newtonian fluid,

τ_t is the relaxation time for turbulent flow,

τ_e is the eddy relaxation time,

τ_f is the wall shear stress vector,

C_f is the friction factor at the wall,

τ_{fi} is the wall shear stress,

$\overline{f_a}$ is the distribution function,

$\overline{f}_a^{eq}$ is the local equilibrium distribution function,

S_ϕ is the source or sink term,

$\bar{e}_a$ is the velocity vector of a particle on the D2Q4,

$\overline{\tau_a}$ is effective relaxation time for rotation fluid,

$\bar{\tau}$ is the Newtonian fluid relaxation time for rotation fluid,

$\overline{\tau_t}$ is the non-Newtonian fluid relaxation time for rotation fluid,

u_ϕ is the azimuthal velocity,

η is the radius ratio,

Γ is the aspect ratio,

H is the height of the cylinder,

ξ is the ratio of angular velocities

R_1 is the radius of the inner cylinder,

D_w is the gap between inner and outer cylinders,

Re	is the Reynolds number,
Re_c	is the critical Reynolds number,
Ta	is the Taylor number,
Ta_c	is the critical Taylor number,
U_0	is the jet exit axial velocity,
D	is the jet diameter,
A	is the forcing amplitude,
f	is the frequency,
e_x, e_y	is the particle velocity in the x and y directions respectively,
α	is the Womersley number.

Chapter 1: Introduction and Literature Review

1.1 Background

Fluid flows play an important role in human's daily life, such as the water flow in rivers, air movement in the atmosphere, the ocean currents and the blood flow in human body are all the common fluid flow phenomena. Many researchers aim to find out the rules which in the fluid flows in last few decades. Fluid flows obey the conservations of mass and momentum. Based on these conservation laws, a set of differential equations can be derived to represent fluid flow motions. The most important dynamic theories are the continuity equation and the Navier-Stokes (N-S) equations which have been established to describe the flow characters in the middle of 19^{th} century. However, for the general governing equations, there is no analytical solution except for some simple situations. Till 1940s, the modern computer techniques developed quickly, people started to use computer to numerically solve the equations and to study the fluid system. At the meantime, the computational fluid dynamics (CFD) methods, such as finite difference method (FDM) and finite volume method (FVM), have been developed to solve the Navier-Stokes equations numerically. Each of them has its own advantages. For example, FDM has two advantages compared with FEM: firstly, it is generally faster than the FEM for a similar case, which is more obvious for three-dimensional calculations [1]; secondly, it generally does not suffer from the local mass conservation problem, which is often observed in a finite element model [2]. On the other hand, The FEM adopts the unstructured grids which can fit complex and irregular geometries more easily than the FDM. Therefore, the FEM can reduce the number of grids significantly with the similar accuracy for flows in complicated geometries. The FVM is also popular for solving the axisymmetric flow equations. The construction of FVM methods capable to deal with unstructured meshes can be of utmost importance in order to handle problems that involve complex geometries [3]. Murthy and Mathur extended the FVM to compute radiation in axisymmetric geometries using unstructured polyhedral meshes [4]. The node-centered FVM using an edge-based data structure, which was presented in Lyra *et al.* [5] is very flexible to deal with control volumes of different shapes associated to generic unstructured meshes. These

CFD methods can solve the N-S equations directly and some macro variables such as velocity and pressure can be obtained as well. It should be noticed that these conventional CFD methods are based on the discretisation of macroscopic continuum equations at the macroscopic level.

It is well known that the fluid is composed of a huge number of atoms and molecules at the microscopic level. By modeling the motion of individual molecule and interactions between molecules, the behavior of fluid can be simulated. However, this microscopic computation method needs much more time than the traditional CFD method at macroscopic level because it has to calculate a huge number of the molecules motions. That is the drawback of this method. Between these two calculation scales, there is an intermediate scale that is named the mesoscopic scale, which can also be used to simulate the fluid system and other physical phenomena. This idea considers a much fewer number of fluid 'particles' than molecular dynamics method. In other word, a fluid 'particle' is a large group of molecules. Moreover, the size of the fluid 'particle' is still smaller than the smallest length scale of the macroscopic simulation for the right macroscopic physical properties.

Using such scale, a cellular automata concept was developed by Ulam, von Neumann and Zuse in the late 1940's [6]. Since then, it has been further developed and it has now become a very powerful tool in simulating various scientific problems [7, 8]. Zuse presented an idea concerning the wide applications of cellular automata (CA) to physical problems in a monograph [9]. Hardy *et al*. proposed some formulations of HPP (Hardy, de Pazzis and Pomeau) lattice gas cellular automata in 1973 [10]. Since then, both one and two-dimensional CA have been investigated. Typical ones are Wolfram's four universal classes CA, Fredkin's game, etc. The two-dimensional "Game of Life" is well known, which was introduced by Conway in the 1970's [11]. This demonstrates the most important feature of the CA: with extremely simple rules; a CA can be used to simulate some complex physical problems in the real world. Actually, many applications have shown that CA is a very simple method to a wide variety of complicated phenomena [6, 12, 13].

1.2 Lattice Gas Automata

A lattice gas automata (LGA) is a particular class of the cellular automata. It is based on a simple model based on fully discrete microscopic space, time and particle velocities that reside on regular lattices [14]. Such particles move from one lattice unit to other lattice in their directions at their own velocities. Two or more particles arriving at the same place can collide. The important property of the LGA is that the mass and momentum are explicitly conserved, which is a significant feature in simulating real physical problems. In fact, the summations of the micro-dynamic mass and momentum equations can be asymptotically equivalent to the Navier-Stokes equation for incompressible flows [14].

The first fully discrete model for a fluid was developed by Hardy *et al*. [10] on a square lattice (HPP model), which is the most simple LGA model for two-dimensional flows. But the N-S equations cannot be recovered from this model using the HPP due to the insufficient symmetry of the lattice. After that, Frisch *et al*. [15] proposed a corrected lattice gas automaton (FHP model) in 1986, which can recover the N-S equations (see Fig. 1.1).

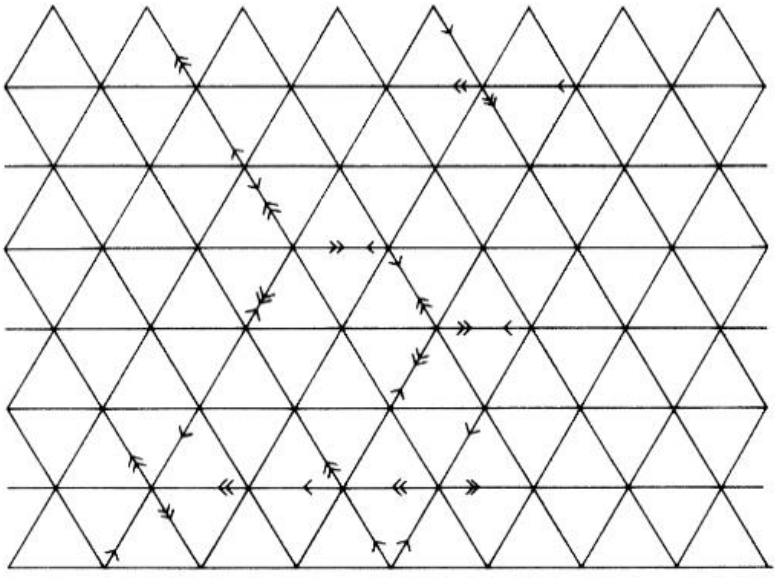

Figure 1.1 Lattice for FHP model.

Generally, the LGA has two sequence steps: streaming step and collision step. In streaming step, each particle moves to the nearest node along the directions at its own velocity. Then, when the particles arriving at one node and their velocity directions were changed according to the assumed rules; and the collision happens. These two steps will simulate convection and diffusion respectively at macroscopic level in physics.

The LGA equation can be written as:

$$n_\alpha\left(x+e_\alpha,t+1\right)=n_\alpha\left(x,t\right)+\Omega_\alpha\left[n\left(x,t\right)\right],\qquad \alpha=0,1,...,M, \tag{1.1}$$

where n_α is a Boolean variable that is used as an indication of the presence with $n_\alpha=1$ or absence with $n_\alpha=0$ of particles, t is the time, e_α is the local constant particle velocity, Ω_α is the collision operator, and M is the number of directions of the particle velocities at each node.

The physical variables, density and velocities are defined by

$$\rho=\sum_{\alpha=0}^{M}\langle n_\alpha\rangle, \tag{1.2}$$

$$u_i=\frac{1}{\rho}\sum_{\alpha=0}^{M}\langle n_\alpha\rangle e_{\alpha i}. \tag{1.3}$$

in which $\langle n_\alpha\rangle$ indicates the ensemble average of n_α in statistical physics.

The LGA for the Navier-Stokes equations has several drawbacks, such as the non-isotropic advection term, spurious invariants, numerical noise *etc*. [16]. As a result, researchers were keen to find a method to treat these drawbacks and the lattice Boltzmann model was developed in such background.

1.3 Lattice Boltzmann Methods

The Lattice Boltzmann method is evolved from LGA to overcome its drawbacks. Its basic difference from LGA is in that Boolean variable is replaced by particle distribution functions, i.e. $\langle n_\alpha \rangle = f_\alpha \ \left(f_\alpha \geq 0 \right)$. If individual particle motion and particle-particle correlations are neglected, Eq.(1.1) can be replaced by the following lattice Boltzmann equation [17],

$$f_\alpha \left(x + e_\alpha, t+1 \right) = f_\alpha \left(x,t \right) + \Omega_\alpha \left[f\left(x,t \right) \right], \qquad \alpha = 0,1,...,M. \tag{1.4}$$

Such approach eliminates the statistical noise in a LGA and retains all the advantages of locality in the kinetic form of a LGA [8]. According to the above definition, the fluid density and velocity can be obtained from

$$\rho = \sum_{\alpha=0}^{M} f_\alpha, \tag{1.5}$$

$$u_i = \frac{1}{\rho} \sum_{\alpha=0}^{M} e_{\alpha i} f_\alpha. \tag{1.6}$$

The lattice Boltzmann method (LBM) is a relative new numerical method for simulating complex flows via an indirect solution to the incompressible Navier-Stokes (N-S) equations [19,20]. It has been applied in different areas [18,21,22], which show its efficiency, accuracy and capabilities. The method has many advantages over the conventional computational methods like the finite difference method and finite volume methods. Although it is originally developed to simulate fluid flows described by the Navier-Stokes equations, it has been extended to solving many other flow problems in science and engineering. For instance, Chang and Yang [23] proposed a lattice Boltzmann model for image denoising; Mendoza *et al*. [24] applied the method to simulate the relativistic fluids; Swift *et al*. [25] used the lattice Boltzmann method to present the nonideal fluids; and Zhou developed the lattice Boltzmann method for shallow water flows [26] and groundwater flows [27]. Moreover, Love and Donato [28] has extended the lattice gas automaton to simulate fluids on arbitrary surfaces. Mendoza *et al*. [29] developed a new lattice kinetic method to simulate fluid dynamics in curvilinear geometries and curved spaces. Klales *et al*. [30] present a

hydrodynamic lattice gas model for two-dimensional flows on curved surfaces with dynamical geometry. Mendoza *et al*. [31] developed and validated a new lattice Boltzmann model for the transport properties of campylotic media. He and Doolen [32] extended the lattice Boltzmann method to general curvilinear coordinate systems by using an interpolation-based strategy.

Unlike traditional CFD methods (e.g., FDM and FVM), LBM is based on the microscopic kinetic equation for the particle distribution function (PDF) and the macroscopic variables are defined from the PDF. The LBM have several advantages: first, it is simple to program. Since the simple streaming step and collision step can recover the non-linear macroscopic advection terms, basically, only one loop of the two simple steps is implemented in LBM programs. Moreover, in LBM, the pressure satisfies a simple equation of state when simulate the incompressible flow. Hence, it is not necessary to solve the Poisson equation by the iteration or relaxation methods as common CFD method when simulate the incompressible flow. The explicit and non-iterative nature of LBM makes the numerical method easy to parallelize [33]. On the other hand, LBM also have some drawbacks like other CFD methods. For the present LBM, most of calculations focus on low-velocity flows; more complex flows need to add extra calculation terms, such as multiphase flows and porous flows, which are still in process by the researchers.

1.4 Axisymmetric Lattice Boltzmann Method (AxLAB®)

As lots of axisymmetric flows occur in practical engineering [34], the study on how to apply the LBM to axisymmetric flows has been reported. The three-dimensional (3D) lattice Boltzmann method was developed to simulate 3D axisymmetric flows [35,36,37] using the cubic lattices, in which a curved boundary condition was treated. In theory, the 3D Navier-Stokes (N-S) equations for axisymmetric flows can be simplified to 2D flow equations in the cylindrical polar system. This makes it possible to develop a simpler lattice Boltzmann method for 3D axisymmetric flows, which will greatly reduce the computational time. To take the full advantage of this feature, appropriate source term may be added to the LBE for the Navier-Stokes equations to model axisymmetric flow. In order to mimic the additional axisymmetric contributions to 2D Navier-Stokes equations in cylindrical coordinates, several spatial

and velocity-dependent source terms were proposed to insert into the standard lattice Boltzmann equation (LBE) [38,39,40]. This is the basic idea behind the method of Halliday *et al*. [41], where they first developed the lattice Boltzmann method for axisymmetric flows through the introduction of two source terms into the lattice Boltzmann equation and recovered the macroscopic hydrodynamic equations. This method has successfully been applied to a number of axisymmetric flow problems [42,43,44]. Later, other researchers also derived modified LBMs following the same procedure of Halliday *et al*. [45,46]. The revised axisymmetric model proposed by Lee can recover the axisymmetric flow equations correctly [44]. Recently, Chen *et al*., [47] used the vorticity-stream-function equations to develop an axisymmetric lattice Boltzmann method, making the formulation satisfy the continuity equation and easy to solve. Guo *et al*., [48] described an axisymmetric lattice Boltzmann model from the continuous Boltzmann-BGK equation in cylindrical coordinates, which is a complete lattice Boltzmann model for the axisymmetric flows with or without rotation in the framework of the lattice Boltzmann method. An improved axisymmetric lattice Boltzmann scheme has been formulated by Li *et al.*, [49], which includes the rotation effect.

More recently, Zhou [50] has improved on his earlier proposed axisymmetric lattice Boltzmann method (AxLAB) [51] to model general axisymmetric flows with or without rotation, which is named AxLAB® for an axisymmetric lattice Boltzmann model revised. The AxLAB® is simple and efficient without involving calculations of a derivative and suitable for studying complex axisymmetric flows with or without swirling effect. Unlike other existing methods, all the macroscopic variables such as velocities and density are determined in the same formulas as those in the standard lattice Boltzmann approach to the Navier-Stokes equations, and furthermore, any additional force terms can be easily and directly added to the model without a modification with similar features to the standard lattice Boltzmann Method for the N-S equations. This makes the model efficient to model general incompressible axisymmetric flows.

However, most axisymmetric lattice Boltzmann methods in literatures are reported for laminar axisymmetric flow equations without the flow turbulence. As most practical flows in nature are turbulent, these methods cannot be directly applied. Generally,

flow turbulence can be modelled by using additional scheme such as the $k-\varepsilon$ model, giving the time-averaged properties. Teixeira [52] presented a lattice Boltzmann method for turbulent flows: the single relaxation time is modified as a variable relaxation time which is decided by solution of the two differential equations, $k-\varepsilon$ equations. As an alternative method, the large eddy simulation can efficiently simulate vorticity larger than a prescribed scale, where space-filtered governing equations with a subgird-scale (SGS) stress model for the unresolved scale stress are used. Usually, the Smagorinsky [53] subgird-scale is applied to simulate flow turbulence in the space-filtered governing equations, which turns to be the simplest and most accurate for turbulence flows. According to the research by Tutar and Hold [54], the space-filtered flow equations are more accurate than the time-averaged ones for the calculation of turbulent flows and so are used in the present study. Hou *et al*. [55] demonstrate that the standard Smagorinsky SGS stress model can be incorporated into the lattice Boltzmann method for turbulence modelling. Meantime, the single relaxation time is modified as a variable relaxation time which is directly linked with the distribution function and can be eliminating any calculations of derivatives. Following the similar idea to Hou *et al*., Zhou has developed a lattice Boltzmann model for the shallow water equations with turbulence modelling (LABSWE^{TM}) [56], demonstrating its power and applicability for turbulence modelling [57].

1.4.1 Study of Pulsatile Flow

In fluid dynamics, a flow with periodic variations is known as pulsatile flow. Researching the pulsatile flow is one of the most attractive research projects in the axisymmetric flow study, especially for the blood flow. The blood transports particles such as red and white blood cells through a complicate network of elastic branching tubes. The blood flow is becoming a great interest research project in the cardiovascular doctors and fluid dynamicists since the deaths of the cardiovascular diseases increase rapidly in the world. Lots of blood problems are due to the abnormal blood flow in arteries. Once the stenoses block more than about 70% of the artery, it is a significant health problem for the patient. The blood flow to the brain and heart will be blocked when the blood clots exist in the main arteries. It is necessary to carry

out experiment and numerical studies to further investigate the flow characters in stenosed artery.

Generally, most of literatures studies for the blood flow come from the experiments. Experiments have been carried out for a local stenosis and steady flow [58,59] or unsteady flows [60]. Then, experimental observations for both steady and unsteady flow through furrowed channels have been presented [61]. Computational methods of the steady flow including analytical solutions for the flow in a continuously perturbed conduit [62] and numerical solutions in locally constructed two-dimensional channels [63] or cylindrical pipes [64]. The pulsatile flow has also been treated numerically for local stenoses and two-dimensional channels [65]. Young and Tsai carried out more experimental studies for the steady and unsteady flows through rigid stenosed tubes with different constriction ratios [66]. However, accurate measurements of distance from the wall and the shape of the velocity profile are technically difficult for pulsatile flow. Moreover, shear stress measurement also depends on the near-wall blood viscosity which is usually not easy to known. Thus arterial wall shear stress measurements are estimated and may have much error.

Therefore, using the numerical methods to investigate the blood flow can overcome the above drawbacks. Since the lattice Boltzmann method (LBM) has advantages such as ease of implementation, ease of parallelization and simple boundary treatments, the LBM may become a useful tool for application in the blood flow. Artoli *et al*. [67] studied the accuracy of two dimensional (2D) Womersley flow by using 2D nine-velocity lattice LBM model. Cosgrove *et al*. [68] also studied the 2D Womersley flow and indicated that the results of LBM incorporating the halfway bounce-back boundary condition are second order in spatial accuracy. Later, Artoli *et al*. [69] obtained some preliminary results for the steady blood flow in a symmetric bifurcation. Actually, the above studies only addressed on simple 2D geometries and it cannot represent the 3D blood tubes.

Maier *et al*. [35] studied the Poiseuille flow in 3D circular tube, and they found that it will cause much error on curved surface when using the simple bounce-back boundary condition. In order to solve this problem, accurate 3D curved boundary treatments were proposed by Mei *et al*. [36] and Bouzidi *et al*. [70]. Besides that, lots

of literatures are written for the pulsatile flow. Beratlis *et al*. [71] presented a closely coupled numerical and experimental investigation of pulsatile flow in a prototypical stenotic site. The pulsatile flow of non-Newtonian fluid in a bifurcation model with a non-planar daughter branch is investigated numerically by Chen and Lu [72], who using the Carreau-Yasuda model to take into account the shear thinning behavior of the analog blood fluid. Li *et al*. investigated the flow field and stress field for different degrees of stenoses under physiological conditions [73].

The studies of 3D pulsatile flow in tubes with different 3D constrictions are necessary to carry out. But the problem is also obviously as the direct 3D simulations of flow in circular tubes [37] are very time-consuming for such an axisymmetric geometry. It is necessary to develop an accurate model to simulate the axisymmetric flow more efficiently. Fang *et al*. [74] studied the pulsatile blood flow in a simple 2D elastic channel. In their study, an elastic and movable boundary condition was proposed by introducing the virtual distribution function at the boundary and some good results were obtained. Guo *et al*. [75] further developed a non-slip wall boundary condition. Later, Fang *et al*. [76] proposed a boundary condition for elastic and moving boundaries and applied to simulate the viscous flow in large distensible blood vessels. Their above results of pulsatile flow are consistent with the experimental data in 3D elastic tubes.

However, the Reynolds number in the above studies are very low and the geometry of study is only 2D. Due to the practical engineering applications, modelling the turbulent axisymmetric flow is necessary.

1.4.2 Study of Rotation Flow

Axisymmetric flows with swirl or rotation played an important role in engineering practice [77,78]. At the meantime, the flows with swirl or rotation have more complex property than the axisymmetric flow without swirl. The flow in a closed cylindrical container with a rotating top has been studied both experimentally and numerically for several decades. The first set of experiments was carried out by Vogel [79] in 1968.

And then, Ronnenberg [80] and Escudier [81] took some experiments to observe the flow produced in cylindrical container by a rotating end wall, in which they found the formation of a concentrated vortex core along the center axis. Based on their research work, many experimental and numerical studies have been carried out later. Spohn *et al*. [82] experimentally studied the vortex breakdown bubbles which appeared in steady-state flow in a closed cylindrical container with the rotating bottom. Details of the flow were visualized by means of the electrolytic precipitation technique, whereas a particle tracking technique was used to characterize the whole flow field. Later, Sotiropoulos *et al*. [83] carried out the first experiment to verify their early numerical findings which show the existence of chaotic behavior in the Lagrangian transport with the vortex-breakdown bubbles for flows are steady. In the computations, numerous cylindrical problems were investigated. Lopez [77,84,85] published three papers to investigate the axisymmetric vortex breakdown from 1990 to 1992. Sotiropoulos *et al*. [86,87] studied three-dimensional structure of confined swirling flows with vortex breakdown in 2001. Apart from the one side rotation, people find two sides rotation can give new insight to the problems and give some new ideas on how to control the vortex. The influence of co- and counter-rotation of the other end wall of the cylinder on vortex breakdown was studied experimentally by Bar-Yoseph *et al*. [88] Gautier *et al*. [89] and Fujimura *et al*. [90]. In computations, Valentine and Jahnke [91] and Lopez [92] studied the case of co-rotating end walls with the same angular velocity for steady and unsteady swirl flow.

The other typical rotation flow is Taylor-Couette flow. The flow moves between two concentric rotating cylinders of infinite length, known as Taylor-Couette flow. This kind of flow has been investigated by many experiments and numerical studies. As we know, Taylor [93] first studied the stability of this viscous flow experimentally and theoretically in 1923. However, the aspect ratio of the annular cavity is not large enough to apply the Taylor-Couette model in practice. The ends effects also played an important role when the aspect ratio reduced. So that the solutions in the annulus of short cylinders may different from the ideal Taylor-Couette model which was presented by Benjamin [94,95]. DiPrima and Eagles [96] have reported the influence of the radius ratio on the stability of the Taylor-Couette flow. When the radius ratio decrease, the number of unstable flow patterns in a fixed Reynolds number decreased rapidly. On the other hand, the rotation speed of the inner cylinder is also need to

study. At low rotational speed of the inner cylinder, the flow is steady and the vortices are planar. Three-dimensional vortices would begin to appear when the speed of rotation exceeds a critical value which depends on the radius ratio of two cylinders. Among these studies, most of them used the conventional Navier-Stokes solvers to studies the Taylor-Couette flow with Newtonian fluid. Recently, the lattice Boltzmann method received much attention from the non-Newtonian fluid dynamics researcher. Yoshino *et al*. [97] proposed a numerical model for non-Newtonian fluid flows based on the LBM. They applied this method to two representative test case problems, power-law fluid flows in a reentrant corner geometry and non-Newtonian fluid flows in a three-dimensional porous structure. Their simulations indicated that this method can be useful for practical non-Newtonian fluid flows. Wang and Bernsdorf [98] used the LBM in the analysis of a blood flow using the Carreau Yasuda model. A comparison has been made between non-Newtonian and Newtonian flows in a three-dimensional (3D) generic stenosis.

Later, several authors developed their own model to study the axisymmetric flows using the LBM. Niu *et al*. [43] developed an extension idea of Halliday *et al*. [41] which include the azimuthal rotation effect in their model. The rotation terms are considered as inertia forces by their methods. Peng *et al*. [42] improved Halliday's method to the axisymmetric thermal systems. Besides the radial and axial velocity components solved by the lattice Boltzmann formulation, the azimuthal velocity component and the temperature are calculated by a finite differences scheme. Moreover, Huang *et al*. [99–103] presented a revised version of the D2Q9 model proposed by He and Luo [104] which improved the numerical stability and to reduce the compressibility effect. They developed a hybrid lattice Boltzmann scheme for axisymmetric flows with the rotation of the inner cylinder. The axial and the radial velocities were solved by inserting source terms into the two-dimensional lattice Boltzmann equation, while the azimuthal velocity and the temperature equations were discretized with a finite difference scheme. More recently, Zhou [51] developed another axisymmetric scheme, suitable for general axisymmetric flows, where the force and source or sink terms were incorporated into the lattice Boltzmann (LB) equation naturally. In 2011, the same author presented a revised axisymmetric lattice Boltzmann method [50]. Later, An *et al*. [105] developed an analytical solution of an axisymmetric lattice Boltzmann model for cylindrical Couette flows for non-

Newtonian fluid. To improve the numerical stability and eliminate the compressibility effect of standard LBM, It is necessary to obtain a more robust incompressible axisymmetric D2Q9 model.

1.4.3 Study of Turbulent Flow

The flow with turbulence is very important in both theoretical and practical study. From the theoretical view, it can be simulated using the Navier-Stokes equations and the continuity equation. However, the most important characteristic of a turbulent flow is the enormous numbers of scales, which is not an easy way for a traditional method to obtain the results. Meanwhile, Tennekes and Lumley [106] summarized a number of characteristics for turbulent flow:

1) Turbulent flow is irregular, random and chaotic, which consists of a spectrum of eddy sizes.

2) The diffusivity in turbulent flow increases with the rise of the Reynolds number Re. That means the exchange of momentum increases.

3) Turbulent flow takes place at high Reynolds number. For example, turbulent axisymmetric pipe flows usually occurs when $Re \geq 4000$ [107], in which $\mathrm{Re} = uD / v.$

4) Turbulent flow is always three-dimensional. But when the governing equations are time-averaged or space-filtered, it can be dominated by two-dimensional characteristics and exists in practice as a two-dimensional flow problem. [106]

5) Turbulent flow is dissipative, as the kinetic energy of the small eddies, which is obtained from larger eddies, is transformed into internal energy. The largest eddies extract the energy from the mean flow. Such process is referred to as a cascade process [106].

6) The flow should still be treated as a continuum in spite of the occurrence of different sizes of eddies.

By using the LBM to solve a high Reynolds number flow, the unresolved small scale effects on large scale dynamic should be added, otherwise the results will be instable. Sterling and Chen [108] reported consistently with this argument and they found the LBM can be viewed as an explicit second-order finite-difference discretization method. In order to extend the LBM to include small scale dynamics for turbulent flows, two methods have been proposed. Because of the LBM was originated from LGA method and the lattice gas dynamics contains small scale fluctuations, so Hou *et al*. [55] suggest the LBM can be used to simulate large scale motions and the lattice gas method can be used to simulate small scale dynamics. The other one is much simple, in which the LBM can be combined with the traditional subgrid model. Benzi *et al*. [109] and Qian *et al*. [110] followed this approach and obtained reasonable results. Among the simplest subgrid models is the standard Smagorinsky model [47], which uses a positive eddy viscosity to represent small scale energy damping. Therefore, Hou *et al*. [55] discussed the traditional subgrid model and incorporated it into the framework of the LBM naturally. Following the similar idea to Hou *et al*., Zhou has developed a lattice Boltzmann model for the shallow water equations with turbulence modelling (LABSWE^{TM}) [56], demonstrating its power and applicability for turbulence modelling [57]. Meantime, lots of other methods have been carried out for the flow turbulence modelling. Krafczyk *et al*. [111] developed a large eddy simulation with a multiple-relaxation-time (MRT) lattice Boltzmann model for the Navier–Stokes equations. Yu *et al*. [112] proposed similar a work and applied the MRT lattice Boltzmann model to simulate turbulent square jet flow.

1.5 Aims and Contributions

In the practical engineering, axisymmetric flows with turbulence are commonly observed. Although the lattice Boltzmann method has developed quickly over the past two decades, it is still a relative new method that unlike the traditional CFD methods. Like all the CFD methods, the LBM also has some drawbacks and needs further improvement. Although the AxLAB® has demonstrated its potential and attractive capabilities in simulating axisymmetric flows, it still needs to be improved and tested for more flow problems.

Therefore, the main contributions of this study are to present and improve the general LBM for axisymmetric flows and apply these models to study the axisymmetric fluid flows. The detailed novelties can be summarized as follows:

1. Presented a general method by inserting proper source terms into the lattice Boltzmann equation this made the model simpler and save the calculation time. In addition, a new simple boundary condition for the distribution function was used to simulate the axisymmetric flows which shown efficiency and accuracy.

2. Developed the AxLAB® model for the non-Newtonian flows like the flow in Taylor-Couette flow.

3. Improved the AxLAB® model for simulation of flow turbulence by combining with the subgrid-scale (SGS) stress model and verify it by simulating different turbulent flows.

1.6 Outline of the Thesis

In Chapter 1, introduces the research background and the history of the lattice Boltzmann method, reviews the development and application of LBM in recent years briefly and outlines the aim and the objectives of this thesis.

In Chapter 2, briefly describes the N-S equations and the various axisymmetric flow governing equations such as laminar flow, turbulent flow.

In Chapter 3, the basic knowledge of lattice Boltzmann methods are introduced. The derivation and theory for the axisymmetric lattice Boltzmann model are presented and two models were described to simulate axisymmetric flows with or without swirl. A brief recovery procedure for the axisymmetric flow equations from the AxLAB® is given.

In Chapter 4, the non-Newtonian fluid simulation was introduced and a general power-law model was suggested for incompressible non-Newtonian fluid flows based on the AxLAB®. Meanwhile, a recovery procedure was presented in this chapter.

In Chapter 5, briefly describes the subgrid-scale (SGS) stress model and how to combine it with the AxLAB® for turbulence modelling. A recovery procedure was also presented in this chapter.

In Chapter 6, discusses the initial and boundary conditions used in the lattice Boltzmann method. In this chapter, the no-slip, semi-slip and slip boundary conditions are presented.

In Chapter 7, several steady and unsteady flows through axisymmetric pipe and complex rotation flows were simulated and analyzed.

In Chapter 8, the non-Newtonian fluid rotation flows was studied and compared with other methods.

In Chapter 9, a turbulent axisymmetric LBM simulation is presented and applied to simulate the three different cases. The accuracy of the turbulent model was compared with other method and experiment results.

In Chapter 10, conclusions and recommends to future work were presented.

Chapter 2: Governing Equations for Axisymmetric Flows

2.1 Introduction

Fluid flows obey the conservations of mass and momentum. Based on these conservation laws, a set of differential equations can be derived to represent fluid flow motions. A general set of flow equations are the continuity equation and the Navier-Stokes (N-S) equations. In this chapter, the governing equations, the N-S equations, and axisymmetric flow equations with and without turbulence terms are described.

2.2 The Navier-Stokes Equations

The governing equations for general incompressible flows are the three-dimensional continuity and Navier-Stokes (N-S) equations that are derived from Newton's second law of motion and the mass conservation. If Cartesian coordinate is adopted, the N-S equations can be shown as follows:

$$\frac{\partial u}{\partial x}+\frac{\partial v}{\partial y}+\frac{\partial w}{\partial z}=0 \tag{2.1}$$

$$\frac{\partial u}{\partial t}+\frac{\partial (uu)}{\partial x}+\frac{\partial (uv)}{\partial y}+\frac{\partial (uw)}{\partial z}=\nu\left(\frac{\partial^2 u}{\partial x^2}+\frac{\partial^2 u}{\partial y^2}+\frac{\partial^2 u}{\partial z^2}\right)-\frac{1}{\rho}\frac{\partial p}{\partial x}+f_x \tag{2.2}$$

$$\frac{\partial v}{\partial t}+\frac{\partial (vu)}{\partial x}+\frac{\partial (vv)}{\partial y}+\frac{\partial (vw)}{\partial z}=\nu\left(\frac{\partial^2 v}{\partial x^2}+\frac{\partial^2 v}{\partial y^2}+\frac{\partial^2 v}{\partial z^2}\right)-\frac{1}{\rho}\frac{\partial p}{\partial y}+f_y \tag{2.3}$$

$$\frac{\partial w}{\partial t}+\frac{\partial (wu)}{\partial x}+\frac{\partial (wv)}{\partial y}+\frac{\partial (ww)}{\partial z}=\nu\left(\frac{\partial^2 w}{\partial x^2}+\frac{\partial^2 w}{\partial y^2}+\frac{\partial^2 w}{\partial z^2}\right)-\frac{1}{\rho}\frac{\partial p}{\partial z}+f_z \tag{2.4}$$

in which x, y and z are the Cartesian coordinate (see Fig 2.1); u, v and w are the corresponding velocity components, respectively; f_x, f_y and f_z are the body

forces per unit mass in the corresponding direction; ν is the kinematic viscosity; p is the pressure; and ρ is the fluid density and t is the time.

The equations (2.1-2.4) can also be written in tensor form as

$$\frac{\partial u_j}{\partial x_j} = 0, \tag{2.5}$$

$$\frac{\partial u_i}{\partial t} + \frac{\partial \left(u_i u_j \right)}{\partial x_j} = f_i - \frac{1}{\rho}\frac{\partial p}{\partial x_i} + \nu \frac{\partial^2 u_i}{\partial x_j x_j}. \tag{2.6}$$

where the subscripts i and j are space direction indices; f_i is the body force per unit mass acting on fluid in the i direction and the Einstein summation convention is used.

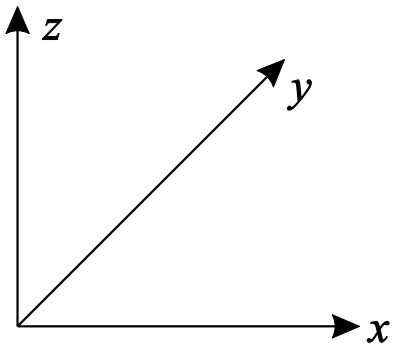

Figure 2.1 Cartesian coordinate system.

The whole left hand side of Eq. (2.6) is an inertia term, in which the second term is called convective term. The three terms on the right hand side are the body force term, the pressure term and the viscous term in sequence. As the general governing equations for fluid flows, the N-S equations have no analytical solution except for some simple situations. However, taking advantage of the increasing computer power, it is possible to obtain numerical solutions to the equations. Thus, numerical methods play an increasingly important role in solving flow problems in engineering.

2.3 Governing Equations in Axisymmetric Flows

2.3.1 Laminar Flow

Consider the flow of an incompressible, isotropic fluid through a three-dimensional pipe. The e_r, e_φ and e_z are the standard orthonormal unit vectors which defining a cylindrical coordinate system:

$$e_r = \left(\frac{x}{r}, \frac{y}{r}, 0 \right), \tag{2.7}$$

$$e_\varphi = \left(\frac{y}{r}, -\frac{x}{r}, 0 \right), \tag{2.8}$$

$$e_z = (0,0,1). \tag{2.9}$$

in which $r = \sqrt{x^2 + y^2}$, φ is the azimuth, $x = r\cos\varphi$ and $y = r\sin\varphi$. If the solution to the Navier-Stokes equation is of the form

$$u = u_r(r,z)e_r + u_z(r,z)e_z, \tag{2.10}$$

that is the velocity field does not depend on φ, then the flow is defined to be axisymmetric (without swirl). The continuity equation in cylindrical coordinate is

$$\frac{\partial u_r}{\partial r} + \frac{u_r}{r} + \frac{\partial u_z}{\partial z} = 0, \tag{2.11}$$

and the components of the momentum equation are:

$$\frac{\partial u_r}{\partial t} + u_r \frac{\partial u_r}{\partial r} + u_z \frac{\partial u_r}{\partial z} = -\frac{1}{\rho}\frac{\partial p}{\partial r} + \nu\left(\frac{\partial^2 u_r}{\partial r^2} + \frac{1}{r}\frac{\partial u_r}{\partial r} - \frac{u_r}{r^2} + \frac{\partial^2 u_r}{\partial z^2} \right), \tag{2.12}$$

$$\frac{\partial u_z}{\partial t} + u_r \frac{\partial u_z}{\partial r} + u_z \frac{\partial u_z}{\partial z} = -\frac{1}{\rho}\frac{\partial p}{\partial r} + \nu\left(\frac{\partial^2 u_z}{\partial r^2} + \frac{1}{r}\frac{\partial u_z}{\partial r} + \frac{\partial^2 u_z}{\partial z^2} \right), \tag{2.13}$$

where ν is the kinematic viscosity. After coordinate transformation, equations (2.11)-(2.13) can be written in Cartesian-like coordinates:

$$\frac{\partial u_j}{\partial x_j} + \frac{u_r}{r} = 0, \tag{2.14}$$

$$\frac{\partial u_i}{\partial t} + u_j \frac{\partial u_i}{\partial x_j} = -\frac{1}{\rho}\frac{\partial p}{\partial x_i} + \nu \frac{\partial^2 u_i}{\partial x_j^2} + \frac{\nu}{r}\frac{\partial u_i}{\partial r} - \frac{\nu u_i}{r^2}\delta_{ir}. \tag{2.15}$$

where the Cartesian coordinate system and the Einstein summation convention are used.

In equation (2.14) and (2.15), ρ is the density; p is the pressure; t is the time; υ is the kinematic viscosity; i is the index standing for r or x; r and x are the coordinates in radial and axial directions, respectively; u_i is the component of velocity in i direction; δ_{ij} is the Kronecker δ function defined by:

$$\delta_{ij} = \begin{cases} 0, & i \neq j, \\ 1, & i = j. \end{cases} \tag{2.16}$$

Incorporation of the continuity equation (2.14) into the momentum equation (2.15) results in [49]:

$$\frac{\partial u_i}{\partial t} + \frac{\partial (u_i u_j)}{\partial x_j} = -\frac{1}{\rho}\frac{\partial p}{\partial x_i} + \nu \frac{\partial}{\partial x_j}\left(\frac{\partial u_i}{\partial x_j} + \frac{\partial u_j}{\partial x_i}\right) + \frac{\nu}{r}\left(\frac{\partial u_i}{\partial r} + \frac{\partial u_r}{\partial x_i}\right) - \frac{u_i u_r}{r} - \frac{2\nu u_i}{r^2}\delta_{ir}. \tag{2.17}$$

2.3.2 Turbulent Flow

Generally speaking, the turbulent flows can be described either by time-averaged Navier-Stokes equation, the Reynolds equation or space-filtered Navier-Stokes equation, the large eddy simulation (LES). In time-averaged models, the variables in turbulent flows are divided into two parts: the time-averaged part and the perturbation part. Taking the velocity for example, it is

$$u_j = \bar{u}_j + u_j'. \tag{2.18}$$

$$\bar{u}_j = \frac{1}{T}\int_t^{t+T} u_j dt. \tag{2.19}$$

where u_j is a universal variable; $\bar{u}_j$ is the time-averaged part and u_j' is the perturbation part of the variable. After substitution of above equation (2.18) into the governing equations, e.g. the N-S equations in the three-dimensional situation,

$$\frac{\partial \bar{u}_j}{\partial x_j} = 0, \tag{2.20}$$

$$\frac{\partial \bar{u}_i}{\partial t} + \frac{\partial\left(\bar{u}_i \bar{u}_j\right)}{\partial x_j} = -\frac{1}{\rho}\frac{\partial p}{\partial x_i} + \nu\frac{\partial^2 \bar{u}_i}{\partial x_j \partial x_j} + \frac{1}{\rho}\frac{\partial \tau_{ij}}{\partial x_j} + f_i, \tag{2.21}$$

a new term $\tau_{ij} = -\rho\overline{u_i' u_j'}$ named the Reynolds stress turns up. According to the Boussinesq approximation [113], the Reynolds stresses τ_{ij} can be expressed in terms of the mean strain rate,

$$\tau_{ij} = -\rho\overline{u_i' u_j'} = -\rho\nu_t\left(\frac{\partial \bar{u}_i}{\partial x_j} + \frac{\partial \bar{u}_j}{\partial x_i}\right). \tag{2.22}$$

As there are ten unknowns (three velocity components, pressure and six stresses) and four equations (the continuity equation and the N-S equations), the closure problem needs to be solved [114]. Based on these problems, there are various levels of approximate methods to close the set of governing equation (2.20) and (2.21) as follows.

1. Zero-Equation models. In this model, a simple algebraic relation is used to compute eddy viscosity. The Reynolds stress tensor is assumed to be proportional to the velocity gradients [115],

$$\nu_t = \frac{\mu_t}{\rho} \sim lu = l_m\left(l_m \frac{dU}{dy}\right), \tag{2.23}$$

l_m is determined experimentally.

2. One-Equation models. These models usually solve a transport equation of a particular turbulent quantity, e.g. turbulent kinetic energy, and obtain a second turbulent quantity from an algebraic expression [114].

$$\nu_t = C_\mu \sqrt{k} l_m. \tag{2.24}$$

$$\frac{\partial k}{\partial t} + U_j \frac{\partial k}{\partial x_j} = \frac{1}{\rho} \tau_{ij} \frac{\partial U_i}{\partial x_j} - \varepsilon + \frac{\partial}{\partial x_j} \left[\frac{1}{\rho} \left(\mu + \frac{\mu_t}{\sigma_k} \right) \frac{\partial k}{\partial x_j} \right]. \tag{2.25}$$

C_μ is a constant determined from simple benchmark experiments by Launder and Spalding [115].

3. Two-Equation models. In this model, two partial differential equations are designed to describe two transport scalars. A typical model in such a category is the widely used $k-\varepsilon$ model [116],

$$\nu_t = C_\mu \frac{k^2}{\varepsilon}. \tag{2.26}$$

$$\rho u_j \frac{\partial k}{\partial x_j} = \rho \tau_{ij} \frac{\partial u_i}{\partial x_j} + \frac{\partial}{\partial x_j} \left[\left(\mu + \frac{\mu_t}{\sigma_k} \right) \frac{\partial k}{\partial x_j} \right] - \left[\rho \varepsilon + 2\mu \left(\frac{\partial k^{1/2}}{\partial x_j} \right)^2 \right], \tag{2.27}$$

$$\rho u_j \frac{\partial \varepsilon}{\partial x_j} = C_1 \frac{\varepsilon}{k} \tau_{ij} \frac{\partial u_i}{\partial x_j} + \frac{\partial}{\partial x_j} \left[\left(\mu + \frac{\mu_t}{\sigma_\varepsilon} \right) \frac{\partial \varepsilon}{\partial x_j} \right] - C_2 \frac{\rho \varepsilon^2}{k} + \frac{2\mu\mu_t}{\rho} \left(\frac{\partial^2 u}{\partial x_2^2} \right)^2. \tag{2.28}$$

where k is the turbulent kinetic energy and ε is the turbulent dissipation rate.

4. Reynolds stress models (RANS). A transport equation is derived for the Reynolds stress $\overline{u_i' u_j'}$. Then the Reynolds stresses are used to obtain closure of the Reynolds-averaged momentum equation [117]. The RANS transport equation is written as

$$\frac{\partial \rho \overline{u_i' u_j'}}{\partial t} + \frac{\partial \rho u_k \overline{u_i' u_j'}}{\partial x_k} = -\frac{\partial}{\partial x_k}\left[\rho \overline{u_i' u_j' u_k'} + \overline{p\left(\delta_{kj} u_i' + \delta_{ik} u_j'\right)} - \mu \frac{\partial}{\partial x_k}\left(\overline{u_i' u_j'}\right)\right] + P_{ij} + G_{ij} + \Phi_{ij} + \varepsilon_{ij}, \tag{2.29}$$

where

$$P_{ij} = -\rho\left(\overline{u_i' u_k'}\frac{\partial u_j}{\partial x_k} + \overline{u_j' u_k'}\frac{\partial u_i}{\partial x_k}\right), \tag{2.30}$$

$$G_{ij} = -\rho\beta\left(g_j \overline{u_j'\theta} - g_j \overline{u_i'\theta}\right), \tag{2.31}$$

$$\Phi_{ij} = \overline{p\left(\frac{\partial u_i'}{\partial x_j} + \frac{\partial u_j'}{x_i}\right)}, \tag{2.32}$$

$$\varepsilon_{ij} = -2\mu \overline{\frac{\partial u_i'}{\partial x_k}\frac{\partial u_j'}{\partial x_k}}. \tag{2.33}$$

The objective of this model is to find the turbulent diffusion, the pressure strain correlation and the turbulent dissipation rate.

Lots of research shows that the space-filtered Navier-Stokes equation is more expensive to use than the time-averaged Reynolds equation, but it can produce more accurate solution to turbulent flows and also provide detailed characteristics of flow turbulence [54]. Therefore, the large eddy simulation is used for turbulent flows in this study. The flow equations for the large eddy simulation can be obtained by introducing a space-filtered quantity in the continuity (Eq.(2.5)) and the momentum equation (Eq.(2.6)). The space-filtered continuity and Naviaer-Stokes equation can be denoted as:

$$\frac{\partial \tilde{u}_j}{\partial x_j} = 0, \tag{2.34}$$

and

$$\frac{\partial \tilde{u}_i}{\partial t}+\frac{\partial\left(\tilde{u}_i \tilde{u}_j\right)}{\partial x_j}=-\frac{1}{\rho}\frac{\partial p}{\partial x_i}+\nu\frac{\partial^2 \tilde{u}_i}{\partial x_j \partial x_j}-\frac{\partial \tau_{ij}}{\partial x_j}+f_i, \tag{2.35}$$

where $\tilde{u}_i$ is the space-filtered velocity component in i direction defined by:

$$\tilde{u}(x,y,z,t)=\iiint_{\Delta x\Delta y\Delta z} u(x,y,z,t)G\left(x,y,z,x',y',z'\right)dx'dy'dz' \tag{2.36}$$

with a spatial filter function G. τ_{ij} is named the subgrid-scale stress which reflects the effects of the unresolved scale with the resolved scales, i.e.

$$\tau_{ij}=u_i u_j-\tilde{u}_i \tilde{u}_j. \tag{2.37}$$

By following the Boussinesq assumption for turbulent stress, the subgrid-scale (SGS) stress with an SGS eddy viscosity ν_e was further represented as

$$\tau_{ij}=-\nu_e\left(\frac{\partial \tilde{u}_i}{\partial x_j}+\frac{\partial \tilde{u}_j}{\partial x_i}\right). \tag{2.38}$$

Substitution of Eq.(2.38) into Eq.(2.35) leads to the following momentum equation,

$$\frac{\partial \tilde{u}_i}{\partial t}+\frac{\partial\left(\tilde{u}_i \tilde{u}_j\right)}{\partial x_j}=-\frac{1}{\rho}\frac{\partial p}{\partial x_i}+\nu_t\frac{\partial^2 \tilde{u}_i}{\partial x_j \partial x_j}+f_i. \tag{2.39}$$

where ν_t is the total viscosity $\nu_t=\nu+\nu_e$, ν is the kinematic viscosity; ν_e is the eddy viscosity, defined by

$$\nu_e=\left(C_s l_s\right)^2\sqrt{S_{ij}S_{ij}}, \tag{2.40}$$

where C_s is the Smagorinsky constant [53], l_s is the characteristic length scale and S_{ij} is the magnitude of the large scale strain-rate tensor.

$$S_{ij} = \frac{1}{2\rho}\left[\frac{\partial\left(\rho\tilde{u}_i\right)}{\partial x_j} + \frac{\partial\left(\rho\tilde{u}_j\right)}{\partial x_i}\right]. \tag{2.41}$$

For the subgrid-scale (SGS) stress model, the finer the grid size, the less unresolved scale eddies. If the grid size is small enough, the SGS model can be a direct numerical simulation. because in the lattice Boltzmann method, the lattice spacing and the mesh size is usually much smaller than that used in a traditional computation method, it can be expected an incorporation of a subgrid-stress model into the lattice Boltzmann method can obtain more accurate solution for turbulent flows.

Substitution of Eq. (2.37) into Eq.(2.35) leads to the following momentum equation,

$$\frac{\partial\tilde{u}_i}{\partial t} + \frac{\partial\left(\tilde{u}_i\tilde{u}_j\right)}{\partial x_j} = -\frac{1}{\rho}\frac{\partial p}{\partial x_i} + \left(\nu+\nu_e\right)\frac{\partial^2\tilde{u}_i}{\partial x_j\partial x_j} - u_i^{'}u_j^{'} + f_i. \tag{2.42}$$

From the above equation, it is noticed that a new term $u_i^{'}u_j^{'}$ turns up which named as Reynolds stress.

For convenience, the hats of u_i and u_j in following equations are dropped off resulting the same form of general turbulent axisymmetric flow equations, but the corresponding symbols represent the space-filtered variables. The governing equations for the incompressible axisymmetric turbulent flow in a cylindrical coordinate system can be written in tensor form as:

$$\frac{\partial u_j}{\partial x_j} + \frac{u_r}{r} = 0, \tag{2.43}$$

$$\frac{\partial u_i}{\partial t} + u_j\frac{\partial u_i}{\partial x_j} = -\frac{1}{\rho}\frac{\partial p}{\partial x_i} + \nu_t\frac{\partial^2 u_i}{\partial x_j^2} + \frac{\nu_t}{r}\frac{\partial u_i}{\partial r} - \frac{\nu_t u_i}{r^2}\delta_{ir}. \tag{2.44}$$

where ν_t is the full viscosity for turbulent flow, $\nu_t = \nu + \nu_e$.

Chapter 3: Lattice Boltzmann Method

3.1 Introduction

Evolving from a simplified and fictitious molecular model (the lattice gas cellular automata (LGCA)), the lattice Boltzmann method (LBM) is a discrete computational method. In general, it is comprised of three components: the lattice Boltzmann equation controls the transport of the particle distribution function from one lattice to the nearby lattice; a lattice pattern represents grid nodes and determines particles' motions; and the local equilibrium distribution function decides what flow equations are recovered by the lattice Boltzmann model, e.g. the axisymmetric flow equations. These three main topics and some related aspects are described in this chapter.

3.2 Derivation of the Lattice Boltzmann Equation

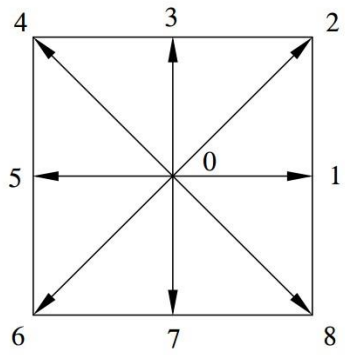

Figure 3.1 Nine-speed square lattice (D2Q9).

In lattice Boltzmann theory [14], the streaming and collision steps are the main two steps that make up the LBM. In the streaming step, particles that move towards their nearest neighbours at their own velocities and their directions are governed by:

$$f_\alpha\left(x+e_\alpha\Delta t,t+\Delta t\right)=f_\alpha^{'}\left(x,t\right)+\frac{\Delta t}{N_\alpha e^2}e_{\alpha i}F_i\left(x,t\right). \tag{3.1}$$

where f_α is the distribution function of the particles, $f_\alpha^{'}$ is the value before the streaming, e_α is the velocity vector of a particle in the α link; Δt is the time step, x is the space vector, $e = \Delta x / \Delta t$; Δx is the lattice size; F_i is the force term, N_α is a constant decided by the lattice pattern as:

$$N_\alpha = \frac{1}{e^2}\sum_\alpha e_{\alpha x} e_{\alpha x} = \frac{1}{e^2}\sum_\alpha e_{\alpha y} e_{\alpha y}, \tag{3.2}$$

Meanwhile, in the collision step, the particles arrive and interact with one another and change their velocities and directions according to the rules of scattering, denoted by:

$$f_\alpha^{'}(x,t) = f_\alpha(x,t) + \Omega_\alpha\left[f(x,t)\right], \tag{3.3}$$

where Ω_α is the collision operator that controls the speed of change in f_α during collision.

The collision operator Ω_α is a matrix and can be obtained from kinetic theory. However, due to the complexity of the analytic solutions, Higuera and Jimenez [118] proposed a fundamentally important idea of simplifying the collision operator. They linearized the collision operator around its local equilibrium state. This collision operator Ω_α is then expanded in terms of its equilibrium value. Referring to Noble *et al*. [119], the operator is as follows:

$$\Omega_\alpha(f) = \Omega_\alpha\left(f^{eq}\right) + \frac{\partial\Omega_\alpha\left(f^{eq}\right)}{\partial f_\beta}\left(f_\beta - f_\beta^{eq}\right) + O\left[\left(f_\beta - f_\beta^{eq}\right)^2\right], \tag{3.4}$$

where f_α^{eq} is the local equilibrium distribution function.

After high-order terms in Eq. (3.4) are neglected and implying that $\Omega_\alpha\left(f^{eq}\right) = 0$, a linearized collision operator (equation (3.5)) is obtained:

$$\Omega_\alpha(f) \approx \frac{\partial \Omega_\alpha\left(f^{eq}\right)}{\partial f_\beta}\left(f_\beta - f_\beta^{eq}\right). \tag{3.5}$$

If assuming the local particle distribution relaxes to an equilibrium state at a single rate τ [120,121],

$$\frac{\partial \Omega_\alpha\left(f^{eq}\right)}{\partial f_\beta} = -\frac{1}{\tau}\delta_{\alpha\beta}, \tag{3.6}$$

where $\delta_{\alpha\beta}$ is the Kronecker delta function:

$$\delta_{\alpha\beta} = \begin{cases} 0, & \alpha \neq \beta, \\ 1, & \alpha = \beta, \end{cases} \tag{3.7}$$

Eq. (3.5) can be written as

$$\Omega_\alpha(f) = -\frac{1}{\tau}\delta_{\alpha\beta}\left(f_\beta - f_\beta^{eq}\right), \tag{3.8}$$

the above Eq. (3.8) resulting in the lattice BGK collision operator [116],

$$\Omega_\alpha(f) = -\frac{1}{\tau}\left(f_\alpha - f_\alpha^{eq}\right), \tag{3.9}$$

where τ is named as single relaxation time. By substituting the collision operator (3.9) into (3.3), the most popular lattice Boltzmann equation or the so-called single relaxation time lattice Boltzmann equation can be expressed as follows [14]:

$$f_\alpha\left(x + e_\alpha \Delta t, t + \Delta t\right) - f_\alpha(x,t) = -\frac{1}{\tau}\left(f_\alpha - f_\alpha^{eq}\right) + \frac{\Delta t}{N_\alpha e^2} e_{\alpha i} F_i(x,t). \tag{3.10}$$

3.2.1 Relation to Continuum Boltzmann Equation

Although the lattice Boltzmann equation (3.10) historically evolved from LGCA, the LBE can also be derived from the continuous Boltzmann equation (CBE).

The CBE with the BGK approximation reads [121]:

$$\frac{\partial f}{\partial t} + e \cdot \nabla f = -\frac{1}{\zeta}\left(f - f^{eq} \right). \tag{3.11}$$

where $f = f\left(x, e, t\right)$ is the single-particle distribution in continuum phase space $\left(x, e\right)$; e is the particle velocity; ζ is a relaxation time; $\nabla = i\frac{\partial}{\partial x} + j\frac{\partial}{\partial y}$ is the gradient operator; and f^{eq} is the Maxwell-Boltzmann equilibrium distribution function defined by

$$f^{eq} = \frac{\rho}{\sqrt{\left(2\pi/3\right)^{D}}} \exp\left[-\frac{3}{2}\left(e - V\right)^{2} \right], \tag{3.12}$$

where D is the spatial dimension; particle velocity $\boldsymbol{e}$ and fluid velocity V are normalized by $\sqrt{3RT}$; R is the ideal gas constant and T is temperature, which produce a sound speed of $U_s = 1/\sqrt{3}$. [18]. Then the fluid density and velocity are calculated in terms of the distribution function,

$$\rho = \int f de, \tag{3.13}$$

$$\rho V = \int e f de. \tag{3.14}$$

If the fluid velocity V is small compared with the sound speed, the equilibrium distribution function given by Eq. (3.12) can be expanded in the following form up to the second order accuracy [123],

$$f^{eq} = \frac{\rho}{\sqrt{(2\pi/3)^D}} \exp\left(-\frac{3}{2}e^2\right)\left[1+3(eV)+\frac{9}{2}(eV)^2-\frac{3}{2}V^2\right]. \tag{3.15}$$

In order to introduce a discrete Boltzmann model, a finite set of velocities and associated distribution functions are built up instead of the whole.

$$f_\alpha(x,t) = f(x,e_\alpha,t), \tag{3.16}$$

$$f_\alpha^{eq}(x,t) = f^{eq}(x,e_\alpha,t), \tag{3.17}$$

They still satisfy Eq. (3.11)

$$\frac{\partial f_\alpha}{\partial t} + e_\alpha \cdot \nabla f_\alpha = -\frac{1}{\zeta}\left(f_\alpha - f_\alpha^{eq}\right) + S_a, \tag{3.18}$$

where for D2Q9 square lattice,

$$S_\alpha = \frac{1}{6e^2} e_{\alpha i} F_i. \tag{3.19}$$

A discretization of Eq. (3.18) is given by

$$\begin{aligned} \frac{f_\alpha(x,t+\Delta t)-f_\alpha(x,t)}{\Delta t} + e_{\alpha x}\frac{f_\alpha(x+\Delta x,t+\Delta t)-f_\alpha(x,t+\Delta t)}{\Delta x} \\ = -\frac{1}{\zeta}\left(f_\alpha - f_\alpha^{eq}\right) + S_\alpha, \end{aligned} \tag{3.20}$$

$$\begin{aligned} f_\alpha(x,t+\Delta t)-f_\alpha(x,t) + e_{\alpha x}\frac{\Delta t}{\Delta x}\left[f_\alpha(x+\Delta x,t+\Delta t)-f_\alpha(x,t+\Delta t)\right] \\ = -\frac{1}{\zeta/\Delta t}\left(f_\alpha - f_\alpha^{eq}\right) + S_\alpha \Delta t, \end{aligned} \tag{3.21}$$

Lagrangian behaviour is then obtained by the selection of $\Delta x/\Delta t = e_{\alpha x}$ and the terms of $f_\alpha(x,\ t+\Delta t)$ are cancelled, leading the above equation to

$$f_\alpha(x+e_\alpha\Delta t, t+\Delta t) - f_\alpha(x,t) = -\frac{1}{\tau}\left(f_\alpha - f_\alpha^{eq}\right) + S_\alpha \Delta t. \tag{3.22}$$

with $\tau = \zeta / \Delta t$. Strictly speaking, τ should be called a single dimensionless relaxation time. The beauty of above transformation is that it provides a linear approach Eq.(3.22) to model a nonlinear system Eq.(3.18), since the terms regarding $f_\alpha\left(x,\ t+\Delta t\right)$ disappear.

3.3 Lattice Pattern

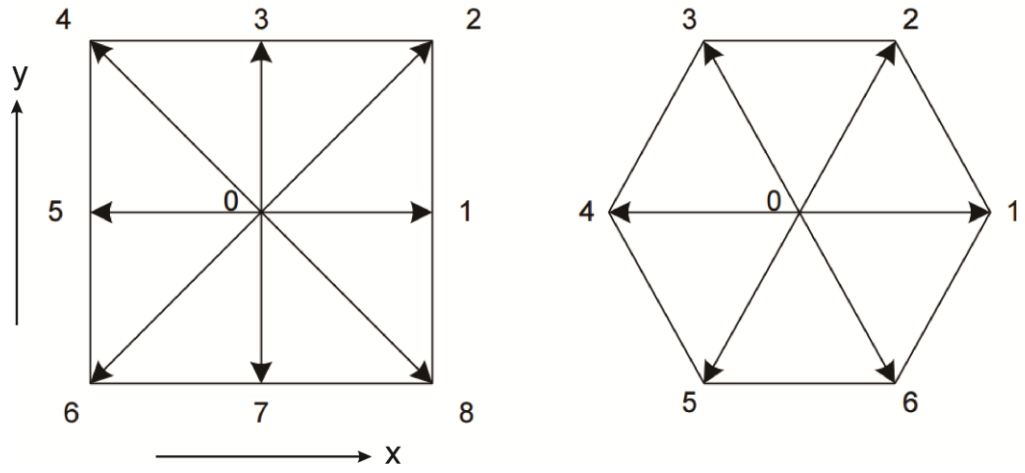

Figure 3.2 Lattice Patterns: 9-speed square lattice (D2Q9) and 7-speed hexagonal lattice (D2Q7).

In the traditional methods, a lattice pattern is used to set up grid points. But in the lattice Boltzmann method, it has another function, determining particle's motions, and a microscopic model for molecular dynamics. In the lattice Boltzmann equation Eq.(3.10), the constant N_α is determined by the lattice pattern.

In two-dimensional situations, there are various regular lattice patterns for selection, for which the LBM can be written down in a simple, explicit form [123]. Among these lattice patterns, the square and hexagonal lattices (from Fig. 3.2) are popular. In this thesis, they are referred by D2Q9 and D2Q7 respectively, i.e. two dimensional, nine or seven velocities according to Qian's denotation [124]. The square lattice can also be D2Q4 or D2Q8 and the hexagonal lattice can be D2Q6 regardless of the zero velocity. However, not all these lattice patterns have sufficient symmetry that is a

dominant requirement for recovery of the correct flow equations [15]. Theoretical analysis and numerical tests illustrate that both the D2Q9 and D2Q7 lattice have such a property and satisfactory performance in numerical simulations. In 1993, Skordos indicated that models based on the D2Q9 lattice usually produce more accurate results than those using the D2Q7 lattice [125]. Furthermore, the use of the square lattice offers an easy way to implement different boundary conditions [126], e.g. the force term can be associated with a gradient and boundary conditions can be easily and accurately determined. Therefore, the D2Q9 lattice is preferred.

For the 9-speed square lattice (D2Q9) shown in Fig. 3.1, each particle moves one lattice unit at its velocity along one of the eight links indicated with number 1-8, or else 0 indicates the particle at rest with zero speed. The velocity of particles is defined by:

$$e_\alpha = \begin{cases} (0,0), & \alpha = 0, \\ e\left[\cos\dfrac{(\alpha-1)\pi}{4}, \sin\dfrac{(\alpha-1)\pi}{4}\right], & \alpha = 1,3,5,7, \\ \sqrt{2}e\left[\cos\dfrac{(\alpha-1)\pi}{4}, \sin\dfrac{(\alpha-1)\pi}{4}\right], & \alpha = 2,4,6,8. \end{cases} \tag{3.23}$$

It is easy to demonstrate that the 9-speed square lattice has the following basic features,

$$\sum_\alpha e_{\alpha i} = \sum_\alpha e_{\alpha i} e_{\alpha j} e_{\alpha k} = 0, \tag{3.24}$$

$$\sum_\alpha e_{\alpha i} e_{\alpha j} = 6e^2 \delta_{ij}, \tag{3.25}$$

$$\sum_\alpha e_{\alpha i} e_{\alpha j} e_{\alpha k} e_{\alpha l} = 4e^4 \left(\delta_{ij}\delta_{kl} + \delta_{ik}\delta_{jl} + \delta_{il}\delta_{jk}\right) - 6e^4 \Delta_{ijkl}, \tag{3.26}$$

where $\Delta_{ijkl} = \begin{cases} 1, & i = j = k = l, \\ 0, & otherwise. \end{cases}$

Substitution Eq. (3.23) into Eq. (3.2), the following equation can be obtained

$$N_\alpha = \frac{1}{e^2}\sum_\alpha e_{\alpha x}e_{\alpha x} = \frac{1}{e^2}\sum_\alpha e_{\alpha y}e_{\alpha y} = 6. \tag{3.27}$$

Combining the above equation and Eq.(3.10), the most common form of a lattice Boltzmann model with D2Q9 lattice can be obtained.

$$f_\alpha\left(x+e_\alpha\Delta t, t+\Delta t\right) - f_\alpha\left(x,t\right) = -\frac{1}{\tau}\left(f_\alpha - f_\alpha^{eq}\right) + \frac{\Delta t}{6e^2}e_{\alpha i}F_i\left(x,t\right). \tag{3.28}$$

3.4 Local Equilibrium Distribution Function

The local equilibrium distribution function plays a significant role in the lattice Boltzmann method. It decides what flow equations are solved by the lattice Boltzmann model. A suitable local equilibrium distribution function f_α^{eq} must be derived, if the lattice Boltzmann equation Eq. (3.28) is applied to solve the two dimensional axisymmetric flow equations (2.14) and (2.15). According to the theory of the lattice gas cellular automata (LGCA), an equilibrium function is the Fermi-Dirac distribution, which is often expanded as a Taylor series in macroscopic velocity to its second order [127]. For the lattice Boltzmann method, applying a Taylor expansion to the Maxwell-Boltzmann distribution can obtain the equilibrium distribution function for recovering the Navier-Stokes equations [128]. However these methods are not suitable to generate the axisymmetric flow equations. Thus an alternative and powerful way called the Ansatz method [129] is used to find the proper expression for the local equilibrium distribution function. In the Ansatz method, an equilibrium function can be assumed as a power series in macroscopic velocity [14].

$$f_\alpha^{eq} = A_\alpha + B_\alpha e_{\alpha i}u_i + C_\alpha e_{\alpha i}e_{\alpha j}u_i u_j + D_\alpha u_i u_j, \tag{3.29}$$

This assumption makes the process a general approach, which is successfully used for solution of various flow problems. Its accuracy and flexibility have been proved and

demonstrated by a number of researchers [130,131,132]. Since the equilibrium function has the same symmetry as the lattice, there must be

$$A_1 = A_3 = A_5 = A_7 = \dot{A}, \tag{3.30}$$

$$A_2 = A_4 = A_6 = A_8 = \ddot{A}, \tag{3.31}$$

Similar expressions for B_α, C_α and D_α. For convenience, Eq. (3.29) is expressed as

$$f_\alpha^{eq} = \begin{cases} A_0 - D_0 u_i u_i, & \alpha = 0, \\ \dot{A} + \dot{B} e_{\alpha i} u_i + \dot{C} e_{\alpha i} e_{\alpha j} u_i u_j - \dot{D} u_i u_i, & \alpha = 1,3,5,7, \\ \ddot{A} + \ddot{B} e_{\alpha j} u_i + \ddot{C} e_{\alpha i} e_{\alpha j} u_i u_j - \ddot{D} u_i u_i, & \alpha = 2,4,6,8. \end{cases} \tag{3.32}$$

In order to determine the coefficients in the above equations, the conservation relations such as mass and momentum conservations are used as the constraints on the equilibrium distribution function. For the axisymmetric flow equations, the local equilibrium distribution function (3.32) must satisfy the following three conditions,

$$\sum_\alpha f_\alpha^{eq} = \rho, \tag{3.33}$$

$$\sum_\alpha e_{\alpha i} f_\alpha^{eq} = \rho u_i, \tag{3.34}$$

$$\sum_\alpha e_{\alpha i} e_{\alpha j} f_\alpha^{eq} = p\delta_{ij} + \rho u_i u_j. \tag{3.35}$$

Based on the above constraints, the calculation of the lattice Boltzmann equation (3.28) leads to the solution of the two-dimensional axisymmetric flow equations (2.14) and (2.15). In this procedure, the source term of the axisymmetric flow equations, such as the friction force and the wind shear stress, is not involved, since it will be cancelled out.

If Eq. (3.33) is substituted into Eq. (3.32), one can obtain,

$$
\begin{aligned}
&A_0 - D_0 u_i u_i \\
&+4\dot{A} + \sum_{\alpha=1,3,5,7} \dot{B} e_{\alpha i} u_i + \sum_{\alpha=1,3,5,7} \dot{C} e_{\alpha i} e_{\alpha j} u_i u_j - 4\dot{D} u_i u_i \\
&+4\ddot{A} + \sum_{\alpha=2,4,6,8} \ddot{B} e_{\alpha i} u_i + \sum_{\alpha=2,4,6,8} \ddot{C} e_{\alpha i} e_{\alpha j} u_i u_j - 4\ddot{D} u_i u_i = \rho.
\end{aligned} \tag{3.36}
$$

Substituting Eq. (3.23) into the above equation evaluating the coefficients of ρ and $u_i u_i$ respectively, so

$$A_0 + 4\dot{A} + 4\ddot{A} = \rho, \tag{3.37}$$

$$D_0 + 2e^2\dot{C} + 4e^2\ddot{C} + 4\dot{D} + 4\ddot{D} = 0. \tag{3.38}$$

Similarly, inserting Eq. (3.32) to Eq.(3.34) yields

$$
\begin{aligned}
&A_0 e_{\alpha i} - D_0 e_{\alpha i} u_j u_j \\
&+ \sum_{\alpha=1,3,5,7} \left(\dot{A} e_{\alpha i} + \dot{B} e_{\alpha i} e_{\alpha j} u_i + \dot{C} e_{\alpha i} e_{\alpha j} e_{\alpha k} u_i u_j - \dot{D} e_{\alpha i} u_i u_i \right) \\
&+ \sum_{\alpha=2,4,6,8} \left(\ddot{A} e_{\alpha i} + \ddot{B} e_{\alpha i} e_{\alpha j} u_i + \ddot{C} e_{\alpha i} e_{\alpha j} e_{\alpha k} u_i u_j - \ddot{D} e_{\alpha i} u_i u_i \right) = \rho u_i .
\end{aligned} \tag{3.39}
$$

Making the coefficients of u_i equal results in

$$2e^2\dot{B} + 4e^2\ddot{B} = \rho. \tag{3.40}$$

Again, inserting Eq. (3.32) to the third constraint Eq.(3.35) yields

$$
\begin{aligned}
&\sum_{\alpha=1,3,5,7} \left(\dot{A} e_{\alpha i} e_{\alpha j} + \dot{B} e_{\alpha i} e_{\alpha j} e_{\alpha k} u_j u_k + \dot{C} e_{\alpha i} e_{\alpha j} e_{\alpha k} e_{\alpha l} u_k u_l - \dot{D} e_{\alpha i} e_{\alpha j} u_k u_k \right) \\
&+ \sum_{\alpha=2,4,6,8} \left(\ddot{A} e_{\alpha i} e_{\alpha j} + \ddot{B} e_{\alpha i} e_{\alpha j} e_{\alpha k} u_j u_k + \ddot{C} e_{\alpha i} e_{\alpha j} e_{\alpha k} e_{\alpha l} u_k u_l - \ddot{D} e_{\alpha i} e_{\alpha j} u_k u_k \right) \\
&= p\delta_{ij} + \rho u_i u_j .
\end{aligned} \tag{3.41}
$$

Substituting Eq. (3.23) into the above equation leads to

$$\begin{aligned} &2\dot{A}e^2\delta_{ij} + 2\dot{C}e^4 u_i u_i + 2\dot{D}e^2 u_i u_i + 4\ddot{A}e^2\delta_{ij} \\ &+8\ddot{C}e^2 u_i u_j + 4\ddot{C}e^4 u_i u_i + 4\ddot{C}e^2 u_i u_i = p\delta_{ij} + \rho u_i u_j . \end{aligned} \tag{3.42}$$

Another four relations can be obtained based on the above equation,

$$2e^2\dot{A} + 4e^2\ddot{A} = p, \tag{3.43}$$

$$8e^2\ddot{C} = \rho, \tag{3.44}$$

$$2e^2\dot{C} = \rho, \tag{3.45}$$

$$2e^2\dot{D} + 4e^2\ddot{D} + 4e^4\ddot{C} = 0. \tag{3.46}$$

Eqs. (3.44) and (3.45) can be put together and yields

$$4\ddot{C} = \dot{C}. \tag{3.47}$$

Due to the symmetry, it is feasible to assume three additional relations with respect to Eq. (3.47).

$$4\ddot{A} = \dot{A}, \tag{3.48}$$

$$4\ddot{B} = \dot{B}, \tag{3.49}$$

$$4\ddot{D} = \dot{D}. \tag{3.50}$$

Up to now, ten equations, (3.37), (3.38), (3.40) and (3.43) - (3.50) are available, so the coefficients can be calculated

$$A_0 = \frac{4}{9}\rho, \quad B_0 = -\frac{2\rho}{3e^2} \tag{3.51}$$

$$\dot{A} = \frac{\rho}{9}, \quad \dot{B} = \frac{\rho}{3e^2}, \quad \dot{C} = \frac{\rho}{2e^4}, \quad \dot{D} = -\frac{\rho}{6e^4} \tag{3.52}$$

$$\ddot{A}=\frac{\rho}{36},\quad \ddot{B}=\frac{\rho}{12e^2},\quad \ddot{C}=\frac{\rho}{8e^2},\quad \ddot{D}=-\frac{\rho}{24e^2} \tag{3.53}$$

Therefore, if Eqs. (3.51), (3.52) and (3.53) are substituted into Eq. (3.32), the local equilibrium distribution function is expressed as

$$f_a^{eq}=\omega_a\rho\left(1+3\frac{e_{ai}u_i}{e^2}+\frac{9}{2}\frac{e_{ai}e_{aj}u_iu_j}{e^4}-\frac{3}{2}\frac{u_iu_i}{e^2}\right), \tag{3.54}$$

where

$$\omega_\alpha=\begin{cases}\dfrac{4}{9}, & \alpha=0,\\ \dfrac{1}{9}, & \alpha=1,3,5,7,\\ \dfrac{1}{36}, & \alpha=2,4,6,8.\end{cases} \tag{3.55}$$

This local equilibrium distribution function is then used in the lattice Boltzmann equation for solving the axisymmetric flow equations.

3.5 Lattice Boltzmann Equation for Axisymmetric Flows

3.5.1 Axisymmetric Flows without Swirl

The AxLAB® on the nine-speed square lattice shown in Fig. 3.1 reads [50],

$$f_\alpha\left(x+e_\alpha\Delta t,t+\Delta t\right)-f_\alpha\left(x,t\right)=-\tau_\alpha\left(f_\alpha-f_\alpha^{eq}\right)+\omega_\alpha\theta\Delta t+\frac{\Delta t}{\mathcal{K}e^2}e_{\alpha i}F_i, \tag{3.56}$$

where f_α is the distribution function of the particles, f_α^{eq} is the local equilibrium distribution function, Δt is the time step, x is the space vector, $e=\Delta x/\Delta t$; Δx is the lattice size; ω_α is the weight, θ is the source or sink term,

$$\theta = -\frac{\rho u_r}{r}, \tag{3.57}$$

F_i is the force term calculated by:

$$F_i = -\frac{\rho u_i u_r}{r} - \frac{2\rho\nu u_i}{r^2}\delta_{ir}; \tag{3.58}$$

in which δ_{ij} is the Kronecker δ function, $e_{\alpha i}$ is the component of e_α, which is the velocity vector of a particle in the α link

$$e_\alpha = \begin{cases} (0,0), & \alpha = 0, \\ \lambda_\alpha e\left[\cos\dfrac{(\alpha-1)\pi}{4}, \sin\dfrac{(\alpha-1)\pi}{4}\right], & \alpha \neq 0; \end{cases} \tag{3.59}$$

With λ_α defined as:

$$\lambda_\alpha = \begin{cases} 1, & \alpha = 1,3,5,7, \\ \sqrt{2}, & \alpha = 2,4,6,8. \end{cases} \tag{3.60}$$

$\mathcal{K}$ is constant and can be defined by:

$$\mathcal{K} = \frac{1}{e^2}\sum_\alpha e_{\alpha x} e_{\alpha x} = \frac{1}{e^2}\sum_\alpha e_{\alpha r} e_{\alpha r;} \tag{3.61}$$

and τ_α is the relaxation time:

$$\tau_\alpha = \begin{cases} \dfrac{1}{\tau}, & r = 0, \\ \dfrac{1}{\tau}\left[1 + \dfrac{(2\tau-1)e_{\alpha r}\Delta t}{2r}\right], & r \neq 0. \end{cases} \tag{3.62}$$

If the nine-speed lattice pattern is used, w_α is defined by Eq.(3.55).

The constant relaxation time τ and the fluid kinematic viscosity ν have the relationship as follows:

$$\nu = \frac{e^2 \Delta t}{6}(2\tau - 1). \tag{3.63}$$

The local equilibrium distribution function f_α^{eq} can be calculated from Eq. (3.54). According to the definition, the fluid density ρ and velocity u_i can be obtained from

$$\rho = \sum_\alpha f_\alpha, \tag{3.64}$$

$$u_i = \frac{1}{\rho}\sum_\alpha e_{\alpha i} f_\alpha. \tag{3.65}$$

3.5.2 Recovery of the Axisymmetric Flow Equations without Swirl

The Chapman-Enskog analysis is applied to show that the macroscopic equations (2.14) and (2.17) can be derived from the lattice Boltzmann equation (3.56). It is assumed that Δt is small and equal to ε,

$$\Delta t = \varepsilon. \tag{3.66}$$

Substitution of the above equation into Eq.(3.56) yields

$$\begin{aligned} & f_\alpha(x + e_\alpha \varepsilon, t + \varepsilon) - f_\alpha(x,t) \\ & \quad = -\frac{1}{\tau}\left(f_\alpha - f_\alpha^{eq}\right) - \frac{(2\tau - 1)}{2\tau r} e_{\alpha r} \varepsilon \left(f_\alpha - f_\alpha^{eq}\right) + w_\alpha \theta \varepsilon + \frac{\varepsilon}{6e^2} e_{\alpha i} F_i. \end{aligned} \tag{3.67}$$

By taking a Taylor expansion to Eq.(3.67) in time and space at point (x,t),

$$\begin{aligned}&\varepsilon\left(\frac{\partial}{\partial t}+e_{\alpha j}\frac{\partial}{\partial x_j}\right)f_\alpha+\frac{1}{2}\varepsilon^2\left(\frac{\partial}{\partial t}+e_{\alpha j}\frac{\partial}{\partial x_j}\right)^2 f_\alpha+O\left(\varepsilon^3\right)\\&=-\frac{1}{\tau}\left(f_\alpha-f_\alpha^{eq}\right)-\frac{(2\tau-1)}{2\tau r}e_{\alpha r}\varepsilon\left(f_\alpha-f_\alpha^{eq}\right)+\varepsilon w_\alpha\theta+\frac{\varepsilon}{6e^2}e_{\alpha i}F_i.\end{aligned}\tag{3.68}$$

According to the Chapman-Enskog expansion, f_α can be written in a series of ε,

$$f_\alpha=f_\alpha^{(0)}+\varepsilon f_\alpha^{(1)}+\varepsilon^2 f_\alpha^{(2)}+O\left(\varepsilon^3\right).\tag{3.69}$$

The centered scheme [9] is used for both source term θ and force term F_i as

$$\theta=\theta\left(x+\frac{1}{2}e_\alpha\varepsilon,t+\frac{1}{2}\varepsilon\right)\tag{3.70}$$

and

$$F_i=F_i\left(x+\frac{1}{2}e_\alpha\varepsilon,t+\frac{1}{2}\varepsilon\right).\tag{3.71}$$

which can also be written, via a Taylor expansion, as

$$\theta\left(x+\frac{1}{2}e_\alpha\varepsilon,t+\frac{1}{2}\varepsilon\right)=\theta\left(x,t\right)+\frac{1}{2}\varepsilon\left(\frac{\partial}{\partial t}+e_{\alpha j}\frac{\partial}{\partial x_j}\right)\theta\left(x,t\right)+O\left(\varepsilon^2\right)\tag{3.72}$$

and

$$F_i\left(x+\frac{1}{2}e_\alpha\varepsilon,t+\frac{1}{2}\varepsilon\right)=F_i\left(x,t\right)+\frac{1}{2}\varepsilon\left(\frac{\partial}{\partial t}+e_{\alpha j}\frac{\partial}{\partial x_j}\right)F_i\left(x,t\right)+O\left(\varepsilon^2\right).\tag{3.73}$$

After substitution of Eq.(3.69), (3.72) and (3.73) into Eq.(3.68), the equation to the order of ε^0 is

$$f_\alpha^{(0)}=f_\alpha^{eq},\tag{3.74}$$

to the order of ε is

$$\left(\frac{\partial}{\partial t}+e_{\alpha j}\frac{\partial}{\partial x_j}\right)f_\alpha^{(0)}=-\frac{f_\alpha^{(1)}}{\tau}+w_\alpha\theta+\frac{1}{6e^2}e_{\alpha i}F_i, \tag{3.75}$$

and to the order of ε^2 is

$$\begin{aligned}&\left(\frac{\partial}{\partial t}+e_{\alpha j}\frac{\partial}{\partial x_j}\right)f_\alpha^{(1)}+\frac{1}{2}\varepsilon^2\left(\frac{\partial}{\partial t}+e_{\alpha j}\frac{\partial}{\partial x_j}\right)^2 f_\alpha^{(0)}=-\frac{f_\alpha^{(2)}}{\tau}-\frac{(2\tau-1)}{2\tau r}e_{\alpha r}f_\alpha^{(1)}\\&+\frac{1}{2}\left(\frac{\partial}{\partial t}+e_{\alpha j}\frac{\partial}{\partial x_j}\right)(w_\alpha\theta)+\frac{1}{12e^2}\left(\frac{\partial}{\partial t}+e_{\alpha j}\frac{\partial}{\partial x_j}\right)(e_{\alpha i}F_i).\end{aligned} \tag{3.76}$$

By using Eq. (3.75), the above equation can be written as

$$\frac{(2\tau-1)}{2\tau}\left(\frac{\partial}{\partial t}+e_{\alpha j}\frac{\partial}{\partial x_j}\right)f_\alpha^{(1)}=-\frac{f_\alpha^{(2)}}{\tau}-\frac{(2\tau-1)}{2\tau}e_{\alpha r}f_\alpha^{(1)}. \tag{3.77}$$

From Eq. (3.75)+ $\varepsilon\times$ Eq.(3.77),

$$\begin{aligned}&\left(\frac{\partial}{\partial t}+e_{\alpha j}\frac{\partial}{\partial x_j}\right)f_\alpha^{(0)}+\frac{(2\tau-1)\varepsilon}{2\tau}\left(\frac{\partial}{\partial t}+e_{\alpha j}\frac{\partial}{\partial x_j}\right)f_\alpha^{(1)}\\&=-\frac{1}{\tau}\left(f_\alpha^{(1)}-\varepsilon f_\alpha^{(2)}\right)-\frac{(2\tau-1)\varepsilon}{2\tau}e_{\alpha r}f_\alpha^{(1)}+w_\alpha\theta+\frac{1}{6e^2}e_{\alpha i}F_i.\end{aligned} \tag{3.78}$$

The summation of the above equation over α provides

$$\frac{\partial}{\partial t}\sum_\alpha f_\alpha^{(0)}+\frac{\partial}{\partial x_j}\sum_\alpha e_{\alpha j}f_\alpha^{(0)}=\theta. \tag{3.79}$$

The use of equation (3.74) and substitution of equation (3.64) and (3.65) into the above equation result in the continuity equation (2.14). If the density variation is small enough and can be neglected.

Taking $\sum e_{\alpha i}$ [equation (3.75) + $\varepsilon \times$ equation (3.77)] above α yields

$$\frac{\partial}{\partial t}\sum_{\alpha} e_{\alpha i} f_{\alpha}^{(0)} + \frac{\partial \Pi_{ij}^{(0)}}{\partial x_j} = \frac{\partial \Lambda_{ij}}{\partial x_j} + \frac{\Lambda_{ir}}{r} + F_i, \tag{3.80}$$

where Π_{ij}^{0} is the zero-order momentum flux tensor given by the following expressions:

$$\Pi_{ij}^{(0)} = \sum_{\alpha} e_{\alpha i} e_{\alpha j} f_{\alpha}^{(0)}, \tag{3.81}$$

$$\Lambda_{ij} = -\frac{\varepsilon}{2\tau}\left(2\tau - 1\right)\sum_{\alpha} e_{\alpha i} e_{\alpha j} f_{\alpha}^{(1)}, \tag{3.82}$$

and

$$\Lambda_{ij} = -\frac{\varepsilon}{2\tau}\left(2\tau - 1\right)\sum_{\alpha} e_{\alpha i} e_{\alpha r} f_{\alpha}^{(1)}. \tag{3.83}$$

By evaluating the terms in Eq. (3.81) with Eq.(3.54),

$$\Pi_{ij}^{(0)} = p\delta_{ij} + \rho u_i u_j, \tag{3.84}$$

where $p = \rho e^2 / 3$ is the pressure, leading to a sound speed $C_s = e/\sqrt{3}$. Substitution of the above equation into equation (3.80) produces

$$\frac{\partial\left(\rho u_i\right)}{\partial t} + \frac{\partial\left(\rho u_i u_j\right)}{\partial x_j} == \frac{\partial p}{\partial x_i} + \frac{\partial \Lambda_{ij}}{\partial x_j} + \frac{\Lambda_{ir}}{r} + F_i. \tag{3.85}$$

By applying equation (3.75), equation (3.82) can be rewrite as

$$\Lambda_{ij} = \Pi_{ij}^{(1)} - \frac{\varepsilon}{2}\left(2\tau - 1\right)\sum_{\alpha} e_{\alpha i} e_{\alpha r} w_{\alpha} \theta, \tag{3.86}$$

with the first-order momentum flux tensor Π_{ij}^{1} defined by

$$\Pi_{ij}^{(1)} = \frac{\varepsilon}{2}(2\tau - 1)\sum_{\alpha} e_{\alpha i} e_{\alpha r}\left(\frac{\partial}{\partial t} + e_{\alpha k}\frac{\partial}{\partial x_k}\right) f_{\alpha}^{(0)}, \tag{3.87}$$

which can also be written using equation (3.81) as

$$\Pi_{ij}^{(1)} = \frac{\varepsilon}{2}(2\tau - 1)\frac{\partial}{\partial t}\Pi_{ij}^{(0)} + \frac{\varepsilon}{2}(2\tau - 1)\frac{\partial}{\partial x_k}\sum_{\alpha} e_{\alpha i} e_{\alpha r} e_{\alpha k} f_{\alpha}^{(0)}. \tag{3.88}$$

The second term in the above equation can be evaluated with equation (3.54) and (3.74) as

$$\frac{\partial}{\partial x_k}\sum_{\alpha} e_{\alpha i} e_{\alpha r} e_{\alpha k} f_{\alpha}^{(0)} = \frac{e^2}{3}\frac{\partial}{\partial x_k}\left(\rho u_i \delta_{jk} + \rho u_j \delta_{ki} + \rho u_k \delta_{ij}\right). \tag{3.89}$$

If assuming characteristic velocity U_c, length L_c and time t_c, the term $\partial / \partial t \Pi_{ij}^{0}$ is of the order of $\rho U_c^2 / t_c$, and the term $\partial / \partial x_k \sum_a e_{ai} e_{aj} e_{ak} f_a^0$ is of the order of $\rho e^2 U_c^2 / L_c$, based on which we obtain that the ratio of the former to the latter terms has the order of

$$O\left(\frac{\partial / \partial t \Pi_{ij}^{(0)}}{\partial / \partial x_k \sum_{\alpha} e_{\alpha i} e_{\alpha r} e_{\alpha k} f_{\alpha}^{(0)}}\right) = O\left(\frac{\rho U_c^2 / t_c}{\rho e^2 U_c / L_c}\right) = O\left(\frac{U_c}{e}\right)^2 = O\left(\frac{U_c}{C_s}\right)^2 = O(M)^2. \tag{3.90}$$

In which $M = U_c / C_s$ is the Mach number. It following that the first term in equation (3.88) is very small compared with the second term and can be neglected if $M \ll 1$, which is consistent with the lattice Boltzmann dynamics; hence equation (3.88), after equation(3.89) is substituted, becomes

$$\Pi_{ij}^{(1)} = \frac{e^2\varepsilon}{6}\left(2\tau - 1\right)\frac{\partial}{\partial x_k}\left(\rho u_i \delta_{jk} + \rho u_j \delta_{ki} + \rho u_k \delta_{ij}\right), \tag{3.91}$$

or

$$\Pi_{ij}^{(1)} = \nu\left[\frac{\partial\left(\rho u_i\right)}{\partial x_j} + \frac{\partial\left(\rho u_j\right)}{\partial x_i} + \frac{\partial\left(\rho u_k\right)}{\partial x_k}\delta_{ij}\right]. \tag{3.92}$$

In which ν is the kinematic viscosity and defined by:

$$\nu = \frac{e^2\Delta t}{6}\left(2\tau - 1\right). \tag{3.93}$$

The insertion of equation (3.92) into equation (3.86) and evaluation of the rest of the terms of the equation lead to

$$\Lambda_{ij} = \nu\left[\frac{\partial\left(\rho u_i\right)}{\partial x_j} + \frac{\partial\left(\rho u_j\right)}{\partial x_i} + \frac{\partial\left(\rho u_k\right)}{\partial x_k}\delta_{ij}\right] - \nu\theta\delta_{ij}. \tag{3.94}$$

After applying the continuity equation (2.14) and $\theta = -\frac{u_r}{r}$, to the above,

$$\Lambda_{ij} = \nu\left[\frac{\partial\left(\rho u_i\right)}{\partial x_j} + \frac{\partial\left(\rho u_j\right)}{\partial x_i}\right]. \tag{3.95}$$

Also,

$$\Lambda_{ir} = \nu\left[\frac{\partial\left(\rho u_i\right)}{\partial x_r} + \frac{\partial\left(\rho u_r\right)}{\partial x_i}\right]. \tag{3.96}$$

Combining Eqs.(3.58), (3.95) and (3.96) with Eq. (3.85) results in

$$\frac{\partial(\rho u_i)}{\partial t}+\frac{\partial(\rho u_i u_j)}{\partial x_j}=-\frac{\partial p}{\partial x_i}+\nu\frac{\partial}{\partial x_j}\left[\frac{\partial(\rho u_i)}{\partial x_j}+\frac{\partial(\rho u_j)}{\partial x_i}\right] +\frac{\nu}{r}\left[\frac{\partial(\rho u_i)}{\partial r}+\frac{\partial(\rho u_r)}{\partial x_i}\right]-\frac{\rho u_i u_r}{r}-\frac{2\rho\nu u_i}{r^2}\delta_{ij}. \tag{3.97}$$

If the density variation is assumed to be small enough, the above is just the momentum equation(2.17).

3.5.3 Axisymmetric Flows with Swirl

For the axisymmetric rotational flows, the governing equation for an azimuthal velocity in a cylindrical coordinate system is [50]:

$$\frac{\partial u_\phi}{\partial t}+\frac{\partial(u_j u_\phi)}{\partial x_j}=\nu\frac{\partial^2 u_\phi}{\partial x_j^2}+\frac{\nu}{r}\frac{\partial u_\phi}{\partial r}-\frac{2u_r u_\phi}{r}-\frac{\nu u_\phi}{r^2}. \tag{3.98}$$

Its further effect on the flow field is taken into account by adding an additional term to the force term F_i in Eq.(3.58) as

$$F_i=-\frac{\rho u_i u_r}{r}-\frac{2\rho\nu u_i}{r^2}\delta_{ir}+\frac{\rho u_\phi^2}{r}\delta_{ir}. \tag{3.99}$$

It is realized that Eq. (3.98) is an advection-diffusion equation and can be solved accurately and efficiently on either a D2Q4 or D2Q5 lattice Boltzmann model [133,134,135]. The D2Q4 lattice is used in rotation lattice Boltzmann equation for solution to the above equation as:

$$\overline{f_a}(x+\overline{e_a}\Delta t,t+\Delta t)-\overline{f_a}(x,t)=-\overline{\tau_a}(\overline{f_a}-\overline{f_a^{eq}})+\frac{S_\phi\Delta t}{4}, \tag{3.100}$$

where $\overline{f_a}$ is the distribution function; $\overline{f}_a^{eq}$ is the local equilibrium distribution function; S_ϕ is the source or sink term defined by:

$$S_\phi = -\frac{2\rho u_r u_\phi}{r} - \frac{\rho \nu u_\phi}{r^2}; \tag{3.101}$$

$\bar{e}_a$ is the velocity vector of a particle on the D2Q4,

$$\bar{e}_a = e\left[\cos\frac{(\alpha-1)\pi}{2}, \sin\frac{(\alpha-1)\pi}{2}\right], \qquad \alpha = 1,2,3,4; \tag{3.102}$$

and $\overline{\tau_a}$ is also an effective relaxation time associated with the single relaxation time $\bar{\tau}$,

$$\overline{\tau_a} = \begin{cases} \dfrac{1}{=}, & r = 0, \\ \dfrac{1}{=}\left[1 + \dfrac{(2\bar{\tau}-1)\bar{e}_{ar}\Delta t}{2r}\right], & r \neq 0. \end{cases} \tag{3.103}$$

There are many expressions for the $\overline{f}_a^{eq}$ and a simple one is used here:

$$\overline{f}_a^{eq} = \left(1 + \frac{2\bar{e}_{aj}u_j}{e^2}\right)\frac{\rho u_\phi}{4}, \alpha = 1,2,3,4, \tag{3.104}$$

where $e_{\alpha j}$ is the component of $\overline{e_\alpha}$. It is easy to show that the above equation has the following properties:

$$\sum_\alpha \overline{f_\alpha^{eq}} = \rho u_\phi, \tag{3.105}$$

$$\sum_\alpha \overline{e_{\alpha i}}\,\overline{f_\alpha^{eq}} = \rho u_i u_\phi, \tag{3.106}$$

and

$$\sum_{\alpha} \overline{e_{\alpha i}}\,\overline{e_{\alpha j}}\,\overline{f_{\alpha}^{eq}} = \rho e^2 u_{\phi}\delta_{ij} / 2. \tag{3.107}$$

The azimuthal velocity can be calculated as:

$$u_{\phi} = \frac{1}{\rho}\sum_{a} \overline{f}_{a}. \tag{3.108}$$

3.5.4 Recovery of Axisymmetric Lattice Boltzmann Equation with Swirl

In order to prove that Eq. (3.98) can be recovered from the lattice Boltzmann equation (3.100), the similar Chapman-Enskog analysis was applied to that given in Sec. 3.3.2 and, after taking a Taylor expansion to Eq. (3.100) in time and space at point (x,t),

$$\begin{aligned}\varepsilon\left(\frac{\partial}{\partial t}+\bar{e}_{\alpha j}\frac{\partial}{\partial x_j}\right)\overline{f}_{\alpha}+\frac{1}{2}\varepsilon^2\left(\frac{\partial}{\partial t}+\bar{e}_{\alpha j}\frac{\partial}{\partial x_j}\right)^2\overline{f}_{\alpha}+O\left(\varepsilon^3\right)= \\ -\frac{1}{\tau}\left(\overline{f}_{\alpha}-\overline{f}_{\alpha}^{eq}\right)-\frac{\left(2\bar{\tau}-1\right)}{2\bar{\tau}r}\bar{e}_{\alpha r}\varepsilon\left(\overline{f}_{\alpha}-\overline{f}_{\alpha}^{eq}\right)+\frac{S_{\phi}}{4}\varepsilon.\end{aligned} \tag{3.109}$$

The centred scheme (3.80) is used again for the term S_{ϕ},

$$S_{\phi} = S_{\phi}\left(x+\frac{1}{2}\bar{e}_{\alpha}\varepsilon, t+\frac{1}{2}\varepsilon\right), \tag{3.110}$$

which is further written, via a Taylor expansion, as

$$S_{\phi}\left(x+\frac{1}{2}\bar{e}_{\alpha}\varepsilon, t+\frac{1}{2}\varepsilon\right) = S_{\phi}\left(x,t\right)+\frac{1}{2}\varepsilon\left(\frac{\partial}{\partial t}+\bar{e}_{\alpha i}\frac{\partial}{\partial x_i}\right)S_{\phi}\left(x,t\right)+O\left(\varepsilon^2\right). \tag{3.111}$$

After substitution of Eq. (3.69) and (3.111) into (3.109), Eq.(3.109) to the order of ε^0 is

$$\overline{f}_{\alpha}^{(0)} = \overline{f}_{\alpha}^{eq} \tag{3.112}$$

to the order of ε is

$$\left(\frac{\partial}{\partial t} + \bar{e}_{\alpha j}\frac{\partial}{\partial x_j}\right)\overline{f}_{\alpha}^{(0)} = -\frac{\overline{f}_{\alpha}^{(1)}}{\bar{\tau}} + \frac{S_{\phi}}{4}. \tag{3.113}$$

and to the order ε^2 is

$$\begin{aligned}\left(\frac{\partial}{\partial t} + \bar{e}_{\alpha j}\frac{\partial}{\partial x_j}\right)\overline{f}_{\alpha}^{(1)} + \frac{1}{2}\left(\frac{\partial}{\partial t} + \bar{e}_{\alpha j}\frac{\partial}{\partial x_j}\right)^2\overline{f}_{\alpha}^{(0)} = \\ -\frac{\overline{f}_{\alpha}^{(2)}}{\bar{\tau}} - \frac{\left(2\bar{\tau}-1\right)}{2\bar{\tau}r}\bar{e}_{\alpha r}\overline{f}_{\alpha}^{(1)} + \frac{1}{2}\left(\frac{\partial}{\partial t} + \bar{e}_{\alpha i}\frac{\partial}{\partial x_i}\right)\frac{S_{\phi}}{4}.\end{aligned} \tag{3.114}$$

The substitution of Eq.(3.113) into the above equation gives

$$\frac{\left(2\bar{\tau}-1\right)}{2\bar{\tau}r}\left(\frac{\partial}{\partial t} + \bar{e}_{\alpha j}\frac{\partial}{\partial x_j}\right)\overline{f}_{\alpha}^{(1)} = -\frac{\overline{f}_{\alpha}^{(2)}}{\bar{\tau}} - \frac{\left(2\bar{\tau}-1\right)}{2\bar{\tau}r}\bar{e}_{\alpha r}\overline{f}_{\alpha}^{(1)}. \tag{3.115}$$

Taking $\sum$[Eq.(3.113)+ $\varepsilon\times$ Eq.(3.115)] yields

$$\frac{\partial}{\partial t}\sum_{\alpha}\overline{f}_{\alpha}^{(0)} + \frac{\partial}{\partial x_i}\sum_{\alpha}\bar{e}_{\alpha i}\overline{f}_{\alpha}^{(0)} = \frac{\partial\Gamma_i}{\partial x_i} + \frac{\Gamma_r}{r} + S_{\phi}, \tag{3.116}$$

where

$$\Gamma_i = -\frac{\left(2\bar{\tau}-1\right)\varepsilon}{2\bar{\tau}}\sum_{\alpha}\bar{e}_{\alpha i}\overline{f}_{\alpha}^{(1)}, \tag{3.117}$$

and

$$\Gamma_r = -\frac{\left(2\bar{\tau}-1\right)\varepsilon}{2\bar{\tau}}\sum_{\alpha}\bar{e}_{\alpha r}\overline{f}_{\alpha}^{(1)}. \tag{3.118}$$

Inserting Eq. (3.113) into Eq. (3.117) leads to

$$\Gamma_i = -\frac{\varepsilon}{2}\left(2\bar{\tau}-1\right)\sum_{\alpha}\bar{e}_{\alpha i}\left(\frac{\partial}{\partial t}+\bar{e}_{\alpha j}\frac{\partial}{\partial x_j}\right)\overline{f}_{\alpha}^{(0)}, \tag{3.119}$$

or

$$\Gamma_i = -\frac{\varepsilon}{2}\left(2\bar{\tau}-1\right)\left(\frac{\partial}{\partial t}\sum_{\alpha}\bar{e}_{\alpha i}f_{\alpha}^{(0)}+\frac{\partial}{\partial x_j}\sum_{\alpha}\bar{e}_{\alpha i}\bar{e}_{\alpha j}\overline{f}_{\alpha}^{(0)}+\right). \tag{3.120}$$

The order analysis indicates that $\partial/\partial t\sum_{\alpha}\bar{e}_{\alpha i}\overline{f}_{\alpha}^{(0)}$ has the order of $\rho U_c^2/t_c$ from Eq.(3.106) and $\partial/\partial x_j\sum_{\alpha}\bar{e}_{\alpha i}\bar{e}_{\alpha j}\overline{f}_{\alpha}^{(0)}$ has the order $\rho e^2 U_c/L_c$ from Eq.(3.107), based on which the ratio of the former to the latter has the order of

$$\begin{aligned} &O\left(\frac{\partial/\partial t\sum_{\alpha}\bar{e}_{\alpha i}\overline{f}_{\alpha}^{(0)}}{\partial/\partial x_j\sum_{\alpha}\bar{e}_{\alpha i}\bar{e}_{\alpha j}\overline{f}_{\alpha}^{(0)}}\right)=O\left(\frac{\rho U_c^2/t_c}{\rho e^2 U_c/L_c}\right)= \\ &O\left(\frac{U_c}{e}\right)^2=O\left(\frac{U_c}{C_s}\right)^2=O\left(M^2\right). \end{aligned} \tag{3.121}$$

This suggests that the first term in Eq. (3.120) is much smaller compared to the second and can be dropped if $M<<1$, which again conforms to the lattice Boltzmann method; hence Eq.(3.120) can be approximated by

$$\Gamma_i = -\frac{\varepsilon}{2}\left(2\bar{\tau}-1\right)\frac{\partial}{\partial x_j}\sum_{\alpha}\bar{e}_{\alpha i}\bar{e}_{\alpha j}\overline{f}_{\alpha}^{(0)}. \tag{3.122}$$

By applying Eq.(3.107) into above,

$$\Gamma_i = \bar{\nu}\frac{\partial\left(\rho u_{\phi}\right)}{\partial x_i}. \tag{3.123}$$

in which $\bar{v}$ is the kinematic viscosity defined by

$$\bar{v} = \frac{e^2 \Delta t}{4}\left(2\bar{\tau} - 1\right). \tag{3.124}$$

Similarly,

$$\Gamma_i = \bar{v}\frac{\partial\left(\rho u_\phi\right)}{\partial r}. \tag{3.125}$$

The substitution of Eqs.(3.105), (3.106), (3.123), and (3.125) into Eq. (3.116) results in the governing equation (3.98) if the density variation is assumed to be small enough.

Consistency in the hydrodynamics requires the same kinematic viscosity, $\bar{v} = v$, which leads to

$$\bar{v} = \frac{1}{2} + \frac{1}{3}\left(2\tau - 1\right). \tag{3.126}$$

As seen from the above formulas, there is no calculation for a velocity gradient in the procedure and the added source or sink term is the same as that in the governing equation without the velocity gradient.

3.6 Stability conditions

The lattice Boltzmann equation is a discrete form of a numerical method. It also suffered from a numerical instability like any other numerical methods. Theoretically, the stability conditions are not known for the method. Generally, most of computational methods have shown that the method is often stable when some basic conditions are satisfied.

The lattice Boltzmann equation simulates the physical water flow, so the diffusion phenomena should be present. This implies that the kinematic viscosity v should be positive [130], i.e. from Eq.(3.93) :

$$v = \frac{e^2 \Delta t}{6}\left(2\tau - 1\right) > 0. \tag{3.127}$$

Thus an apparent constraint on the relaxation time is

$$\tau > \frac{1}{2}. \tag{3.128}$$

It should be point out that these conditions can be easily satisfied by using suitable values for the relaxation time. Also the time step should obey this relation:

$$\Delta t = \frac{dx}{e} \tag{3.129}$$

Normally, the lattice velocity e should not set too much larger than the flow velocity. Thus, the axisymmetric lattice Boltzmann method is stable as this condition is satisfied.

Chapter 4: Simulation of Non-Newtonian Fluids

4.1 Introduction

The majority of studies on the CFD focused on the Newtonian behaviour. However, in numerous engineering applications such as oil drilling and journal-bearing lubrication, the fluids often show a different behaviour from Newtonian fluid. Hence, a growing number of researchers take into account the rheological aspect by considering non-Newtonian fluids. Non-Newtonian fluids have a viscosity that is a function of shear rate. The viscosity of such fluids exhibits a non-linear relationship between shear stress and shear rate. In general all liquids exhibit a non-Newtonian character at certain shear rates, with Newtonian fluids being a sub class of non-Newtonian fluids. In this chapter, a general power-law model will be presented and combined with the AxLAB® to simulate non-Newtonian fluid flow.

4.2 AxLAB® for non-Newtonian Fluids Simulation

For non-Newtonian fluids, it is a common practice to adopt the power-law model for the effective viscosity ν_m, which is defined using the local shear rate γ and the Newtonian fluid viscosity ν as,

$$\nu_m = \nu |\gamma|^{(n-1)}, \tag{4.1}$$

where n is the power-law exponent. In the theory, when $n=1$ Eq. (4.1) describes the Newtonian fluid. When $0<n<1$, the effective viscosity reduces with the fluid shear rate which is called “shear-thinning” or “pseudoplastic” fluid. When $n>1$, the effective viscosity increases with the shear rate, and the fluid called “shear-thickening” or “dilatant” fluid. In the present study, the relationship of the shear rate is defined by Khali *et al.*, [137]

$$\gamma = 2\left[\left(\frac{\partial u_r}{\partial r}\right)^2 + \left(\frac{u_r}{r}\right)^2 + \left(\frac{\partial u_z}{\partial z}\right)^2\right] + \left[r\frac{\partial}{\partial r}\left(\frac{u_\phi}{r}\right)\right]^2 + \left(\frac{\partial u_\phi}{\partial z}\right)^2 + \left(\frac{\partial u_r}{\partial z} + \frac{\partial u_z}{\partial r}\right)^2. \tag{4.2}$$

In order to simulate non-Newtonian fluid flows, replace the relaxation time τ in the AxLAB® using Eq. (3.93) with τ_m given by

$$\tau_m = \frac{3\nu_m}{e^2\Delta t} + \frac{1}{2}. \tag{4.3}$$

In addition, the force term for non-Newtonian fluid is accordingly changed to

$$F_{im} = -\frac{\rho u_i u_r}{r} - \frac{2\rho\nu_m u_i}{r^2}\delta_{ir}. \tag{4.4}$$

By using the similar Chapman-Enskog analysis to that described by Zhou [50], the following incompressible non-Newtonian axisymmetric flows equations can be recovered from the lattice Boltzmann equation (3.56) using τ_m.

$$f_\alpha\left(x + e_\alpha\Delta t, t + \Delta t\right) - f_\alpha\left(x,t\right) = -\tau_\alpha\left(f_\alpha - f_\alpha^{eq}\right) + \omega_\alpha\theta\Delta t + \frac{\Delta t}{\mathcal{K}e^2}e_{\alpha i}F_{im}, \tag{4.5}$$

in which τ_α is the relaxation time and for the non-Newtonian fluid can be written as:

$$\tau_\alpha = \begin{cases} \dfrac{1}{\tau_m}, & r = 0, \\ \dfrac{1}{\tau_m}\left[1 + \dfrac{\left(2\tau_m - 1\right)e_{\alpha r}\Delta t}{2r}\right], & r \neq 0. \end{cases} \tag{4.6}$$

4.3 Recovery of the Axisymmetric Flow Equations for non-Newtonian Fluids

Similar to the former section, the Chapman-Enskog analysis is applied to show that the macroscopic equations (2.14) and (4.7)

$$\frac{\partial u_i}{\partial t}+\frac{\partial (u_i u_j)}{\partial x_j}=-\frac{1}{\rho}\frac{\partial p}{\partial x_i}+\nu_m\frac{\partial}{\partial x_j}\left(\frac{\partial u_i}{\partial x_j}+\frac{\partial u_j}{\partial x_i}\right) + \frac{\nu_m}{r}\left(\frac{\partial u_i}{\partial r}+\frac{\partial u_r}{\partial x_i}\right)-\frac{u_i u_r}{r}-\frac{2\nu_m u_i}{r^2}\delta_{ir}, \tag{4.7}$$

can be derived from the lattice Boltzmann equation(4.5). Assuming Δt is small and equal to ε,

$$\Delta t=\varepsilon. \tag{4.8}$$

Noting Eq.(3.62), substitute the above equation into Eq.(3.56) and obtain

$$f_\alpha\left(x+e_\alpha\varepsilon,t+\varepsilon\right)-f_\alpha\left(x,t\right) =-\frac{1}{\tau_m}\left(f_\alpha-f_\alpha^{eq}\right)-\frac{\left(2\tau_m-1\right)}{2\tau r}e_{\alpha r}\varepsilon\left(f_\alpha-f_\alpha^{eq}\right)+w_\alpha\theta\varepsilon+\frac{\varepsilon}{6e^2}e_{\alpha i}F_i. \tag{4.9}$$

By taking a Taylor expansion to Eq.(4.9) in time and space at point $\left(x,t\right)$, have

$$\varepsilon\left(\frac{\partial}{\partial t}+e_{\alpha j}\frac{\partial}{\partial x_j}\right)f_\alpha+\frac{1}{2}\varepsilon^2\left(\frac{\partial}{\partial t}+e_{\alpha j}\frac{\partial}{\partial x_j}\right)^2 f_\alpha+O\left(\varepsilon^3\right) =-\frac{1}{\tau_m}\left(f_\alpha-f_\alpha^{eq}\right)-\frac{\left(2\tau_m-1\right)}{2\tau_m r}e_{\alpha r}\varepsilon\left(f_\alpha-f_\alpha^{eq}\right)+\varepsilon w_\alpha\theta+\frac{\varepsilon}{6e^2}e_{\alpha i}F_i. \tag{4.10}$$

According to the Chapman-Enskog expansion, f_α can be written in a series of ε,

$$f_\alpha=f_\alpha^{(0)}+\varepsilon f_\alpha^{(1)}+\varepsilon^2 f_\alpha^{(2)}+O\left(\varepsilon^3\right). \tag{4.11}$$

The centred scheme is used for both source term θ and force term F_i as

$$\theta = \theta\left(x + \frac{1}{2} e_\alpha \varepsilon, t + \frac{1}{2}\varepsilon \right) \tag{4.12}$$

and

$$F_i = F_i\left(x + \frac{1}{2} e_\alpha \varepsilon, t + \frac{1}{2}\varepsilon \right). \tag{4.13}$$

which can also be written, via a Taylor expansion, as

$$\theta\left(x + \frac{1}{2} e_\alpha \varepsilon, t + \frac{1}{2}\varepsilon \right) = \theta(x,t) + \frac{1}{2}\varepsilon\left(\frac{\partial}{\partial t} + e_{\alpha j}\frac{\partial}{\partial x_j} \right)\theta(x,t) + O\left(\varepsilon^2\right) \tag{4.14}$$

and

$$F_i\left(x + \frac{1}{2} e_\alpha \varepsilon, t + \frac{1}{2}\varepsilon \right) = F_i(x,t) + \frac{1}{2}\varepsilon\left(\frac{\partial}{\partial t} + e_{\alpha j}\frac{\partial}{\partial x_j} \right)F_i(x,t) + O\left(\varepsilon^2\right). \tag{4.15}$$

After substitution of Eq.(4.11), (4.14) and (4.15) into Eq.(4.10), the equation to the order of ε^0 is

$$f_\alpha^{(0)} = f_\alpha^{eq}, \tag{4.16}$$

to the order of ε is

$$\left(\frac{\partial}{\partial t} + e_{\alpha j}\frac{\partial}{\partial x_j} \right) f_\alpha^{(0)} = -\frac{f_\alpha^{(1)}}{\tau_m} + w_\alpha \theta + \frac{1}{6e^2} e_{\alpha i} F_i, \tag{4.17}$$

and to the order of ε^2 is

$$\left(\frac{\partial}{\partial t}+e_{\alpha j}\frac{\partial}{\partial x_j}\right)f_\alpha^{(1)}+\frac{1}{2}\varepsilon^2\left(\frac{\partial}{\partial t}+e_{\alpha j}\frac{\partial}{\partial x_j}\right)^2 f_\alpha^{(0)}=-\frac{f_\alpha^{(2)}}{\tau_m}-\frac{(2\tau_m-1)}{2\tau_m r}e_{\alpha r}f_\alpha^{(1)}$$
$$+\frac{1}{2}\left(\frac{\partial}{\partial t}+e_{\alpha j}\frac{\partial}{\partial x_j}\right)(w_\alpha\theta)+\frac{1}{12e^2}\left(\frac{\partial}{\partial t}+e_{\alpha j}\frac{\partial}{\partial x_j}\right)(e_{\alpha i}F_i). \tag{4.18}$$

By using Eq.(4.17), the above equation can be written as

$$\frac{(2\tau_m-1)}{2\tau_m}\left(\frac{\partial}{\partial t}+e_{\alpha j}\frac{\partial}{\partial x_j}\right)f_\alpha^{(1)}=-\frac{f_\alpha^{(2)}}{\tau_m}-\frac{(2\tau_m-1)}{2\tau_m}e_{\alpha r}f_\alpha^{(1)}. \tag{4.19}$$

From Eq.(4.17) + $\varepsilon\times$ Eq.(4.19),

$$\left(\frac{\partial}{\partial t}+e_{\alpha j}\frac{\partial}{\partial x_j}\right)f_\alpha^{(0)}+\frac{(2\tau_m-1)\varepsilon}{2\tau_m}\left(\frac{\partial}{\partial t}+e_{\alpha j}\frac{\partial}{\partial x_j}\right)f_\alpha^{(1)}$$
$$=-\frac{1}{\tau_m}\left(f_\alpha^{(1)}-\varepsilon f_\alpha^{(2)}\right)-\frac{(2\tau_m-1)\varepsilon}{2\tau_m}e_{\alpha r}f_\alpha^{(1)}+w_\alpha\theta+\frac{1}{6e^2}e_{\alpha i}F_i. \tag{4.20}$$

The summation of the above equation over α provides

$$\frac{\partial}{\partial t}\sum_\alpha f_\alpha^{(0)}+\frac{\partial}{\partial x_j}\sum_\alpha e_{\alpha j}f_\alpha^{(0)}=\theta. \tag{4.21}$$

The use of equation (4.16) and substitution of equation (3.64) and (3.65) into the above equation result in the continuity equation (2.14). If the density variation is small enough and can be neglected.

Taking $\sum e_{\alpha i}$ [equation (4.17) + $\varepsilon\times$ equation(4.19)] above α yields

$$\frac{\partial}{\partial t}\sum_\alpha e_{\alpha i}f_\alpha^{(0)}+\frac{\partial\Pi_{ij}^{(0)}}{\partial x_j}=\frac{\partial\Lambda_{ij}}{\partial x_j}+\frac{\Lambda_{ir}}{r}+F_i, \tag{4.22}$$

where Π_{ij}^0 is the zero-order momentum flux tensor given by the following expressions:

$$\Pi_{ij}^{(0)} = \sum_{\alpha} e_{\alpha i} e_{\alpha j} f_{\alpha}^{(0)}, \tag{4.23}$$

$$\Lambda_{ij} = -\frac{\varepsilon}{2\tau_m}\left(2\tau_m - 1\right)\sum_{\alpha} e_{\alpha i} e_{\alpha j} f_{\alpha}^{(1)}, \tag{4.24}$$

and

$$\Lambda_{ij} = -\frac{\varepsilon}{2\tau_m}\left(2\tau_m - 1\right)\sum_{\alpha} e_{\alpha i} e_{\alpha r} f_{\alpha}^{(1)}. \tag{4.25}$$

By evaluating the terms in Eq. (4.23) with Eq.(3.54),

$$\Pi_{ij}^{(0)} = p\delta_{ij} + \rho u_i u_j, \tag{4.26}$$

Where $p = \rho e^2 / 3$ is the pressure, leading to a sound speed $C_s = e/\sqrt{3}$. Substitution of the above equation into equation (4.22) produces

$$\frac{\partial\left(\rho u_i\right)}{\partial t} + \frac{\partial\left(\rho u_i u_j\right)}{\partial x_j} == \frac{\partial p}{\partial x_i} + \frac{\partial \Lambda_{ij}}{\partial x_j} + \frac{\Lambda_{ir}}{r} + F_i. \tag{4.27}$$

By applying equation(4.17), equation (4.24) can be rewrite as

$$\Lambda_{ij} = \Pi_{ij}^{(1)} - \frac{\varepsilon}{2}\left(2\tau_m - 1\right)\sum_{\alpha} e_{\alpha i} e_{\alpha r} w_{\alpha}\theta, \tag{4.28}$$

With the first-order momentum flux tensor Π_{ij}^{1} defined by

$$\Pi_{ij}^{(1)} = \frac{\varepsilon}{2}\left(2\tau_m - 1\right)\sum_{\alpha} e_{\alpha i} e_{\alpha r}\left(\frac{\partial}{\partial t} + e_{\alpha k}\frac{\partial}{\partial x_k}\right) f_{\alpha}^{(0)}, \tag{4.29}$$

which can also be written using equation (4.23) as

$$\Pi_{ij}^{(1)} = \frac{\varepsilon}{2}(2\tau_m - 1)\frac{\partial}{\partial t}\Pi_{ij}^{(0)} + \frac{\varepsilon}{2}(2\tau_m - 1)\frac{\partial}{\partial x_k}\sum_{\alpha} e_{\alpha i}e_{\alpha r}e_{\alpha k} f_{\alpha}^{(0)}. \tag{4.30}$$

The second term in the above equation can be evaluated with equation (3.54) and (4.16) as

$$\frac{\partial}{\partial x_k}\sum_{\alpha} e_{\alpha i}e_{\alpha r}e_{\alpha k} f_{\alpha}^{(0)} = \frac{e^2}{3}\frac{\partial}{\partial x_k}\left(\rho u_i\delta_{jk} + \rho u_j\delta_{ki} + \rho u_k\delta_{ij}\right). \tag{4.31}$$

If assuming characteristic velocity U_c, length L_c and time t_c, the term $\partial/\partial t\Pi_{ij}^0$ is of the order of $\rho U_c^2/t_c$, and the term $\partial/\partial x_k\sum_a e_{ai}e_{aj}e_{ak}f_a^0$ is of the order of $\rho e^2 U_c^2/L_c$, based on which we obtain that the ratio of the former to the latter terms has the order of

$$O\left(\frac{\partial/\partial t\Pi_{ij}^{(0)}}{\partial/\partial x_k\sum_{\alpha} e_{\alpha i}e_{\alpha r}e_{\alpha k}f_{\alpha}^{(0)}}\right) = O\left(\frac{\rho U_c^2/t_c}{\rho e^2 U_c/L_c}\right) = O\left(\frac{U_c}{e}\right)^2 = O\left(\frac{U_c}{C_s}\right)^2 = O(M)^2. \tag{4.32}$$

In which $M = U_c/C_s$ is the Mach number. It following that the first term in equation (4.30) is very small compared with the second term and can be neglected if $M \ll 1$, which is consistent with the lattice Boltzmann dynamics; hence equation(4.30), after equation(4.31) is substituted, becomes

$$\Pi_{ij}^{(1)} = \frac{e^2\varepsilon}{6}(2\tau_m - 1)\frac{\partial}{\partial x_k}\left(\rho u_i\delta_{jk} + \rho u_j\delta_{ki} + \rho u_k\delta_{ij}\right), \tag{4.33}$$

or

$$\Pi_{ij}^{(1)} = \nu_m\left[\frac{\partial(\rho u_i)}{\partial x_j} + \frac{\partial(\rho u_j)}{\partial x_i} + \frac{\partial(\rho u_k)}{\partial x_k}\delta_{ij}\right]. \tag{4.34}$$

in which ν_m is the kinematic viscosity and defined by Eq.(4.1).

The insertion of equation (4.34) into equation (4.28) and evaluation of the rest of the terms of the equation lead to

$$\Lambda_{ij} = \nu_m \left[\frac{\partial(\rho u_i)}{\partial x_j} + \frac{\partial(\rho u_j)}{\partial x_i} + \frac{\partial(\rho u_k)}{\partial x_k} \delta_{ij} \right] - \nu_m \theta \delta_{ij}. \tag{4.35}$$

After applying the continuity equation (2.14) and $\theta = -\frac{u_r}{r}$, to the above, can obtain

$$\Lambda_{ij} = \nu_m \left[\frac{\partial(\rho u_i)}{\partial x_j} + \frac{\partial(\rho u_j)}{\partial x_i} \right]. \tag{4.36}$$

Also,

$$\Lambda_{ir} = \nu_m \left[\frac{\partial(\rho u_i)}{\partial x_r} + \frac{\partial(\rho u_r)}{\partial x_i} \right]. \tag{4.37}$$

Combining Eqs.(3.58), (4.36)and (4.37) with Eq. (4.27)results in

$$\begin{aligned} \frac{\partial(\rho u_i)}{\partial t} + \frac{\partial(\rho u_i u_j)}{\partial x_j} = -\frac{\partial p}{\partial x_i} + \nu_m \frac{\partial}{\partial x_j} \left[\frac{\partial(\rho u_i)}{\partial x_j} + \frac{\partial(\rho u_j)}{\partial x_i} \right] \\ + \frac{\nu_m}{r} \left[\frac{\partial(\rho u_i)}{\partial r} + \frac{\partial(\rho u_r)}{\partial x_i} \right] - \frac{\rho u_i u_r}{r} - \frac{2\rho \nu_m u_i}{r^2} \delta_{ij}. \end{aligned} \tag{4.38}$$

If the density variation is assumed to be small enough, the above is just the momentum equation (4.7).

Chapter 5: Large Eddy Simulation for Turbulent Flows

5.1 Introduction

Most axisymmetric lattice Boltzmann methods in literature are reported for laminar axisymmetric flow equations without flow turbulence. As most practical flows in nature are turbulent, these methods cannot be directly applied. Generally, flow turbulence can be modelled by using additional scheme such as the model in modified laminar flow equations such as time-averaged or space-filtered flow equations. Teixeira [52] presented a lattice Boltzmann method for turbulent flows: the single relaxation time is modified as a variable relaxation time which is decided by solution of the two differential equations, $k-\varepsilon$ equations. As an alternative method, the large eddy simulation can efficiently simulate vorticity larger than a prescribed scale, where space-filtered governing equations with a subgird-scale (SGS) stress model for the unresolved scale stress are used. The simplest and most accurate model in this class is developed by Smagorinsky [53], who expressed the Reynolds stress tensor by using the eddy viscosity and a large-scale strain tensor. According to the previous research [54], the space-filtered flow equations are more accurate for turbulent flows and so are used in the present study. Hou *et al*. [55] demonstrate that the standard Smagorinsky SGS stress model can be incorporated into the lattice Boltzmann method for turbulence modelling. Meantime, the single relaxation time is modified as a variable relaxation time which is directly linked with the distribution function and can be eliminating any calculations of derivatives. In this chapter, the similar idea was applied to develop an axisymmetric LBM for turbulence modelling. The general methods for turbulent flows modelling are briefly reviewed first. Then the subgrid-scale stress model for turbulent axisymmetric flows is introduced. Finally the recovery of the AxLAB® with turbulence is recovered from the axisymmetric flow governing equations.

5.2 AxLAB® with the Subgrid-Scale Stress Model (SGS)

Most practical flows in nature with high Reynolds numbers are far to be directly simulated with current computer capacity. This problem rise the challenge of predicting the behaviour of highly turbulent flows without directly simulating all scales of motion. The large eddy simulation using a subgrid-scale stress model is a powerful tool within this problem. The simplest and most popular method in this topic is developed by Smagorinsky [53], who uses the eddy viscosity and a large-scale strain tensor to express the Reynolds stress tensor. According to the research by Tutar and Hold [54], space-filtered flow equations are more accurate than the time-averaged ones for the calculation of turbulent flows and so are used in the present study.

Zhou has developed an axisymmetric lattice Boltzmann model for the axisymmetric flow equations (AxLAB®) without turbulence modelling [50] which presented in chapter 3. In this section, the AxLAB® was extended to include turbulence modelling. By comparing the axisymmetric flow Eqs. (2.14) and (2.15), and the turbulent axisymmetric flow Eqs.(2.43) and (2.44), it can be noticed that the only difference between them are the viscous terms. In the turbulent axisymmetric flow equations the viscous term has an additional viscosity concerning the eddies, which is not included in general axisymmetric flow equations. The kinematic viscosity ν is defined only by the relaxation time from Eq.(3.63). For the turbulence modelling using the eddy viscosity,

$$\nu_e = \tau_e \cdot \frac{e^2 \Delta t}{3}, \tag{5.1}$$

a new relaxation time τ_t is defined as:

$$\tau_t = \tau_\alpha + \tau_e, \tag{5.2}$$

A total viscosity ν_t is defined by

$$\nu_t = \nu + \nu_e. \tag{5.3}$$

Therefore, the lattice Boltzmann equation with the total relaxation time τ_t can be written as:

$$f_\alpha\left(x+e_\alpha\Delta t,t+\Delta t\right)-f_\alpha\left(x,t\right)=-\tau_{\alpha t}\left(f_\alpha-f_\alpha^{eq}\right)+\omega_\alpha\theta\Delta t+\frac{\Delta t}{\mathcal{K}e^2}e_{\alpha i}F_i, \tag{5.4}$$

where

$$\tau_{\alpha t}=\begin{cases}\dfrac{1}{\tau_t}, & r=0,\\ \dfrac{1}{\tau_t}\left[1+\dfrac{\left(2\tau_t-1\right)e_{\alpha r}\Delta t}{2r}\right], & r\neq 0.\end{cases} \tag{5.5}$$

and

$$F_i=-\frac{\rho u_i u_r}{r}-\frac{2\rho\nu_t u_i}{r^2}\delta_{ir}, \tag{5.6}$$

By using this equation, the solution to the turbulent axisymmetric flow equation can be obtain, i.e. Eqs.(2.43) and (2.44). This is the basic idea behind the lattice Boltzmann method coupled with a subgrid-scale stress model proposed by Hou *et al*. [55]. In this way, the flow turbulence can be modelled simply and efficiently in the lattice Boltzmann equation without any changes in its standard form.

Next, the total relaxation time τ_t will be defined. As Eq. (2.41) defines, the strain-rate tensor S_{ij} involves calculation of derivatives which is not suitable to use. To keep the consistency with the lattice gas dynamics, it is natural to calculate S_{ij} in terms of the distribution function. By using the Chapman-Enskog expansion, it can be found that the strain-rate tensor S_{ij} is related to the non-equilibrium momentum flux tensor that is described in Section 4.3, so it is convenient to calculate S_{ij} by

$$S_{ij}=-\frac{3}{2e^2\rho\tau_t\Delta t}\sum_\alpha e_{\alpha i}e_{\alpha j}\left(f_\alpha-f_\alpha^{eq}\right). \tag{5.7}$$

If assuming ν_t and τ_t also satisfy the relation as Eq.(3.63), the following equation can be obtained,

$$\tau_t = \frac{1}{2} + \frac{3\nu_t}{e^2 \Delta t}. \tag{5.8}$$

Substitution of Eqs. (5.2) and (5.3) into Eq. (5.8) leads to

$$\tau_e + \tau = \frac{1}{2} + \frac{3(\nu_e + \nu)}{e^2 \Delta t}. \tag{5.9}$$

Substitution of Eq. (3.63) into the above equation leads to

$$\tau_e = \frac{3}{e^2 \Delta t} \nu_e. \tag{5.10}$$

Substitution of Eq. (2.40) into the above equation gives

$$\tau_e = \frac{3}{e^2 \Delta t} (C_s l_s)^2 \sqrt{S_{ij} S_{ij}}. \tag{5.11}$$

If Eq. (5.7) is substituted into above equation, τ_e can be further expressed as

$$\tau_e = \frac{3}{e^2 \Delta t} (C_s l_s)^2 \frac{3}{2e^2 \rho \tau_t \Delta t} \sqrt{\Pi_{ij} \Pi_{ij}}, \tag{5.12}$$

where

$$\Pi_{ij} = \sum_{\alpha} e_{\alpha i} e_{\alpha j} \left(f_\alpha - f_\alpha^{eq} \right). \tag{5.13}$$

If $l_s = \Delta t$ is adopted and Eq. (5.2) is referred, Eq. (5.12) is

$$\tau_e = \frac{9 C_s^2}{2e^2 \rho (\tau + \tau_e)} \sqrt{\Pi_{ij} \Pi_{ij}}, \tag{5.14}$$

Finally, solution of the above equation and ignoring the minus value of τ_e, the eddy relaxation time can be obtained,

$$\tau_e = \frac{-\tau + \sqrt{\tau^2 + 18C_s{}^2/\left(e^2\rho\right)\sqrt{\Pi_{ij}\Pi_{ij}}}}{2}, \tag{5.15}$$

hence giving the following total relaxation time τ_t via Eq. (5.2)

$$\tau_t = \frac{\tau + \sqrt{\tau^2 + 18C_s{}^2/\left(e^2\rho\right)\sqrt{\Pi_{ij}\Pi_{ij}}}}{2}. \tag{5.16}$$

As the solution of the lattice Boltzmann equation (3.56) is the solution to the axisymmetric flow equations (2.14) and (2.15), the flow turbulence can be simply and naturally modelled in the standard lattice Boltzmann equation with total relaxation time τ_t which includes the eddy relaxation time τ_e form Eq. (5.2). By using Chapman-Enskog analysis, the 2D incompressible axisymmetric turbulent flow equations Eqs. (2.14) and (5.17) can be recovered from the lattice Boltzmann equation (3.56) .

$$\frac{\partial u_i}{\partial t} + \frac{\partial (u_i u_j)}{\partial x_j} = -\frac{1}{\rho}\frac{\partial p}{\partial x_i} + \upsilon_t \frac{\partial}{\partial x_j}\left(\frac{\partial u_i}{\partial x_j} + \frac{\partial u_j}{\partial x_i}\right) + \frac{\upsilon_t}{r}\left(\frac{\partial u_i}{\partial r} + \frac{\partial u_r}{\partial x_i}\right) - \frac{u_i u_r}{r} - \frac{2\upsilon_t u_i}{r^2}\delta_{ir}. \tag{5.17}$$

5.3 Recovery of the AxLAB® with Turbulence

Similar to Section 3.3.2, the procedure used to recover the turbulent axisymmetric flow equations (2.43) and (2.44) from the lattice Boltzmann equation (5.4) is described in this section. Assuming Δt is small and equal to ε,

$$\Delta t = \varepsilon. \tag{5.18}$$

Noting Eq.(5.5), substitute the above equation into Eq.(5.4) and obtain

$$
\begin{aligned}
&f_\alpha\left(x+e_\alpha\varepsilon,t+\varepsilon\right)-f_\alpha\left(x,t\right)\\
&=-\frac{1}{\tau_t}\left(f_\alpha-f_\alpha^{eq}\right)-\frac{\left(2\tau_t-1\right)}{2\tau_t r}e_{\alpha r}\varepsilon\left(f_\alpha-f_\alpha^{eq}\right)+w_\alpha\theta\varepsilon+\frac{\varepsilon}{6e^2}e_{\alpha i}F_i.
\end{aligned}
\tag{5.19}
$$

By taking a Taylor expansion to Eq.(5.19) in time and space at point (x,t),

$$
\begin{aligned}
&\varepsilon\left(\frac{\partial}{\partial t}+e_{\alpha j}\frac{\partial}{\partial x_j}\right)f_\alpha+\frac{1}{2}\varepsilon^2\left(\frac{\partial}{\partial t}+e_{\alpha j}\frac{\partial}{\partial x_j}\right)^2 f_\alpha+O\left(\varepsilon^3\right)\\
&=-\frac{1}{\tau_t}\left(f_\alpha-f_\alpha^{eq}\right)-\frac{\left(2\tau_t-1\right)}{2\tau_t r}e_{\alpha r}\varepsilon\left(f_\alpha-f_\alpha^{eq}\right)+\varepsilon w_\alpha\theta+\frac{\varepsilon}{6e^2}e_{\alpha i}F_i.
\end{aligned}
\tag{5.20}
$$

According to the Chapman-Enskog expansion, f_α can be written in a series of ε,

$$
f_\alpha=f_\alpha^{(0)}+\varepsilon f_\alpha^{(1)}+\varepsilon^2 f_\alpha^{(2)}+O\left(\varepsilon^3\right).
\tag{5.21}
$$

The centered scheme is used for both source term θ and force term F_i as

$$
\theta=\theta\left(x+\frac{1}{2}e_\alpha\varepsilon,t+\frac{1}{2}\varepsilon\right)
\tag{5.22}
$$

and

$$
F_i=F_i\left(x+\frac{1}{2}e_\alpha\varepsilon,t+\frac{1}{2}\varepsilon\right).
\tag{5.23}
$$

which can also be written, via a Taylor expansion, as

$$
\theta\left(x+\frac{1}{2}e_\alpha\varepsilon,t+\frac{1}{2}\varepsilon\right)=\theta\left(x,t\right)+\frac{1}{2}\varepsilon\left(\frac{\partial}{\partial t}+e_{\alpha j}\frac{\partial}{\partial x_j}\right)\theta\left(x,t\right)+O\left(\varepsilon^2\right)
\tag{5.24}
$$

and

$$F_i\left(x+\frac{1}{2}e_\alpha\varepsilon,t+\frac{1}{2}\varepsilon\right)=F_i\left(x,t\right)+\frac{1}{2}\varepsilon\left(\frac{\partial}{\partial t}+e_{\alpha j}\frac{\partial}{\partial x_j}\right)F_i\left(x,t\right)+O\left(\varepsilon^2\right). \quad (5.25)$$

After substitution of Eq.(5.21), (5.24) and (5.25) into Eq.(5.20), the equation to the order of ε^0 is

$$f_\alpha^{(0)}=f_\alpha^{eq}, \quad (5.26)$$

to the order of ε is

$$\left(\frac{\partial}{\partial t}+e_{\alpha j}\frac{\partial}{\partial x_j}\right)f_\alpha^{(0)}=-\frac{f_\alpha^{(1)}}{\tau_t}+w_\alpha\theta+\frac{1}{6e^2}e_{\alpha i}F_i, \quad (5.27)$$

and to the order of ε^2 is

$$\begin{aligned}&\left(\frac{\partial}{\partial t}+e_{\alpha j}\frac{\partial}{\partial x_j}\right)f_\alpha^{(1)}+\frac{1}{2}\varepsilon^2\left(\frac{\partial}{\partial t}+e_{\alpha j}\frac{\partial}{\partial x_j}\right)^2 f_\alpha^{(0)}=-\frac{f_\alpha^{(2)}}{\tau_t}-\frac{\left(2\tau_t-1\right)}{2\tau_t r}e_{\alpha r}f_\alpha^{(1)}\\&+\frac{1}{2}\left(\frac{\partial}{\partial t}+e_{\alpha j}\frac{\partial}{\partial x_j}\right)\left(w_\alpha\theta\right)+\frac{1}{12e^2}\left(\frac{\partial}{\partial t}+e_{\alpha j}\frac{\partial}{\partial x_j}\right)\left(e_{\alpha i}F_i\right).\end{aligned} \quad (5.28)$$

By using Eq.(5.27), the above equation can be written as

$$\frac{\left(2\tau-1\right)}{2\tau}\left(\frac{\partial}{\partial t}+e_{\alpha j}\frac{\partial}{\partial x_j}\right)f_\alpha^{(1)}=-\frac{f_\alpha^{(2)}}{\tau}-\frac{\left(2\tau-1\right)}{2\tau}e_{\alpha r}f_\alpha^{(1)}. \quad (5.29)$$

From Eq. (5.27)+ $\varepsilon\times$ Eq.(5.29),

$$\begin{aligned}&\left(\frac{\partial}{\partial t}+e_{\alpha j}\frac{\partial}{\partial x_j}\right)f_\alpha^{(0)}+\frac{\left(2\tau_t-1\right)\varepsilon}{2\tau_t}\left(\frac{\partial}{\partial t}+e_{\alpha j}\frac{\partial}{\partial x_j}\right)f_\alpha^{(1)}\\&=-\frac{1}{\tau_t}\left(f_\alpha^{(1)}-\varepsilon f_\alpha^{(2)}\right)-\frac{\left(2\tau_t-1\right)\varepsilon}{2\tau_t}e_{\alpha r}f_\alpha^{(1)}+w_\alpha\theta+\frac{1}{6e^2}e_{\alpha i}F_i.\end{aligned} \quad (5.30)$$

The summation of the above equation over α provides

$$\frac{\partial}{\partial t}\sum_{\alpha} f_{\alpha}^{(0)} + \frac{\partial}{\partial x_j}\sum_{\alpha} e_{\alpha j} f_{\alpha}^{(0)} = \theta. \tag{5.31}$$

The use of equation (5.26) and substitution of equation (3.64) and (3.65) into the above equation result in the continuity equation (2.14). If the density variation is small enough and can be neglected.

Taking $\sum e_{ai}$ [equation (5.27) + $\varepsilon \times$ equation(5.29)] above α yields

$$\frac{\partial}{\partial t}\sum_{\alpha} e_{\alpha i} f_{\alpha}^{(0)} + \frac{\partial \Pi_{ij}^{(0)}}{\partial x_j} = \frac{\partial \Lambda_{ij}}{\partial x_j} + \frac{\Lambda_{ir}}{r} + F_i, \tag{5.32}$$

where Π_{ij}^{0} is the zero-order momentum flux tensor given by the following expressions:

$$\Pi_{ij}^{(0)} = \sum_{\alpha} e_{\alpha i} e_{\alpha j} f_{\alpha}^{(0)}, \tag{5.33}$$

$$\Lambda_{ij} = -\frac{\varepsilon}{2\tau_t}\left(2\tau_t - 1\right)\sum_{\alpha} e_{\alpha i} e_{\alpha j} f_{\alpha}^{(1)}, \tag{5.34}$$

and

$$\Lambda_{ij} = -\frac{\varepsilon}{2\tau_t}\left(2\tau_t - 1\right)\sum_{\alpha} e_{\alpha i} e_{\alpha r} f_{\alpha}^{(1)}. \tag{5.35}$$

By evaluating the terms in Eq. (5.33)with Eq.(3.54),

$$\Pi_{ij}^{(0)} = p\delta_{ij} + \rho u_i u_j, \tag{5.36}$$

Where $p = \rho e^2 / 3$ is the pressure, leading to a sound speed $C_s = e/\sqrt{3}$. Substitution of the above equation into equation (5.32) produces

$$\frac{\partial(\rho u_i)}{\partial t}+\frac{\partial(\rho u_i u_j)}{\partial x_j}=\frac{\partial p}{\partial x_i}+\frac{\partial \Lambda_{ij}}{\partial x_j}+\frac{\Lambda_{ir}}{r}+F_i. \tag{5.37}$$

By applying equation(5.27), equation (5.34) can be rewrite as

$$\Lambda_{ij}=\Pi_{ij}^{(1)}-\frac{\varepsilon}{2}(2\tau_t-1)\sum_{\alpha}e_{\alpha i}e_{\alpha r}w_\alpha\theta, \tag{5.38}$$

With the first-order momentum flux tensor Π_{ij}^{1} defined by

$$\Pi_{ij}^{(1)}=\frac{\varepsilon}{2}(2\tau-1)\sum_{\alpha}e_{\alpha i}e_{\alpha r}\left(\frac{\partial}{\partial t}+e_{\alpha k}\frac{\partial}{\partial x_k}\right)f_\alpha^{(0)}, \tag{5.39}$$

which can also be written using equation (5.33) as

$$\Pi_{ij}^{(1)}=\frac{\varepsilon}{2}(2\tau_t-1)\frac{\partial}{\partial t}\Pi_{ij}^{(0)}+\frac{\varepsilon}{2}(2\tau_t-1)\frac{\partial}{\partial x_k}\sum_{\alpha}e_{\alpha i}e_{\alpha r}e_{\alpha k}f_\alpha^{(0)}. \tag{5.40}$$

The second term in the above equation can be evaluated with equation (3.54) and (5.26) as

$$\frac{\partial}{\partial x_k}\sum_{\alpha}e_{\alpha i}e_{\alpha r}e_{\alpha k}f_\alpha^{(0)}=\frac{e^2}{3}\frac{\partial}{\partial x_k}\left(\rho u_i\delta_{jk}+\rho u_j\delta_{ki}+\rho u_k\delta_{ij}\right). \tag{5.41}$$

If assuming characteristic velocity U_c, length L_c and time t_c, the term $\partial/\partial t\Pi_{ij}^0$ is of the order of $\rho U_c^2/t_c$, and the term $\partial/\partial x_k\sum_a e_{ai}e_{aj}e_{ak}f_a^0$ is of the order of $\rho e^2U_c^2/L_c$, based on which we obtain that the ratio of the former to the latter terms has the order of

$$O\left(\frac{\partial/\partial t\Pi_{ij}^{(0)}}{\partial/\partial x_k\sum_\alpha e_{\alpha i}e_{\alpha r}e_{\alpha k}f_\alpha^{(0)}}\right)=O\left(\frac{\rho U_c^2/t_c}{\rho e^2U_c/L_c}\right)$$
$$=O\left(\frac{U_c}{e}\right)^2=O\left(\frac{U_c}{C_s}\right)^2=O(M)^2. \tag{5.42}$$

In which $M=U_c/C_s$ is the Mach number. It following that the first term in equation (5.40) is very small compared with the second term and can be neglected if $M\ll 1$, which is consistent with the lattice Boltzmann dynamics; hence equation(5.40), after equation(5.41) is substituted, becomes

$$\Pi_{ij}^{(1)}=\frac{e^2\varepsilon}{6}(2\tau_t-1)\frac{\partial}{\partial x_k}\left(\rho u_i\delta_{jk}+\rho u_j\delta_{ki}+\rho u_k\delta_{ij}\right), \tag{5.43}$$

or

$$\Pi_{ij}^{(1)}=\nu_t\left[\frac{\partial(\rho u_i)}{\partial x_j}+\frac{\partial(\rho u_j)}{\partial x_i}+\frac{\partial(\rho u_k)}{\partial x_k}\delta_{ij}\right]. \tag{5.44}$$

In which ν is the kinematic viscosity and defined by:

$$\nu_t=\frac{e^2\Delta t}{6}(2\tau_t-1). \tag{5.45}$$

The insertion of equation (5.44) into equation (5.38) and evaluation of the rest of the terms of the equation lead to

$$\Lambda_{ij}=\nu_t\left[\frac{\partial(\rho u_i)}{\partial x_j}+\frac{\partial(\rho u_j)}{\partial x_i}+\frac{\partial(\rho u_k)}{\partial x_k}\delta_{ij}\right]-\nu_t\theta\delta_{ij}. \tag{5.46}$$

After applying the continuity equation (2.14) and $\theta=-\frac{u_r}{r}$, to the above,

$$\Lambda_{ij} = \nu_t \left[\frac{\partial(\rho u_i)}{\partial x_j} + \frac{\partial(\rho u_j)}{\partial x_i} \right]. \tag{5.47}$$

Also,

$$\Lambda_{ir} = \nu_t \left[\frac{\partial(\rho u_i)}{\partial x_r} + \frac{\partial(\rho u_r)}{\partial x_i} \right]. \tag{5.48}$$

Combining Eqs.(5.6), (5.47)and (5.48) with Eq. (5.37)results in

$$\begin{aligned} \frac{\partial(\rho u_i)}{\partial t} + \frac{\partial(\rho u_i u_j)}{\partial x_j} = & -\frac{\partial p}{\partial x_i} + \nu_t \frac{\partial}{\partial x_j} \left[\frac{\partial(\rho u_i)}{\partial x_j} + \frac{\partial(\rho u_j)}{\partial x_i} \right] \\ & + \frac{\nu_t}{r} \left[\frac{\partial(\rho u_i)}{\partial r} + \frac{\partial(\rho u_r)}{\partial x_i} \right] - \frac{\rho u_i u_r}{r} - \frac{2\rho \nu_t u_i}{r^2} \delta_{ij}. \end{aligned} \tag{5.49}$$

If the density variation is assumed to be small enough, the above is just the momentum equation (2.44).

$$\frac{\partial u_j}{\partial x_j} = -\frac{u_r}{r}, \tag{5.50}$$

$$\frac{\partial u_i}{\partial t} + u_j \frac{\partial u_i}{\partial x_j} = -\frac{1}{\rho} \frac{\partial p}{\partial x_i} + \nu_m \frac{\partial^2 u_i}{\partial x_j^2} + \frac{\nu_m}{r} \frac{\partial u_i}{\partial r} - \frac{\nu_m u_i}{r^2} - \frac{\nu_m u_i}{r^2} \delta_{ir}. \tag{5.51}$$

Chapter 6: Initial and Boundary Conditions

6.1 Introduction

Proper choice of boundary conditions is important in solving the governing equation encountered numerical fluid dynamics. In this chapter, a number of different boundary conditions which widely used have been presented such as no-slip, slip and semi-slip. Many research shows that the boundary conditions have strongly influence on the accuracy and stability of the simulation results [138]. Some typical research can be found in [139-142]. Up to now, the research for the boundary conditions and initial conditions are still attracting many attentions in the LBM [143-145]. Succi [21] categorised two classes of boundary conditions in fluid dynamics: boundary conditions for simple cases and boundary conditions for complex cases. Brief descriptions of these types of boundaries are given as follows.

6.2 Solid Boundary Conditions

6.2.1 No-slip Boundary Condition

The standard bounce-back scheme is derived from the LGCA boundary conditions that are simple and widely used in implementing wall boundary conditions [146,147]. The post-collision distributions function in the lattice Boltzmann equation (3.28) coming from a solid node x_b to a fluid node x_f is not known during the streaming step. The bounce-back scheme is used to complete the unknown distribution function in the lattice Boltzmann equation [148]. In other words, the distribution function from the incoming particle $f_\alpha\ (x_f, t)$ towards the wall boundary is bounced back into the fluid (see Figure 6.1).

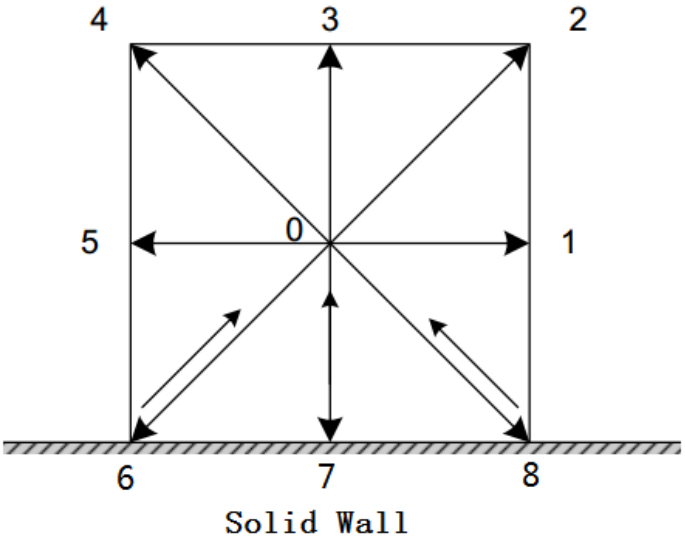

Figure 6.1 Layout of no-slip boundary conditions.

For a stationary wall, the bounce-back scheme is equivalent to setting the distribution function as follows [148]:

$$f_2 = f_6 \tag{6.1}$$

$$f_3 = f_7 \tag{6.2}$$

$$f_4 = f_8 \tag{6.3}$$

The zero momentum of the particle close to the solid wall is summed from the above equations leading to no-slip boundary conditions. The no-slip boundary condition is first-order accurate [144]. In order to achieve second-order accuracy, the wall needs to be placed in the middle of the lattice nodes, e.g. $x = 1/2$ with additional approximation of staircase boundary scheme treatment [139,150].

6.2.2 Slip Boundary Condition

When the boundary is smooth with negligible friction, a slip boundary condition should be applied, which has been depicted in Fig. 6.2. In such a case, the tangential momentum balance of the fluid flow on the wall should be achieved. There is no

momentum exchange with the wall along the tangential direction. The unknown distribution functions f_2, f_3 and f_4 can be calculated:

$$f_2 = f_8 \tag{6.4}$$

$$f_3 = f_7 \tag{6.5}$$

$$f_4 = f_6 \tag{6.6}$$

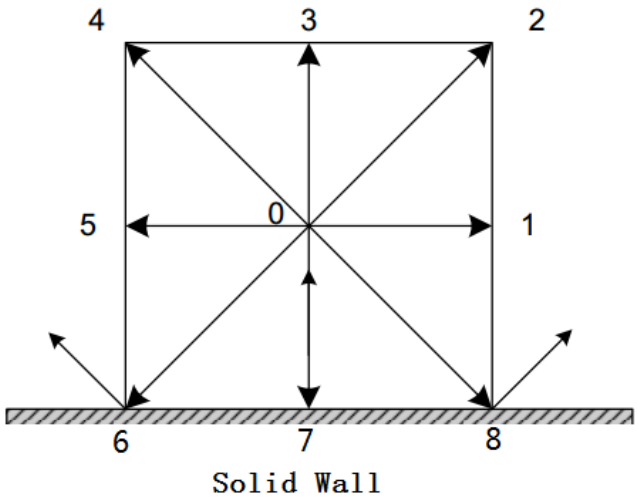

Figure 6.2 Slip boundary condition layout.

6.2.3 Semi-slip Boundary Condition

When fluid flows over a stationary surface, the fluid touching the surface is brought to rest by the shear stress [18,151]. Some fluid particles bounce back into the main stream and others move along the surface duet to the friction force. There is no motion normal to the surface; only a thin film of fluid moves tangentially along it, for which a combination of no-slip and slip boundary conditions would provide the best results.

Zhou [152] suggested that it is necessary to consider the effect of wall shear stress in order to achieve a semi-slip boundary condition. The wall shear stress vector τ_f due to wall friction can be expressed,

$$\tau_f = -\rho\nu \frac{\partial V_\tau}{\partial n^*} = -\rho C_f |V_\tau| V_\tau, \tag{6.7}$$

where V_τ is the velocity vector parallel to the wall; n^* is the outward coordinate normal to the wall; and C_f is the friction factor at the wall. The wall friction factor τ_f may be estimated with the Manning roughness n_f by:

$$C_f = \frac{g n_f^2}{r^{1/3}}, \tag{6.8}$$

The velocity vector normal to the wall tends to be zero if the slip boundary condition is applied at the boundary node. Thus,

$$V_\tau = V. \tag{6.9}$$

Substitution of equation (3.6) into (3.4) gives the tensor form of wall shear stress:

$$\tau_{fi} = -\rho C_f u_i \sqrt{u_j u_j}. \tag{6.10}$$

Hence, a semi-slip boundary condition can be used at the boundary node by adding the wall shear stress τ_{fi} into the force term F_i in the lattice Boltzmann equation (3.10) together with the slip boundary condition.

6.3 Inflow and Outflow Conditions

Appropriate inlet and outlet boundary conditions are important to obtain realistic simulation results, which work as constraints to ensure consistency with the

surrounding flow conditions. In fact, different flow variables (such as velocity and pressure) at the boundary have to reflect the correct situation.

In traditional numerical methods, it is common to assign a given velocity profile at the inlet while imposing a given fluid velocity at the outlet [18]. In LBM, the zero gradients technique for these physical variables in the computational analysis has been proven to give satisfactory results [14]. For example, after streaming, the unknown f_1 , f_2 and f_8 are simply calculated by:

$$f_\alpha(1,j) = f_\alpha(2,j), \qquad \alpha = 1,2,8. \tag{6.11}$$

Similarly, for the out flow, the unknown distribution functions f_4 , f_5 and f_6 have the following relations:

$$f_\alpha(N_x,j) = f_\alpha(N_x-1,j), \qquad \alpha = 4,5,6. \tag{6.12}$$

where N_x is the total lattice number in x direction.

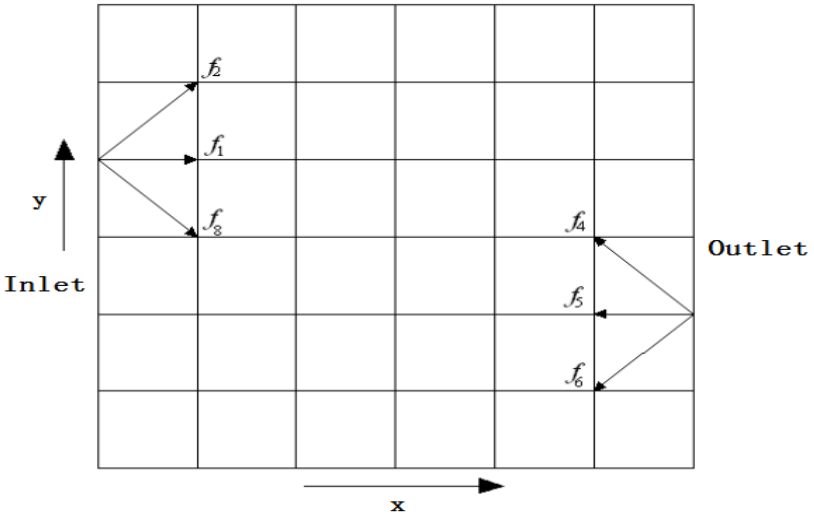

Figure 6.3 Sketch for inflow and outflow boundaries.

For the axisymmetric flows with swirl, all of the distribution functions can be set to their respective local equilibrium distribution functions, $f_\alpha = f_\alpha^{eq}$ and $\overline{f}_\alpha = \overline{f}_\alpha^{eq}$ which is proposed by Zhou [49] and demonstrated to produce accurate solutions to rotational axisymmetric flows. Although a real individual distribution function may be different from the local equilibrium distribution function, this can provide accurate solutions to the problem as the following chapters show. It should be noted that other schemes like

the non-equilibrium extrapolation approach by Guo *et al*. [153] may be applied for accurate solutions to flows with significant non-equilibrium effect.

6.4 Periodic Boundary Condition

A periodic boundary condition may be useful in some specific cases. For example, the blood flows in the human body and a flow region contains the tidal flow. It has good stability when the computational domain becomes closed by connecting the inflow and outflow boundaries in the computation. According to these flows features, a periodic boundary condition can be achieved by specifying the unknown f_1 , f_2 and f_8 at the inflow boundary after streaming equal to the counterparts at the outflow boundary (see Fig. 6.4),

$$f_\alpha(1, j) = f_\alpha(L_x, j), \qquad \alpha = 1, 2, 8. \tag{6.13}$$

Similarly, the unknown f_4 , f_5 and f_6 at the outflow boundary are equal to the counterparts at the inflow boundary,

$$f_\alpha(L_x, j) = f_\alpha(1, j), \qquad \alpha = 4, 5, 6. \tag{6.14}$$

where L_x is the final node in the *x* direction within the computational domain. Also, a periodic boundary condition in the *y* direction can be achieved.

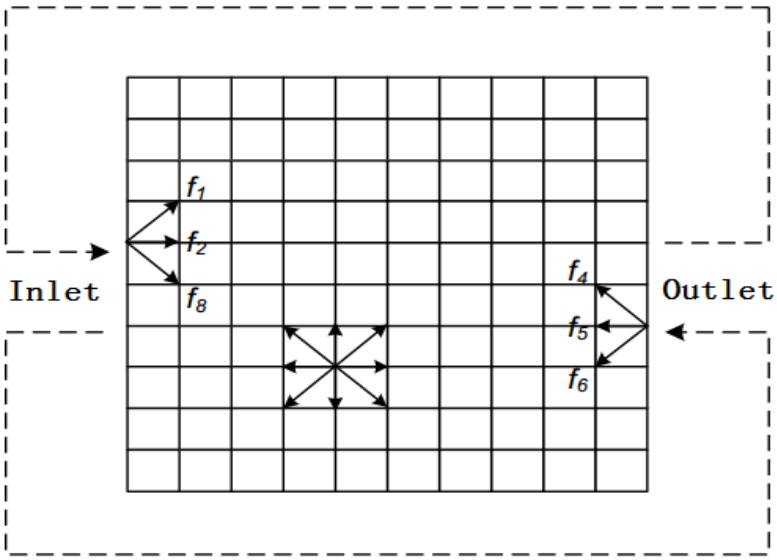

Figure 6.4 Sketch for the Periodic Boundary Condition

6.5 Initial Condition

Initial condition is the flow at the start time (when t=0s). Before calculation, the initial condition for distribution function needs to be given. Generally, there are two ways to specify the initial condition in the lattice Boltzmann method [14]. One is to specify a random value between 0 and 1 for the distribution function. The other is to define a flow field with fluid velocity and density firstly, then calculate the local equilibrium distribution function f_α^{eq} and use it as an initial condition for f_α. Generally speaking, it is easier to define a macroscopic value than a microscopic. Hence, the second method is preferred in practical computations, which is used in the present models. It should be notice that there is no difference between results calculated with these two initial conditions for a steady flow problem.

6.6 Solution Procedure

The solution procedures for the AxLAB® and AxLAB® with turbulence are very simple. It involves only explicit calculations and consists of the following steps:

For AxLAB® or AxLAB® with turbulence, the procedure is

1. Assume the initial fluid density ρ and velocity u , v ,

2. Compute f_α^{eq} from Eq.(3.54),

3. Calculate f_α from the lattice Boltzmann equation (3.56) or from the Eq. (4.15) for turbulent flows together with the total relaxation time τ_t calculated from Eq. (4.17).

4. Renew the fluid density and the velocity by Eqs. (3.64) and (3.65),

5. Return to step 2 and repeat the above procedure until a solution is obtained.

The calculation procedure can also illustrate by a flow chart below:

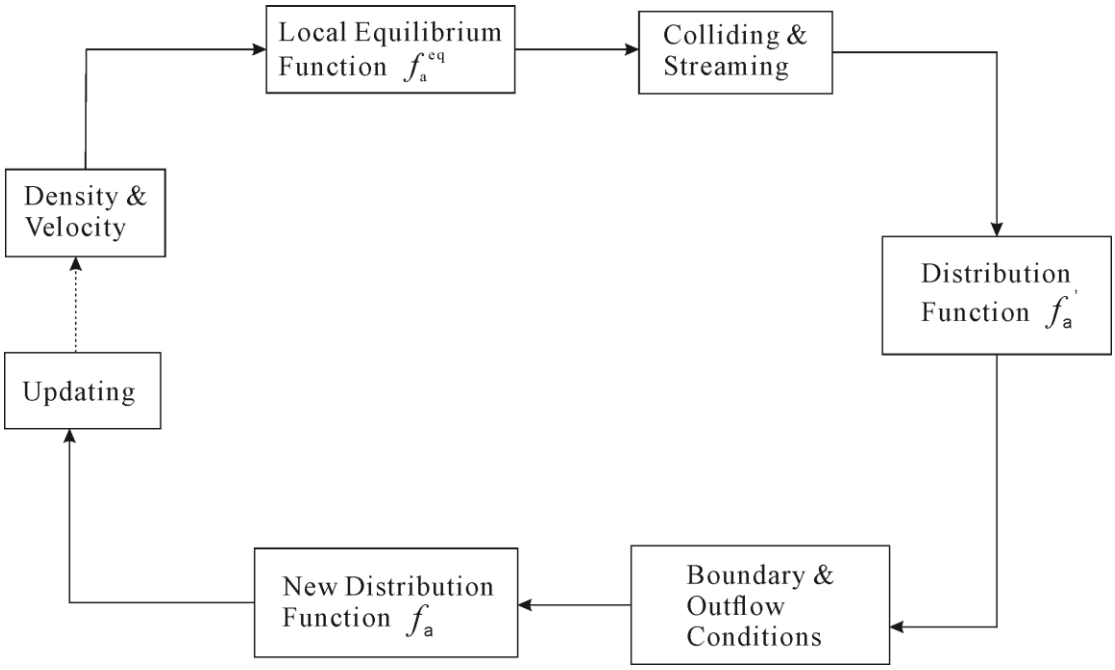

Figure 6.5 Flow chart to demonstrate the LBM calculation procedure.

Chapter 7: Applications to Laminar Flows

7.1 Steady Flow through a Straight Pipe

Flow through a normal pipe is a basic case for axisymmetric flow simulation. This kind of flow is an axisymmetric steady, laminar flow of a viscous fluid through a pipe driven by a parabolic velocity profile at the inlet. A pipe was selected with the diameter of D=40m, in the numerical calculation, the velocity u_x in the axial direction is specified at the inflow boundary,

$$u_x = U_0\left[1-\left(\frac{r}{R}\right)^2\right] \tag{7.1}$$

with $U_0 = 0.01\, m/s$ and the zero gradient is applied at the outlet boundary. 81×41 lattices are used with flow density of $\rho = 3\ kg/m^3$. The Reynolds number is

$$\mathrm{Re} = 4.1 \qquad (\mathrm{Re} = \frac{U_0 D}{\nu}) \tag{7.2}$$

After steady solution reached, the result below can be obtained.

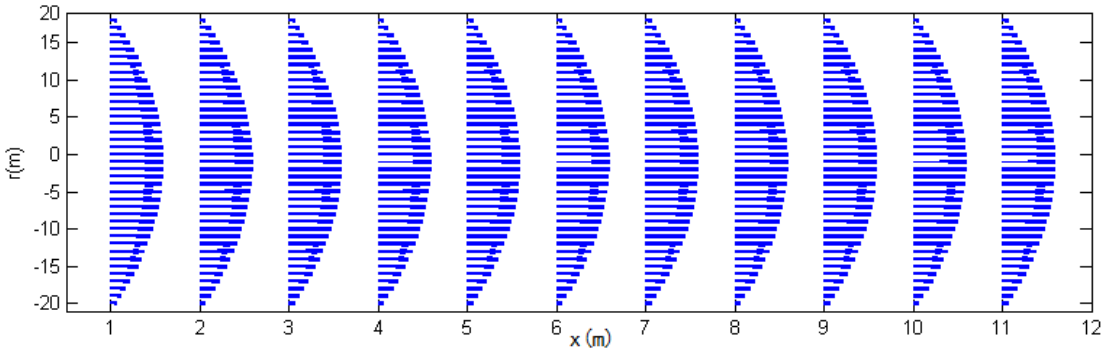

Figure 7.1Velocity vectors for steady flow through a straight pipe by AxLAB®.

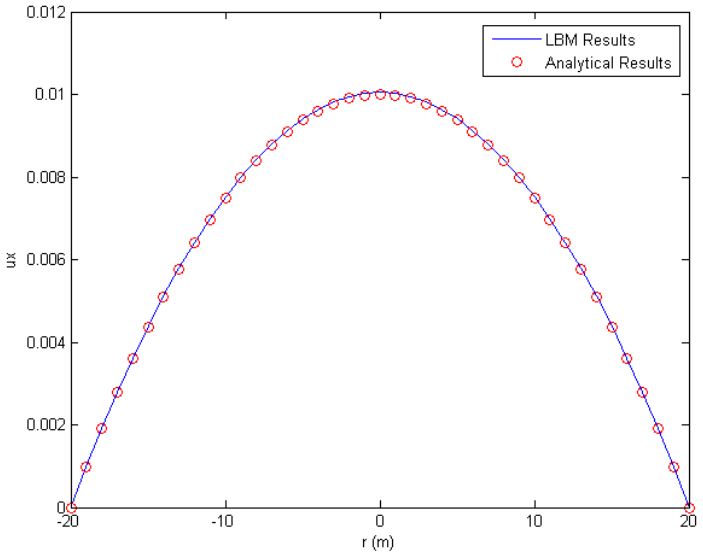

Figure 7.2 Velocity U_x distribution across cross section in pipe flow

The velocity profiles and vectors for u_x are shown in Fig. 7.1 and Fig. 7.2 respectively, which are correct with the analytical results [154] and can be used for further simulations.

7.2 Flows through a Concentric Annulus

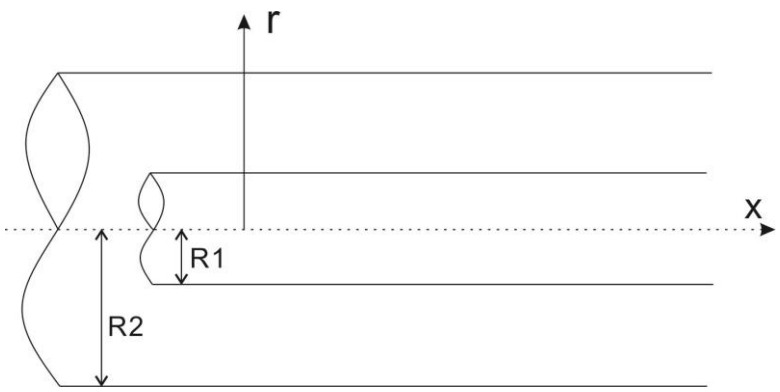

Figure 7.3 Flow through a concentric annulus.

A steady axial laminar flow in the annular space between two concentric cylinders is considered. It is driven by a constant pressure gradient schematic (see Fig. 7.3). There are no-slip at the inner wall $r = R_1$ and outer wall $r = R_2$. The radius ratio of outer cylinder to inner cylinder is defined as *k*. So when the $k \to \infty$, the flow recovers the

normal pipe flow which has shown in section 7.1. The treatment for this simulation is same as normal pipe flow.

The analytical solution for the velocity profile is [154]

$$u_x = \frac{1}{4\upsilon p}\frac{dp}{dx}\left[r^2 - R_2^2 - \frac{R_2^2 - R_1^2}{\ln\left(R_2 / R_1\right)} \ln\frac{r}{R_2} \right], \tag{7.3}$$

and the average velocity is

$$\bar{u} = -\frac{1}{8\upsilon p}\frac{dp}{dx}\left[R_2^2 - R_1^2 - \frac{R_2^2 - R_1^2}{\ln\left(R_2 / R_1\right)} \right]. \tag{7.4}$$

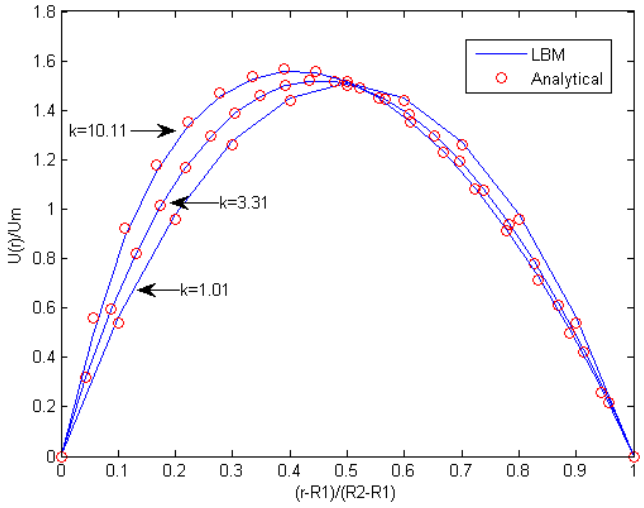

Figure 7.4 Velocity profile for flow through concentric annulus with radius ratio $k = 1.01,\ 3.31$ and 10.11.

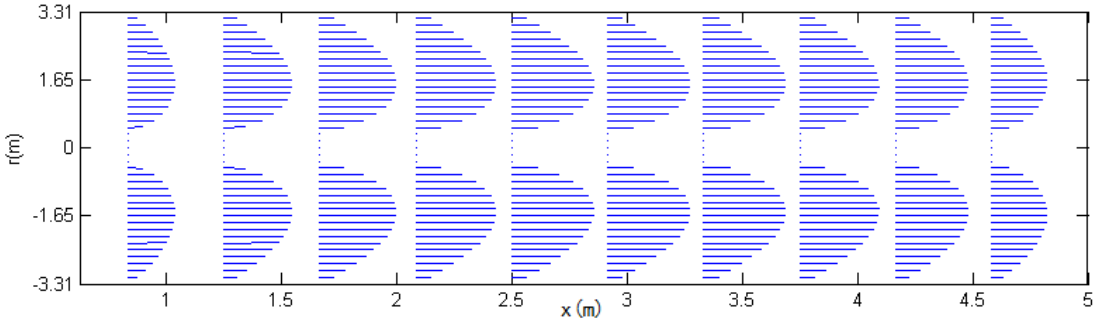

Figure 7.5 Velocity vectors when $k = 3.31$ by AxLAB®.

Fig 7.4 shows the normalized velocity profiles as U_r / U_m for flow through concentric annulus with k = 1.01, 3.31 and 10.11.Then numerical results agree well with the analytical solutions. The figure also shows that the velocity profile leans toward the inner cylinder as the radius ratio k increases, which is consistent with [154]. The flow velocity vectors are plotted in Fig 7.5, it is easy to see that the velocity leans to the centre line of the pipe.

7.3 Steady Flow through a Constricted Pipe

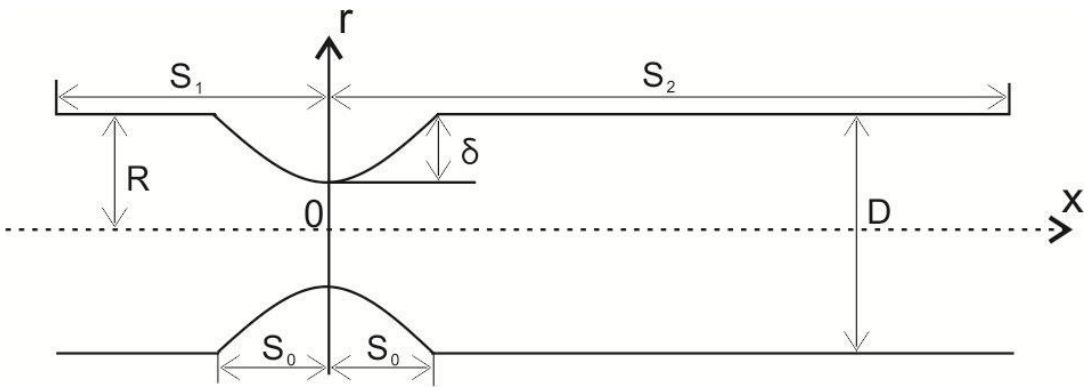

Figure 7.6 Geometry of constricted pipe.

The flow in constricted pipes has been of great interest to biodynamicists. Although the actual geometry of astenotic artery maybe complex and varied, it is frequently simplified as a symmetric constriction in a cylindrical tube. Several researchers have studied steady flow through an axisymmetric tube with constriction. Smith studied steady flow through an axisymmetric stenosis using an analytical method [155]. Huang *et al*. [156] investigated steady flow through tubes with constrictions using LBM with D3Q19 model. The flow was studied by using axisymmetric lattice Boltzmann method due to its simple and efficient feature.

In this case, the geometry of the constriction is described by a cosine function curve. The geometry of the constricted pipe is shown in Fig 7.6 and the radius of the stenosis is described by the following function:

$$r(x) = R - \frac{\delta}{2}\left(1 + \cos\frac{\pi x}{S_0}\right), \qquad (-S_0 < x < S_0), \tag{7.5}$$

where R is the radius of the nonstenosis is $2S_0$, and $S_0 = D$. In this study, three cases of stenosis radial height were computed, $\delta = R/2,\ R/3,\ R/4$. As schematic in Fig 7.6, $S_1 = 3D$, $S_2 = 8D$ was set to make sure that the flow is fully developed at the outlet.

In this simulation, a fully developed parabolic velocity profile is imposed at the inlet boundary and the zero pressure gradients are used at the outlet boundary. The centre value of the inlet parabolic velocity keeps at $u_c = 0.01$. The employed lattice number is 441×41 and the Reynolds number $Re = 4.1$. The wall boundary conditions deal with by using the bounce-back scheme. The inlet velocity boundary is applied with Zou and He velocity boundary treatment [157] and the outlet pressure is specified from the next inner nodes. Fig 7.7 shows the velocity vectors of this simulation. It can be noticed that the velocity increased rapidly at the constricted location. In order to test the convergence of the grid number, one more lattice mesh (grid 2: 881×81) was also proposed in this case. In Figs 7.8 and 7.9, the velocity profiles are plotted on both mesh when $\delta = R/3$. From the figures, only small differences can be seen. Defining the relative error between two meshes as $E_r = (u_1 - u_2)/u_1$, in which u_1 and u_2 are the maximum velocity of axial velocity for the standard mesh and the fine mesh (grid 2), respectively, the relative error is found to be 0.897%. Therefore the 441×41 mesh is deemed adequate for the present simulations.

The normalized axial and radial velocity profiles at $x = 0$ are shown in Figs 7.8 and 7.9, respectively, for three values of the stenosis radial height. It can be seen that the axial velocity increases and exhibits sharper as the stenosis radial height increases. In Fig 7.8, the obvious reverse flow is observed and the absolute radial velocity also increases as the stenosis radial height increases. The results show that the stenosis radial height has significant effect on the velocity and thus the wall shear stress distribution.

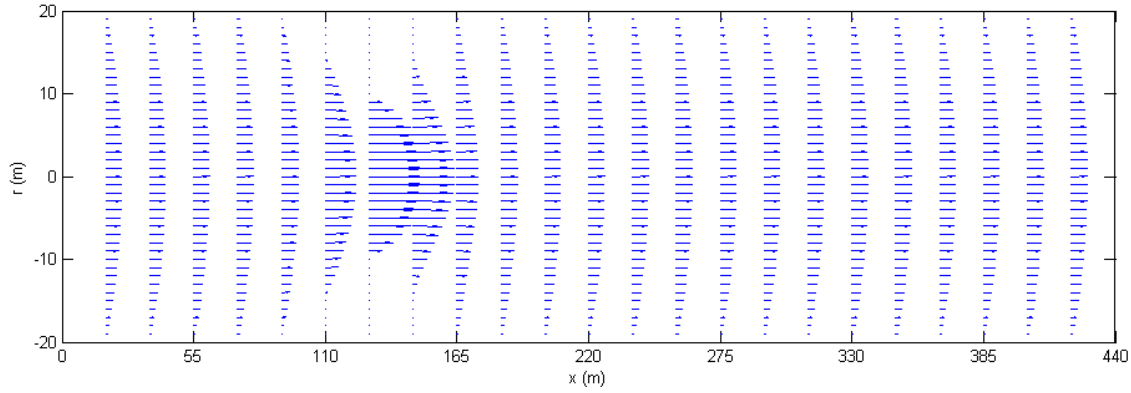

Figure 7.7 Velocity vectors for steady flow through a constricted pipe when $\delta = R/2$.

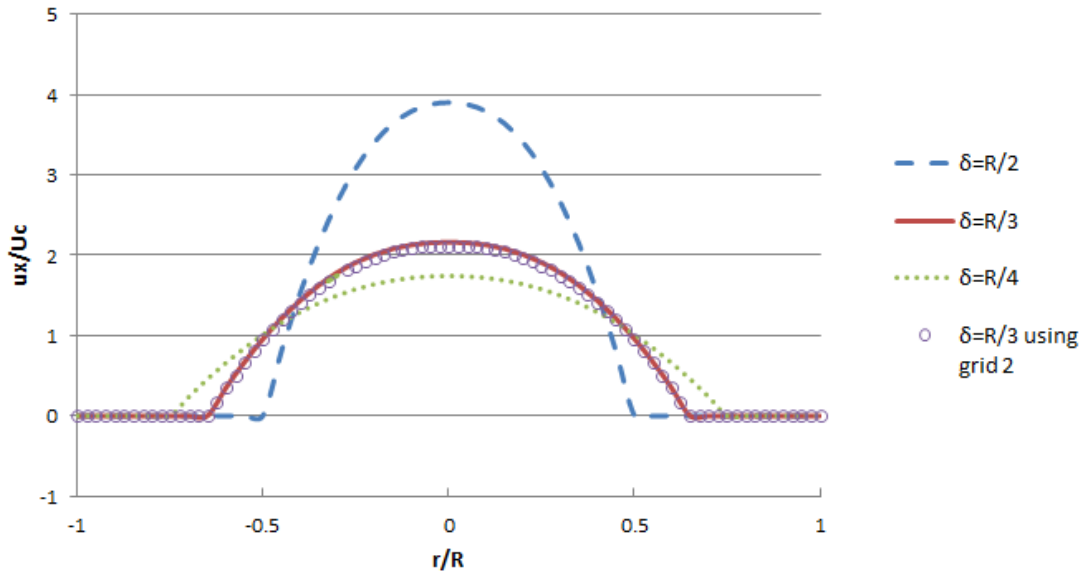

Figure 7.8 Axial velocity profiles in constricted pipe for three different constriction radial heights.

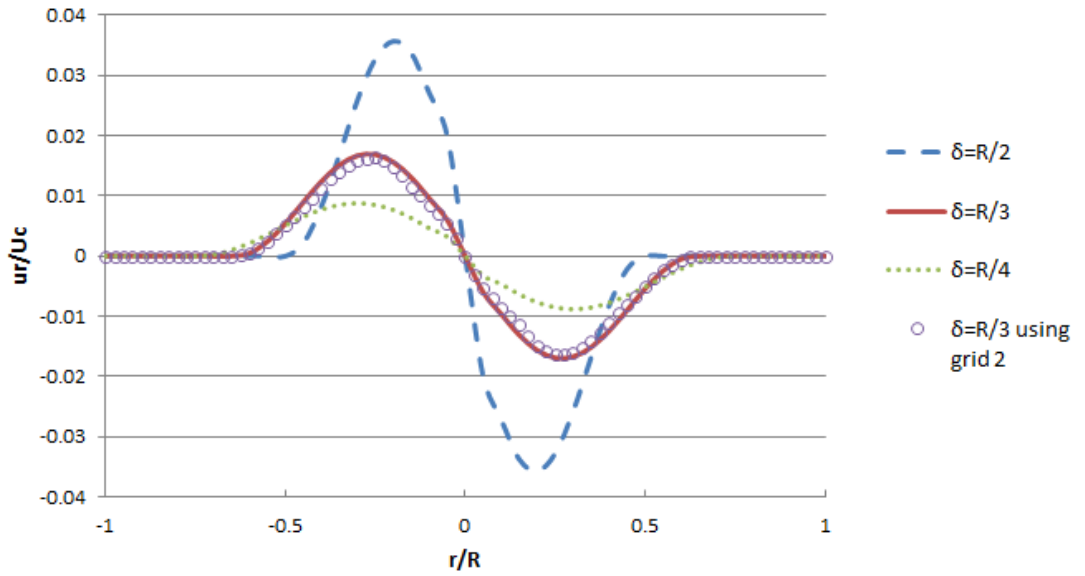

Figure 7.9 Radial velocity profiles in constricted pipe for different constriction radial heights.

7.4 Steady Flow through an Expanded Pipe

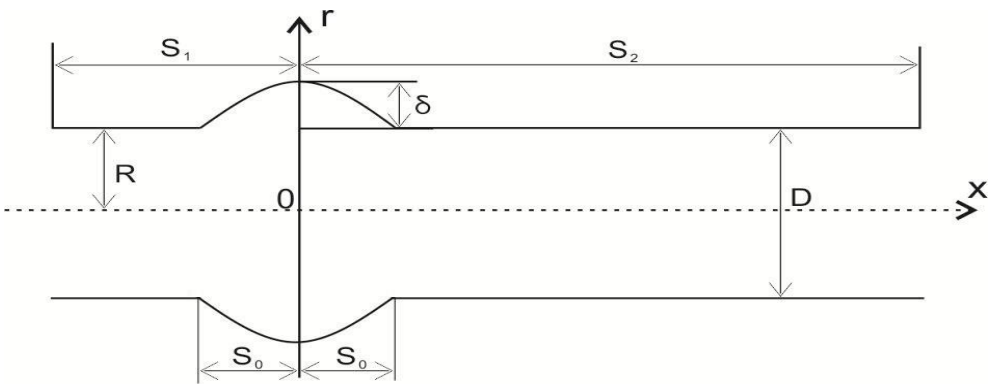

Figure 7.10 Geometry of expanded pipe.

The steady flow through a pipe with local expansion of cosine function shape was also simulated in this study. The geometry of the expansion is shown in Fig 7.10. Radius of the expansion is described by the following function:

$$r(x) = R + \frac{\delta}{2}\left(1 + \cos\frac{\pi x}{S_0}\right), \qquad (-S_0 < x < S_0), \tag{7.6}$$

where R is the radius of the non-expanded part of the pipe, δ is the radial height of the expansion, the axial length of the expansion is $2S_0$ with $S_0 = D$. In this study, the expansion height was $\delta = R/2$. As schematic in Fig. 7.10, it was set $S_1 = 3D$ and $S_2 = 8D$ to make sure the flow fully developed at the outlet.

In this simulation, a fully developed parabolic velocity profile is also imposed at the inlet boundary and the zero pressure gradients are used at the outlet boundary. The centre value of the inlet parabolic velocity is $u_c = 0.01$ and the Reynolds number $Re = 4.1$ ($Re = u_c D/\nu$). The boundary conditions are treated with the same method as the flow through a constricted pipe. Fig 7.11 shows the velocity vectors of this simulation. It illustrated that the velocity decreased at the expended location and then increased during the downstream flow. It can be seen that the axial velocity profile at $x = 0$ shown in Fig 7.12 increases as the expansion height increases, while the radial velocity at $x = 0$ shown in Fig 7.13 increases as the distance increases. This validates that the short distance after the pipe expansion significantly influences the velocity of the flow, hence leading to a great effect on the wall stress tensor in the flow. For human carotid with local expansion, these changes of velocity and thus the wall shear stress caused by expansion will in fluency the structure and the function of the vessel significantly. In addition, the convergence test ($\delta = R/4$) was also proposed in this study, three different time steps were selected for this test, $0.5\Delta t$, Δt and $2\Delta t$. From Fig 7.14, it can be seen that the results using $0.5\Delta t$ and Δt were almost same. But for $2\Delta t$, the result was a little far beyond the former two, which caused errors for this study. So, Δt was the proper time step for this simulation.

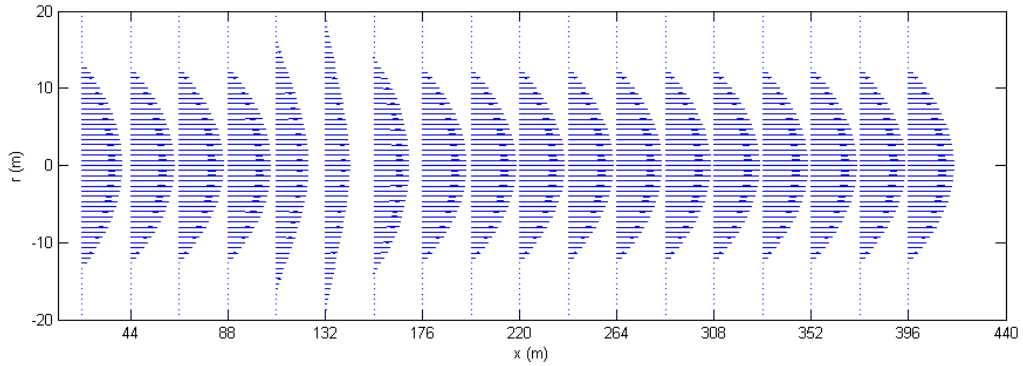

Figure 7.11 Velocity vectors when $\delta = R/2$.

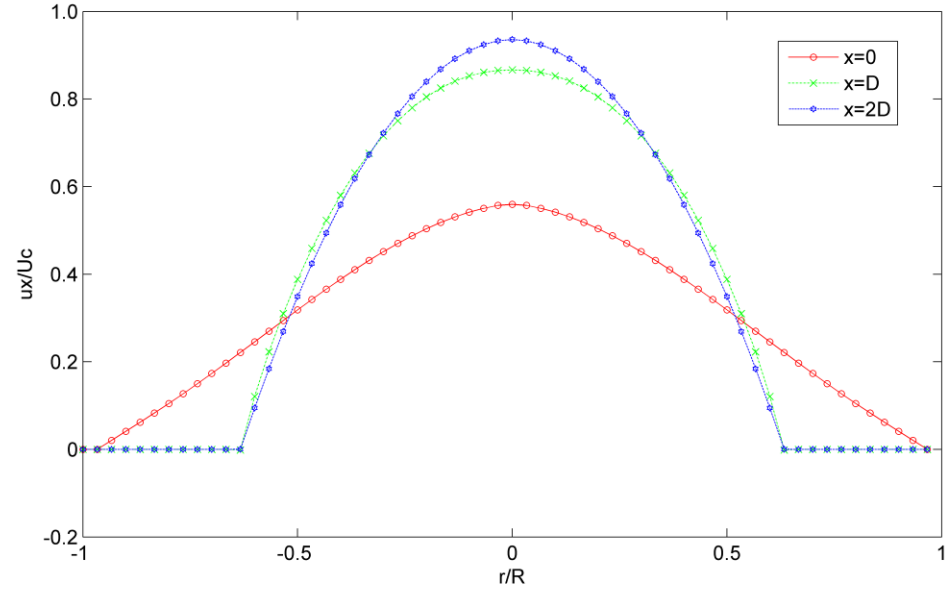

Figure 7.12 Axial velocity profiles in expanded pipe at different distances when $\delta = R/2$.

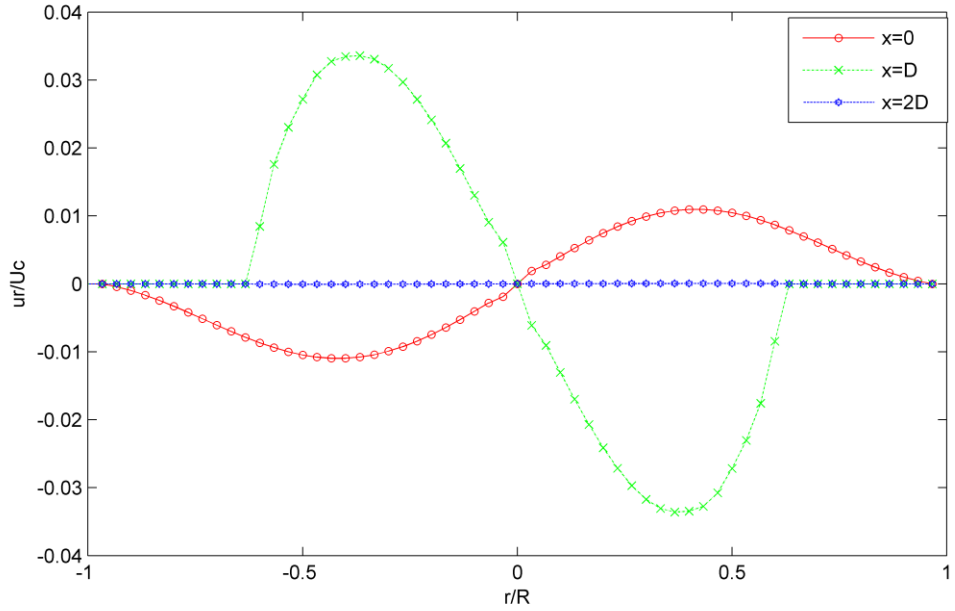

Figure 7.13 Radial velocity profiles in expanded pipe at different distances when $\delta = R/2$.

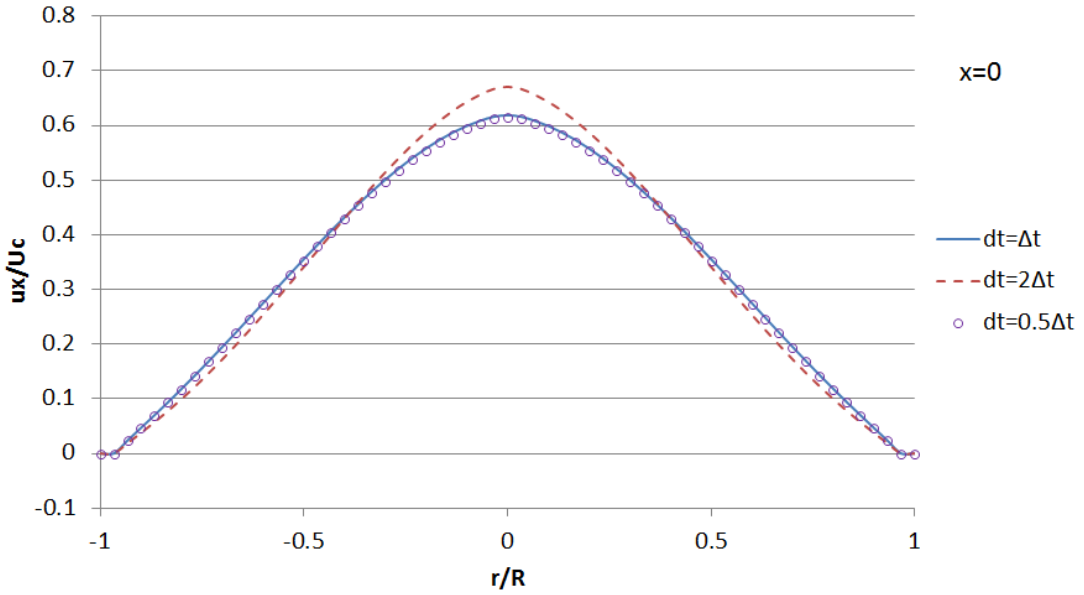

Figure 7.14 Axial velocity profiles in expanded pipe at $x = 0$, compared with two time steps $0.5\Delta t$ and $2\Delta t$, when $\delta = R/4$.

7.5 Unsteady Tube Flow (3D Womersley Flow)

The 3D Womersley flow, or a pulsatile flow, is an unsteady axisymmetric flow in a straight pipe. It is driven by a periodic pressure gradient at the inlet of the pipe and pressure gradient is normally given as

$$\frac{dp}{dx} = p_0 \cos \omega t \tag{7.7}$$

where p_0 is the maximum amplitude of the pressure variation and $\omega = 2\pi / T$ is the angular frequency, in which T is the period. The Reynolds number is defined as $Re = U_c D / v$, U_c is the characteristic velocity given by

$$U_c = \frac{p_0 \alpha^2}{4w\rho} = \frac{p_0 R^2}{4\rho v} \tag{7.8}$$

In which $\alpha = R\sqrt{\omega / \nu}$ is the womersley number, when $\alpha \to 0$, the flow is steady flow. Where *R* is the pipe radius and *D* is the diameter. The analytical solution for the velocity of axisymmetric pulsatile pipe flow in the axial direction is

$$u_x(r,t) = \mathrm{R}_e\left\{\frac{p_0}{iwp}\left[1-\frac{J_0(r\phi/R)}{J_0(\phi)}\right]e^{iwt}\right\}, \tag{7.9}$$

where J_0 is the zeroth order Bessel function of the first type, i is the imaginary unit, $\phi = (-\alpha + i\alpha)/\sqrt{2}$, and $\mathrm{R_e}$ denotes the real part of a complex number. The implementation of the periodic pressure gradient can be achieved by applying an equivalent periodic body force to the flow [68] or specifying periodic pressure at the inlet and fixing the outlet pressure [104], an additional body force is added to the existing force term F_i ,

$$F_i = -\frac{\rho u_i u_r}{r} - \frac{2\rho\nu u_i}{r^2}\delta_{ir} + p_0\cos(wt)\delta_{ix} \tag{7.10}$$

In the computation, $\rho = 3,\ p_0 = 0.001,\ D = 40,\ T = 1200,\ \alpha = 8,$ and $U_c = 1,$ which gives $Re = 1200$. Also $\tau = 0.6$, 80×40 lattice with $\Delta x = 1$ are used in the simulation. The periodic boundary conditions are applied to inflow and outflow boundaries; the standard bounce-back scheme is applied to no-slip boundary conditions along the pipe walls. The numerical solutions at different times are obtained after an initial running time of 10*T*. The numerical results along diameter were compared to the analytical solutions of Eq.(7.9) in Figs.7.15 and 7.16. The velocity is normalized by U_c. The radius axis is nondimensionalized by dividing by the radius of the tube as shown in Figs.7.15 and 7.16. It also can be noticed when oscillatory pressure gradient changes very fast and it is impossible for velocity field to reach the fully developed velocity profile with maximum value U_c . From this case, the character velocity U_c=1.0, but the U_{max} observed in whole oscillatory period is only about 0.07.

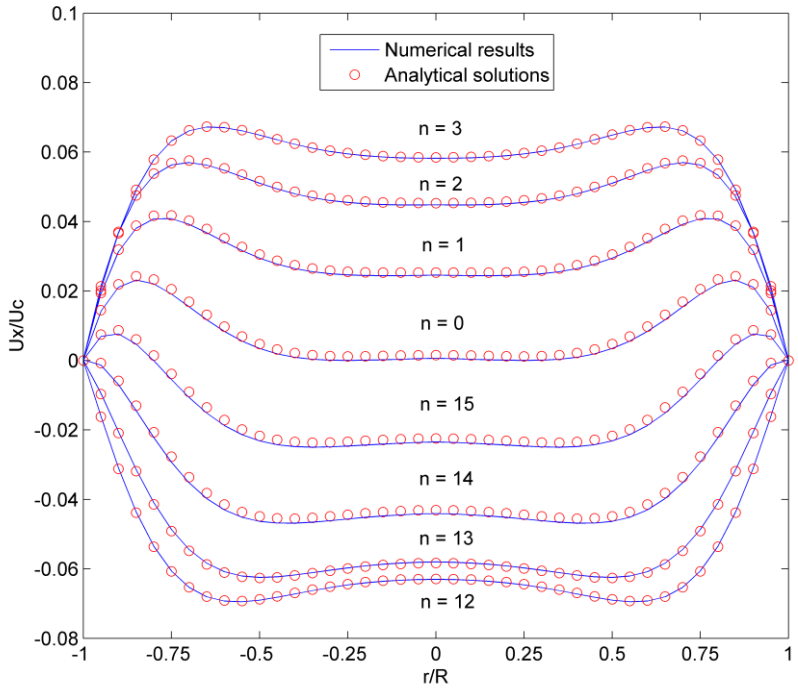

Figure 7.15 Comparisons when u_x is increasing at different times $t = nT/16,$ with n=0, 1, 2, 3, 12, 13, 14, 15.

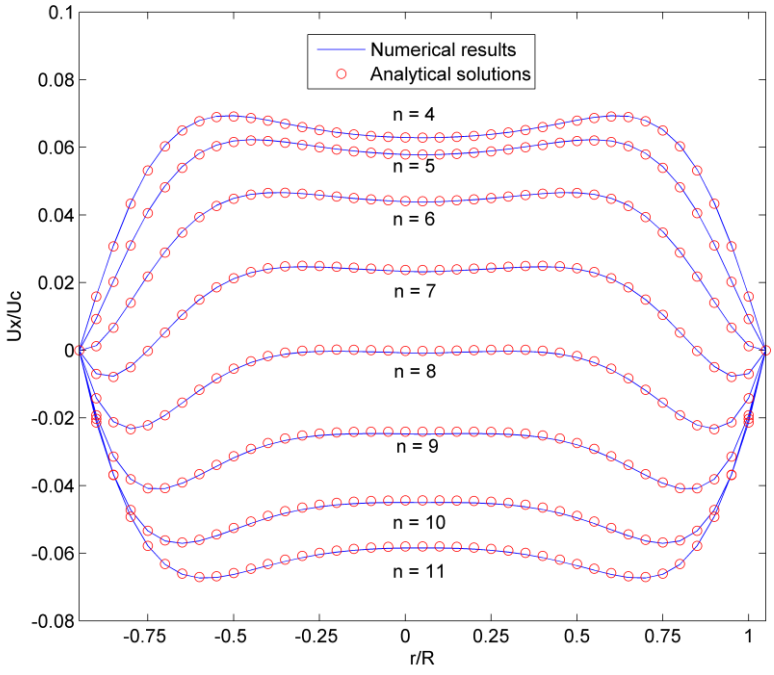

Figure 7.16 Comparisons when u_x is decreasing at different times, $t = nT/16,$ with n=4, 5, 6, 7, 8, 9, 10, 11.

7.6 Cylindrical Cavity Flow

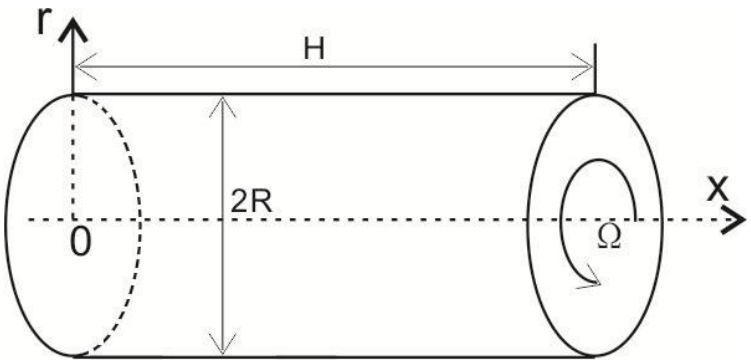

Figure 7.17 Definition sketch for cylindrical cavity flow.

Steady cylindrical cavity flows have been investigated both experimentally and numerically in last few decades [48,158-160]. The flow problem is sketched in Fig. 7.17 and is known to have different complex structures depending on the combinations of the aspect ratio $\Gamma = H / R$ and the Reynolds number Re. With different combinations of these two parameters, distinct breakdown bubbles may occur. The bottom of the cavity is closed and kept stationary, while the top lid rotates around the cylindrical axis with a constant angular velocity Ω. Four cases with parameters of (Γ, Re), namely a. (1.5, 990), b. (1.5, 1290), c. (2.5, 1010) and d. (2.5, 1290), have been used to validate the 3D lattice Boltzmann method by Bhaumik and Lakshmisha [160] and the axisymmetric lattice Boltzmann method by Guo *et al*. [75]. Li *et al*. also used the first two cases for the validation of their improved axisymmetric lattice Boltzmann scheme [158]. Consequently, these four cases are applied to test the AxLAB® stability and accuracy.

These cases has also been investigated in the experiment, the stream lines for the steady solution are plotted in Fig. 7.18-7.21 and clearly show that breakdown vortices are well developed. The streamlines of the swirling flow are shown for the four cases considered. It is seen that in the cases of (a) and (c), no breakdown bubbles are seen. In case (b), however, a single bubble appears. Moreover, in case (d), a couple of bubbles appear which was not presented by the report of Guo *et al*. [75]. All the flow patterns are again in agreement with that observed in the experimental measurements [160].

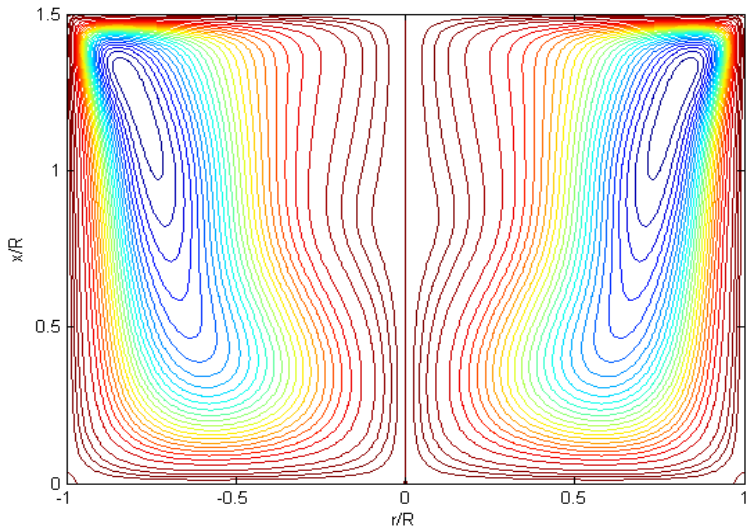

Figure 7.18 Stream lines for Case (a) with Γ = 1.5 and Re = 990.

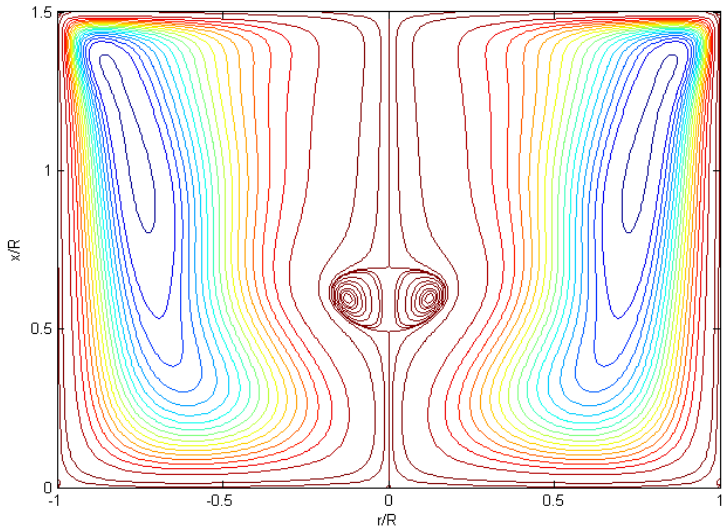

Figure 7.19 Stream lines for Case (b) with Γ = 1.5 and Re = 1290.

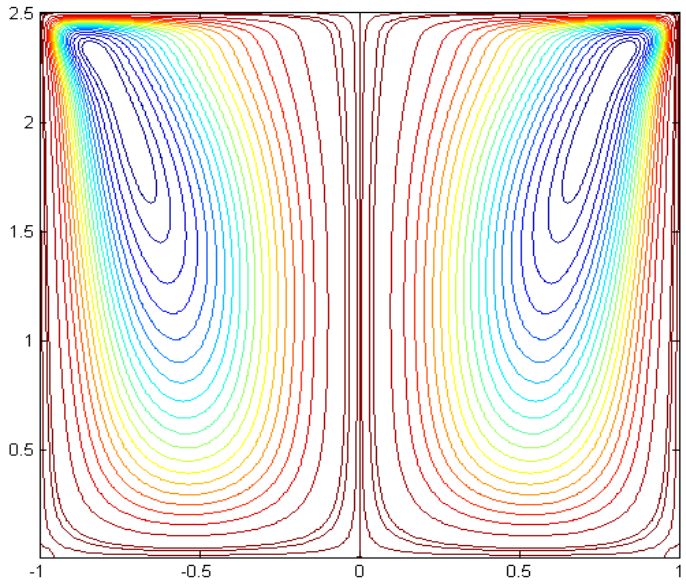

Figure 7.20 Stream lines for Case (c) with A = 2.5 and Re = 990.

In the simulations, R=1, $\rho = 1$ and $\tau = 0.55$. The boundary conditions are

$$\begin{cases} u_x = u_r = u_\phi = 0, & x = 0, \\ u_x = u_r = u_\phi = 0, & r = \pm R, \\ u_x = u_r = 0, u_\phi = r\Omega, & x = H. \end{cases} \tag{7.11}$$

which are implemented in the proposed model by setting all of the distribution functions to their respective local equilibrium distribution functions, $f_a = f_a^{eq}$ and $\overline{f_a} = \overline{f_a^{eq}}$, at the boundaries. Although a real individual distribution function may be different from the local equilibrium distribution function, this can provide accurate solutions to the problem as the following results show. It should be noted that other schemes like the nonequilibrium extrapolation approach by Guo *et al*. [42] may be applied for accurate solutions to flows with significant nonequilibrium effect.

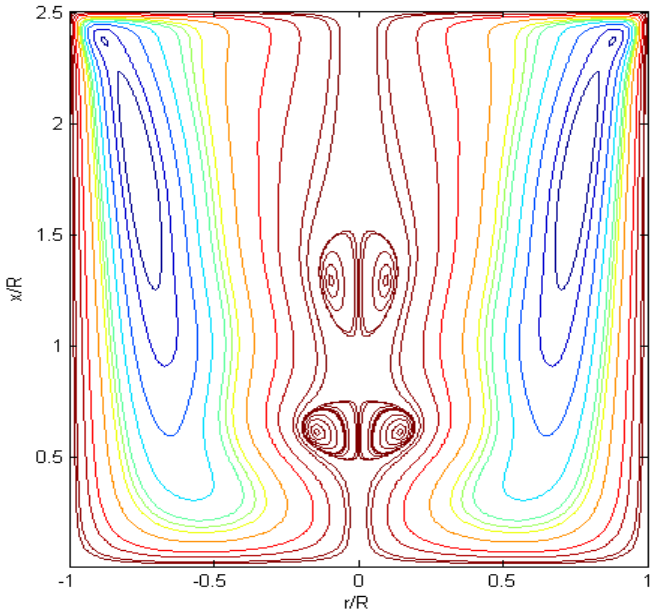

Figure 7.21 Stream lines for Case (d) with A = 2.5 and Re = 1290.

7.7 Different Forced Axisymmetric Laminar Cold-Flow Jets

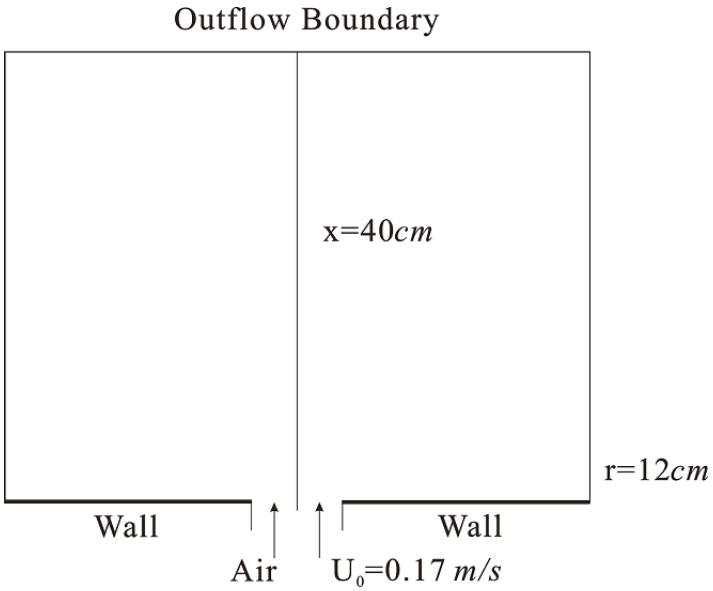

Figure 7.22 Wall jet forced flow.

The next case considered is the forced cold-flow jets, of which periodically forced jets present many opportunities for jet mixing for a variety of applications. In practical engineering, the ability to increase the mixing rate for laminar flows is important in

the development of mesoscale reactors of various types. In this section, simulations are performed to study the effect of high-amplitude forcing on laminar jets. Different amplitudes and frequencies of the forcing function are investigated to show the vortex creation and the subsequent flow evolution downstream of the jet. This case is illustrated schematically in Fig. 7.22, which involves a wall jet; the computational domain is 12 cm in the radial direction and 40 cm in the axial direction. A uniform grid with 400×120 lattices was used. The same test is also used by Barve *et al*. [161] with a finite volume method. The diameter of the wall jet was 1 cm and the Reynolds number, $\mathrm{Re}=U_0D/\nu$, was set to 100, where U_0 is the jet exit axial velocity which is 0.17*m/s*, *D* is the jet diameter. The forcing case involved contains a velocity function of the form $u=U_0\left[1+A\sin\left(2\pi ft\right)\right]$, in which U_0 is an average velocity and is given. For all the simulations, the temperature and pressure of air are 300K and 1 atm. Based on the amplitude of the forcing, there are two types of forced jets: one is the low forcing type, which has the amplitudes less than or equal to 1, i.e., $A<1$, and the high forcing type, with a greater amplitudes of $A\geq1$, in which reverse flow occurs. The high amplitude forcing flow is quite different from those with low amplitude. For this reason, both high and low forcing flows are considered and compared with the study of Barve *et al*. [161]

Again, two types of boundary conditions were used. For the wall jet and outflow boundaries, all the distribution functions were set to their respective local equilibrium distribution functions at the boundaries, $f_\alpha=f_\alpha^{eq}$ and $\overline{f}_\alpha=\overline{f}_\alpha^{eq}$. And the bounce back scheme is applied to the remaining boundaries which gives the no-slip boundary conditions.

7.7.1 Low-Amplitude Forced Flow

The centreline velocity profile for the steady jet is shown in Fig. 7.23. The results are similar to those obtained in a similar numerical study by Barve *et al.* [161]. In the figure, the low-amplitude forcing problem $A=10\%$ at the 25% phase was shown, in which it has the maximum jet exit velocity of all the phase in agreement with the results obtained by Barve *et al*. The different velocity field along the centreline indicates that the vortices were formed around the jet entrance. The oscillations in the

velocity profile also confirmed that only near the jet area can the forcing affect the flows, and farther downstream, the effect becomes weak. From Fig.7.23 it can also be seen that the results for steady jet with 10% amplitude are similar to those obtained using a finite volume methods by Barve *et al*. [161] and Pai and Hsieh [162].

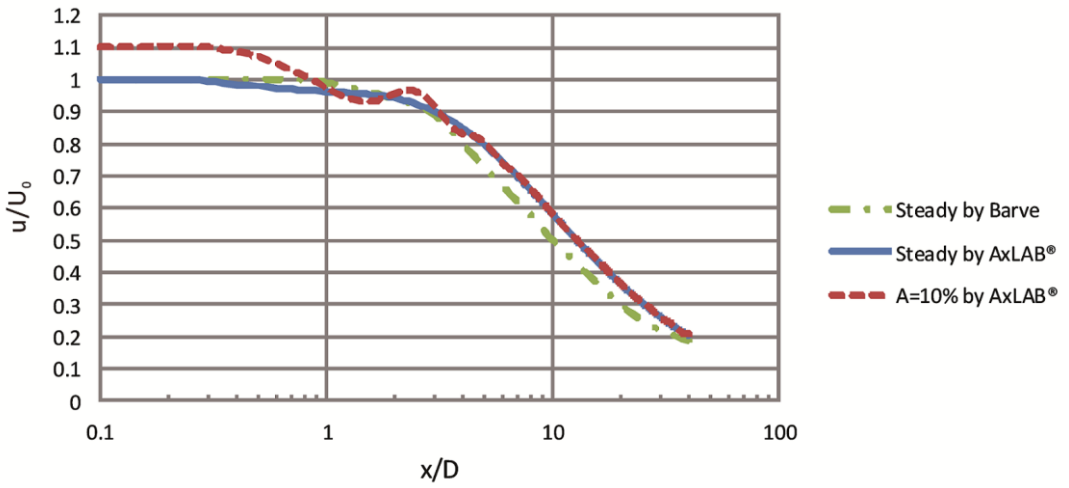

Figure 7.23 Centreline velocities for steady jets and amplitude A = 10% forced laminar jets; steady jets are compared with data from Barve *et al*.

7.7.2 High-Amplitude Forced Flow

With high amplitude forcing, Barve *et al*. expects that the vortex structures at the jet entrance will get larger and stronger. The same amplitude as considered by Barve *et al*. was used to examine this. Fig. 7.24 shows contour plots of the vorticity field along with the velocity vector for a steady flow jet for $u = U_0$ and five different phase of the jet with $A = 200\%$ amplitude forcing and f = 5Hz frequency, which are in good agreements with Brave's results. In the steady jet, the vorticity reaches peak value near the orifice, because the large velocity gradient at the jet exit plane. At the downstream, the magnitudes of the vorticity are reduced when the vorticity diffuses around the area. For the forced jet over one forcing time period, the vorticity field changed gradually, which shows the generation of the vortices at the orifice edge, followed by their ejection from the near orifice region and their subsequent convection downstream. It also shows that the vortices grow in size along the flow direction and this convectional activity form the downstream shape without interacting with each other.

Fig.7.25 depicts the centreline axial velocities at five different phases and the centreline time-averaged axial velocity for the forcing amplitude $A = 200\%$ and frequency $f = 5Hz$. As expected by Barve *et al*., the high amplitude transmits the forcing effects farther downstream compared to the low amplitude forcing case (Fig. 7.23).

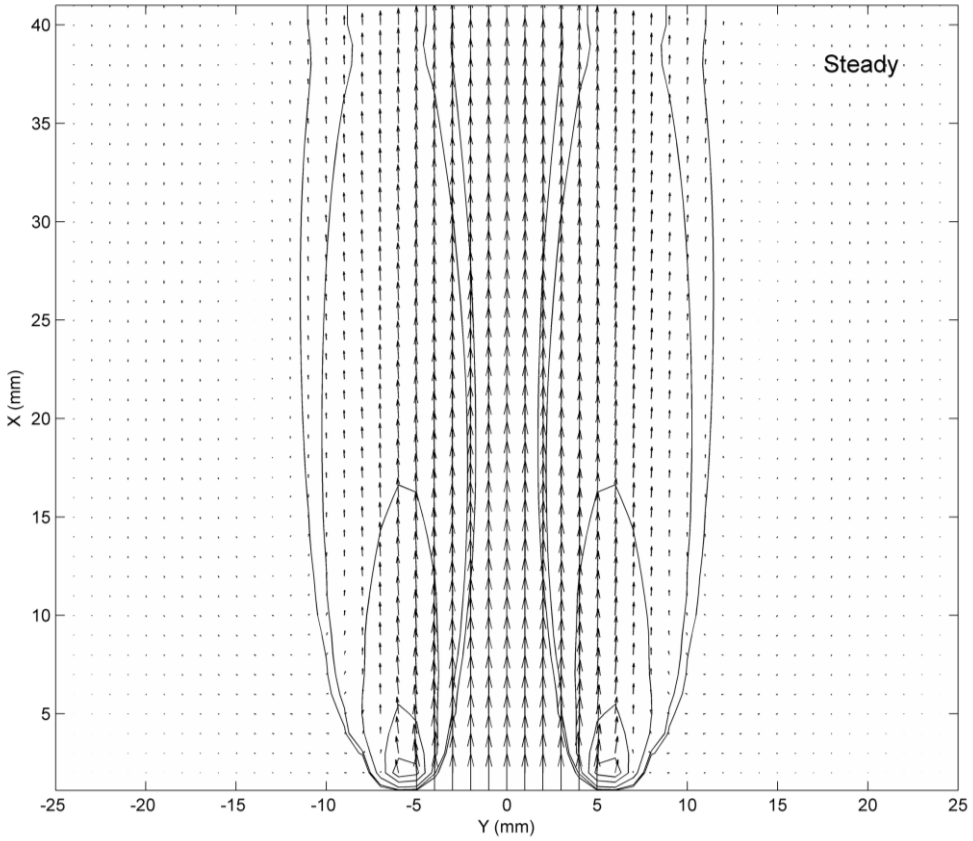

(a)

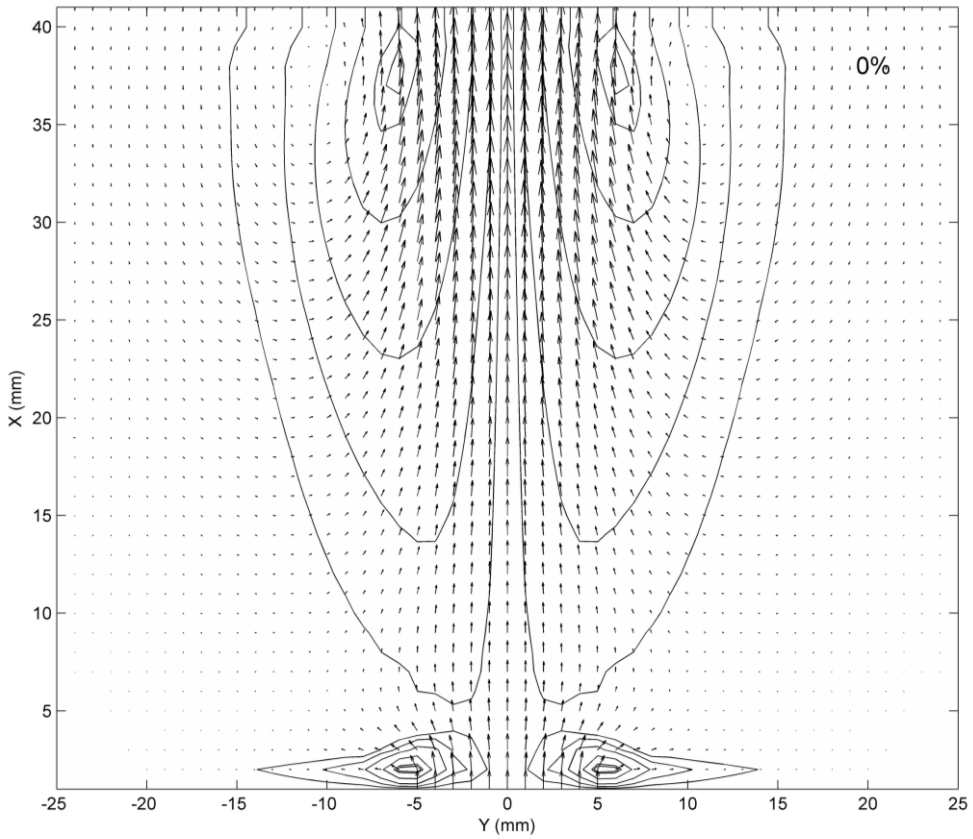
0%
X (mm)
Y (mm)
40
35
30
25
20
15
10
5
-25
-20
-15
-10
-5
0
5
10
15
20
25

(b)

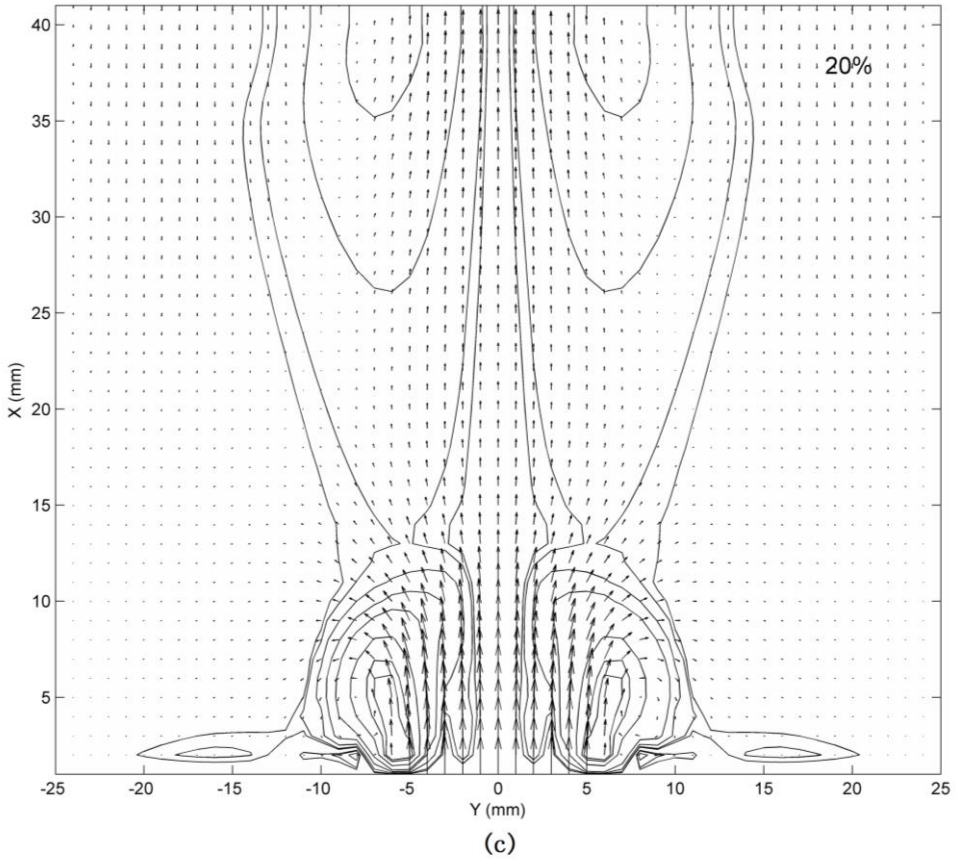
20%
X (mm)
Y (mm)
40
35
30
25
20
15
10
5
-25
-20
-15
-10
-5
0
5
10
15
20
25

(c)

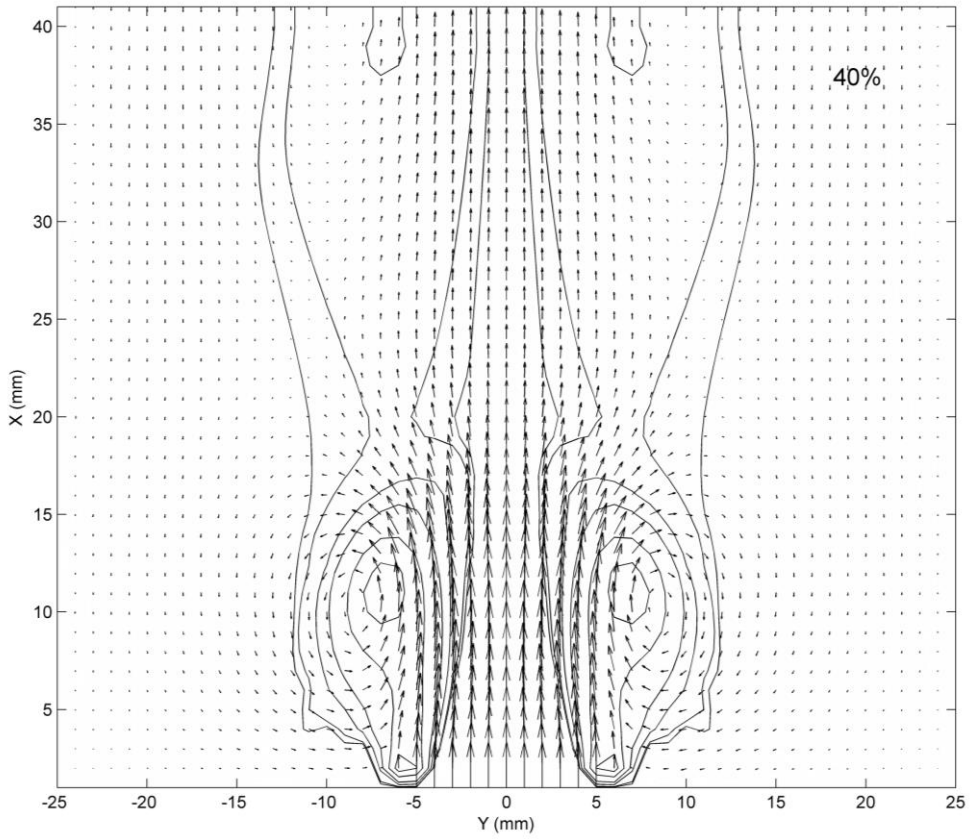
40%
X (mm)
Y (mm)
40
35
30
25
20
15
10
5
-25
-20
-15
-10
-5
0
5
10
15
20
25

(d)

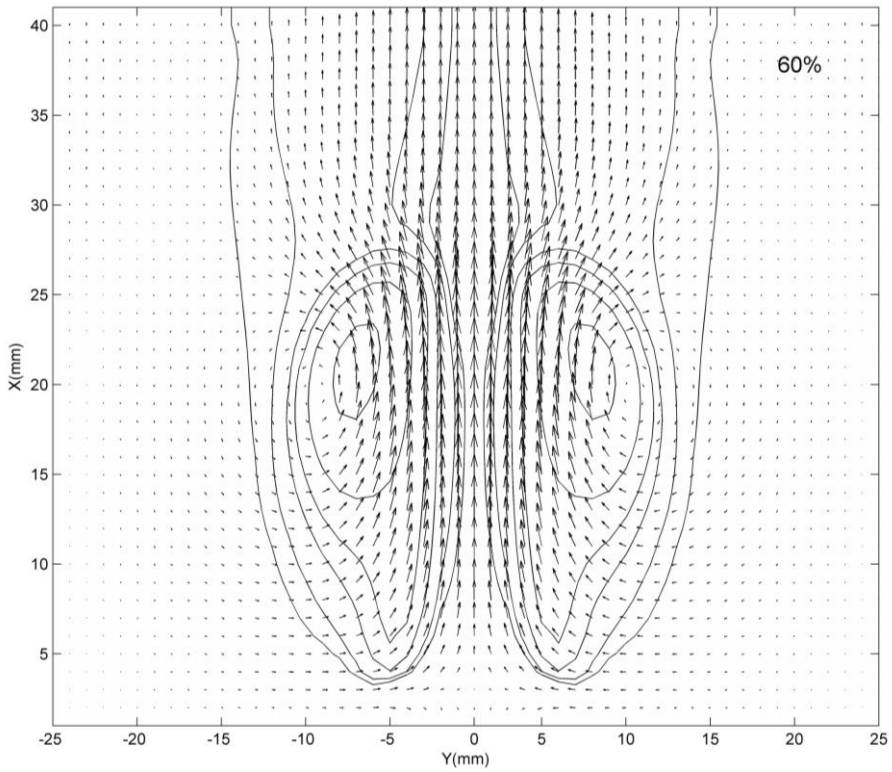
60%
X(mm)
Y(mm)
40
35
30
25
20
15
10
5
-25
-20
-15
-10
-5
0
5
10
15
20
25

(e)

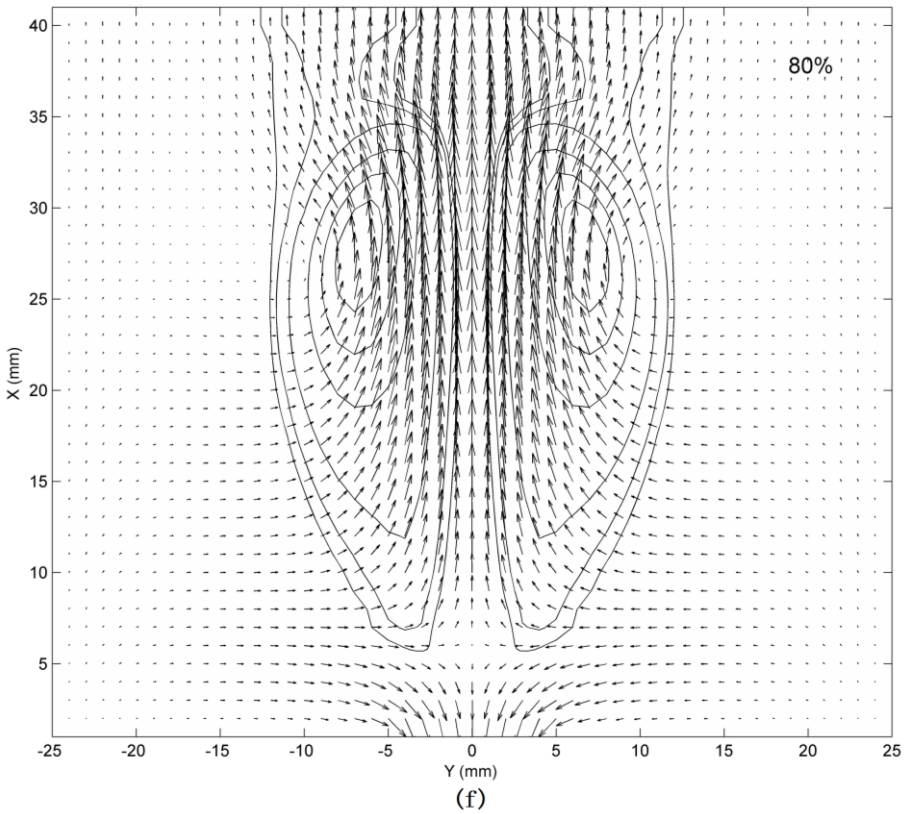

Figure 7.24 Vorticity contour plots and velocity vectors for the steady case and five different jet phases (0%, 20%, 40%, 60% and 80%) for a forcing amplitude of 200% and f = 5 Hz.

It can be observed from Fig. 7.25 that at the beginning of phase 60% and 80% the axial velocity value is below zero-that is, the axial velocity will change from negative to positive in the velocity field region. The velocity vectors near the nozzle in Fig. 7.24 clearly show this. Fig.7.26 compares the average centreline velocities for the five phases. The results from AxLAB® show a slight difference from the results of Barve *et al*., but have a similar trend. This is reasonable as there are inevitable errors in different numerical models.

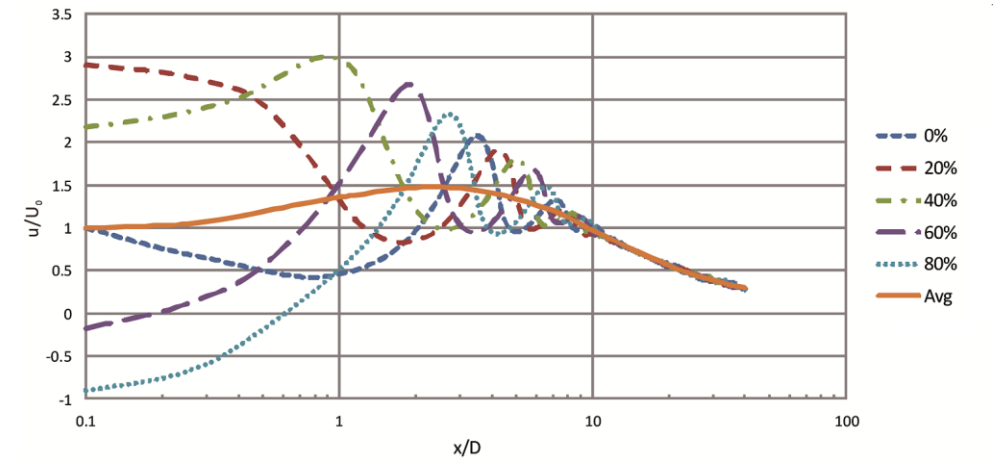

Figure 7.25 Centreline velocities against distance for 200% amplitude forcing.

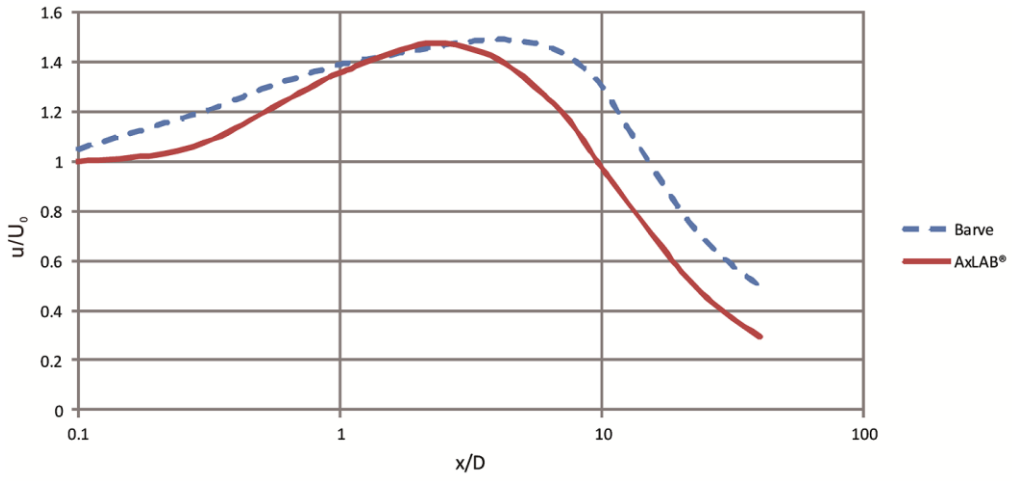

Figure 7.26 Comparison of time-averaged centreline velocities with the solution of Barve *et al*. at 200% amplitude forcing.

7.8 Swirling Flow in a Cylinder with Rotating Top and Bottom

The flow patterns for axisymmetric swirling flow in a closed cylinder with rotating top and bottom is simulated and compared with the numerical results by Shen *et al*. [163] Fig. 7.27 displayed the sketch of the flow geometry. In this circular cylinder, the radius is *R*, height is *H* and filled with an incompressible Newtonian fluid of constant density ρ and kinematic viscosity ν. The top and bottom of the cylinder are

rotating with angular velocities Ω_1 and Ω_2, respectively. The different flow regimes are specified by the Reynolds number, $\mathrm{Re} = \Omega_1 R^2 / \nu$, the aspect ratio, $\Gamma = H / R$, and the ratio of angular velocities, $\xi = \Omega_2 / \Omega_1$.

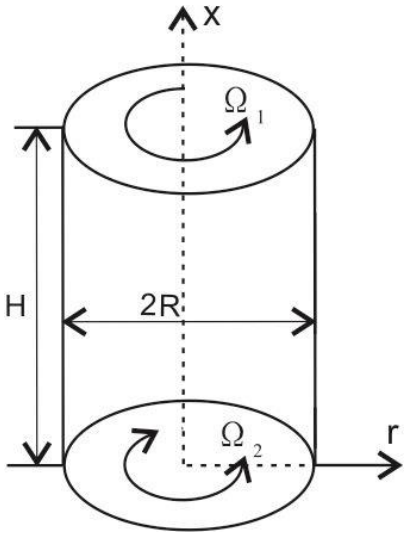

Figure 7.27 Sketch of the flow geometry.

Firstly, to validate the code, swirling flows in a cylinder with co- and counter-rotating end walls are computed and analysed at aspect ratio of $\Gamma = 2$. For the parameter studies, different ratios of angular velocities and Reynolds numbers are needed. A standard lattice mesh of medium size (100×200) is used in most of the computations in this case. To evaluate the influence of the grid, the code is validated for the case of co-rotation at a ratio of angular velocities $\xi = 0.7$ and a Reynolds number of 4000. The results shows good agreement with the study by Shen *et al*. [163]

In this swirling flow case, the flow will normally transit from an unsteady situation to a steady situation. However, sometimes the flow will transit from a steady to an unsteady regime which because the supercritical Hopf bifurcation. In the same time, the critical Reynolds number can be determined from the amplitude of velocity components that decrease linearly with the Reynolds number in the unsteady regime. Hence, the critical Reynolds number can be calculated from [163]:

$$\mathrm{Re}_{cr} = \mathrm{Re}_1 - \frac{A_1^2}{A_2^2 - A_1^2}\left(\mathrm{Re}_2 - \mathrm{Re}_1\right), \tag{7.12}$$

where subscripts 1 and 2 refer to two different points in the unsteady region that are located close to the Reynolds number.

In order to test this AxLAB® model, computations are performed at aspect ratio $\Gamma = 2,$ which is same as Shen *et al*. [163] and Gelfgat *et al*. [164] Fig.7.28 shows the stability diagrams of the critical Reynolds number in the counter-rotating region by the present method and finite volume method of Shen *et al*. In the Fig 7.28 it can be noticed that the present model have a good agreement with the model of Shen *et al*. Furthermore, when the ratio of angular velocities increase beyond -0.6, the critical Reynolds number starts to increase rapidly which indicate the steady region for a moderate counter-rotation has been enlarged. Moreover, further increasing the counter-rotation velocity, it can be seen that the size of the steady region reaches a maximum and then decreases, a sharp break can be captured around $\xi = -0.5$. After that, the critical Reynolds number stays almost flat which also reported by Shen *et al*. The reduced frequency is defined by $\omega = 2\pi f / \Omega_1,$ in which $f\,(Hz)$ is the frequency of the oscillation.

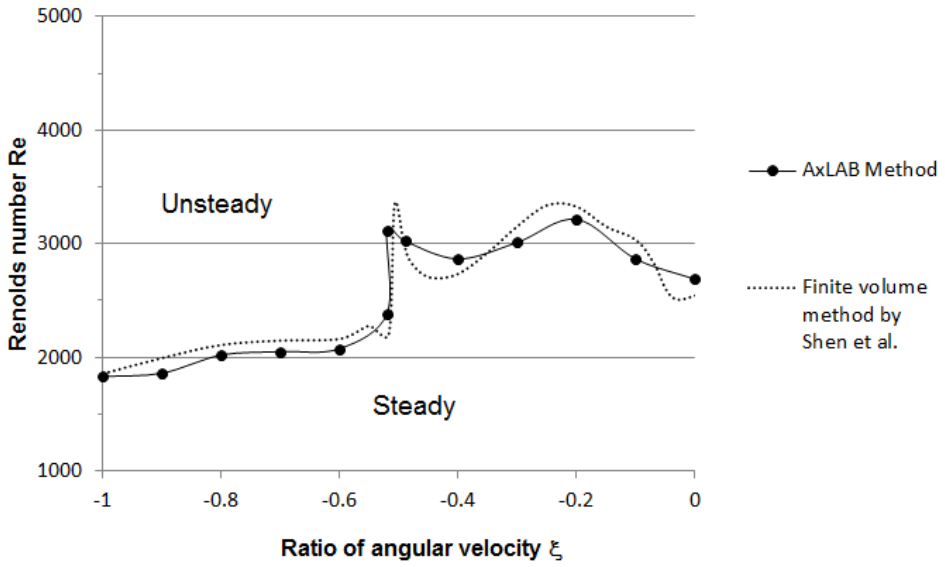

Figure 7.28 Diagrams of oscillatory instability in a cylinder with rotating top and counter-rotating bottom, $\Gamma = 2.$

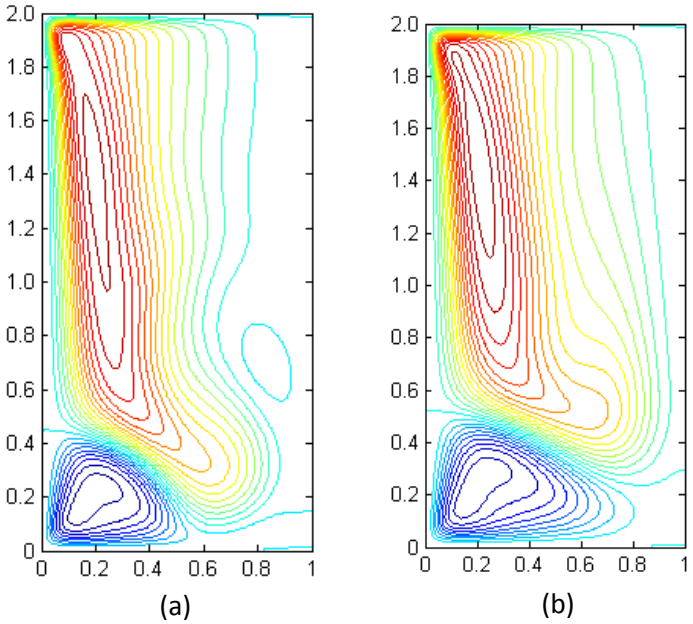

Figure 7.29 Streamlines for counter-rotating cylinder at different Reynolds number $\xi = -0.51$: (a) Re=3000, (b) Re=2200.

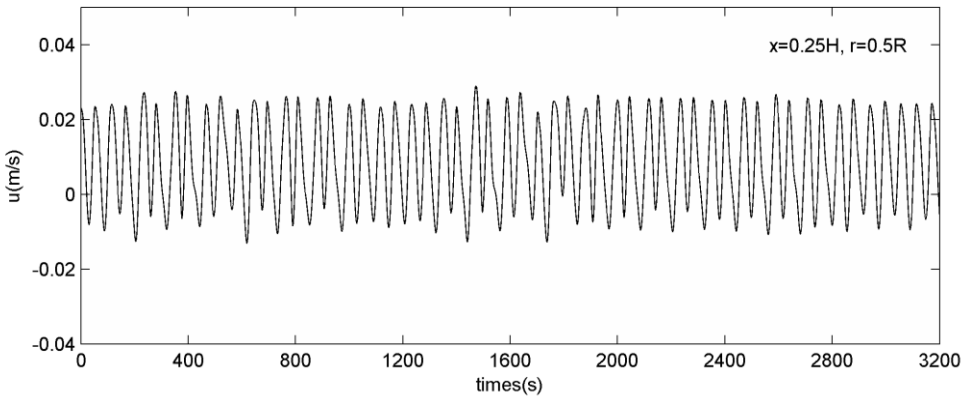

Figure 7.30 History of the axial velocity at point $(x = 0.25H,\ r = 0.5R)$.

In order to test the results of the bifurcation around the break of the critical Reynolds number at $\xi = -0.51$, two graphs were plotted in Fig 7.29. In the figures it can be noticed that in Fig 7.29 (a) there is a middle bubble and the bottom edge separation zone is smaller than Fig 7.29 (b). On the other hand, the two flow patterns are simply different. The difference also can be found in Fig 7.29 which shows the critical Reynolds number in different ratio of angular velocities and it shown that the Re=2200 and Re=3000 are not belonging to the same branch. From Fig 7.30, the history of the axial velocity confirms that the flow is periodic. Fig 7.31 illustrates the unsteady flow structure, form this set of figures, it can be noticed that the bottom edge

separate region size changes during the time and the middle bubble appears and then disappears. This situation also found by Shen *et al*. [163] who used a finite volume method.

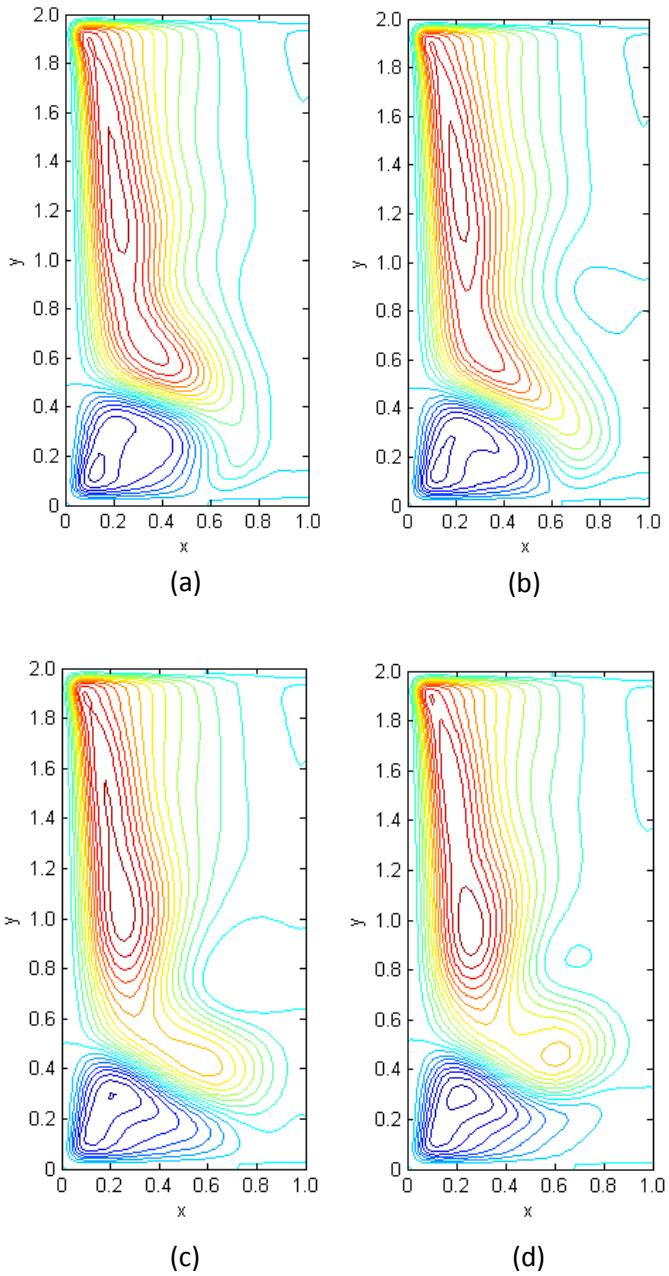

Figure 7.31 Stream lines for unsteady swirl flow in a cylinder with counter-rotating bottom at Re=3250, and $\xi = -0.52$. Four different times in a period (a) $t = t_0$ (b) $t = t_0 + T/4$ (c) $t = t_0 + T/2$ (d) $t = t_0 + 3T/4$.

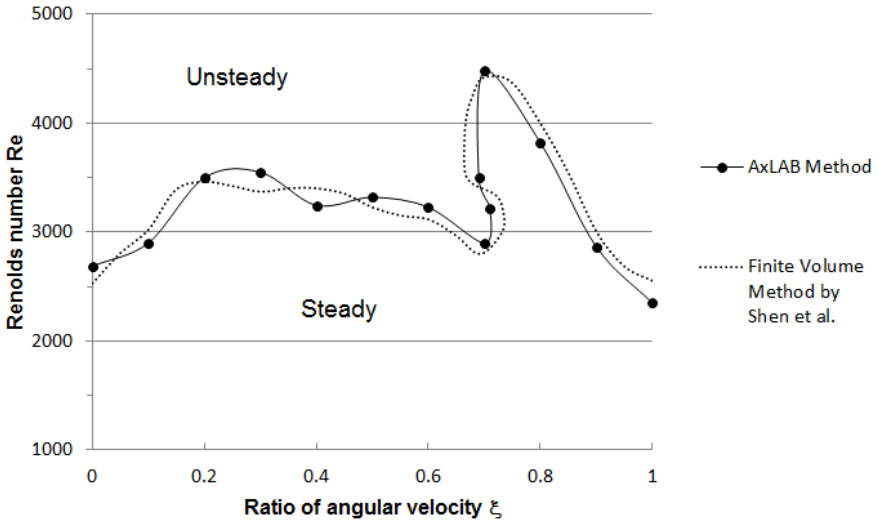

Figure 7.32 Diagrams of oscillatory instability in a cylinder with rotating top and co-rotating bottom, $\Gamma = 2$.

Next, the study is for the influence of co-rotation on the transition from steady to unsteady flow. The relation between the critical Reynolds number and the ratio of angular velocities is plotted in Fig 7.32. From this figure, at $\xi = 0.7$ an S shape appears again in which it is further compared with the other result by Shen *et al*. [163], showing a good agreement.

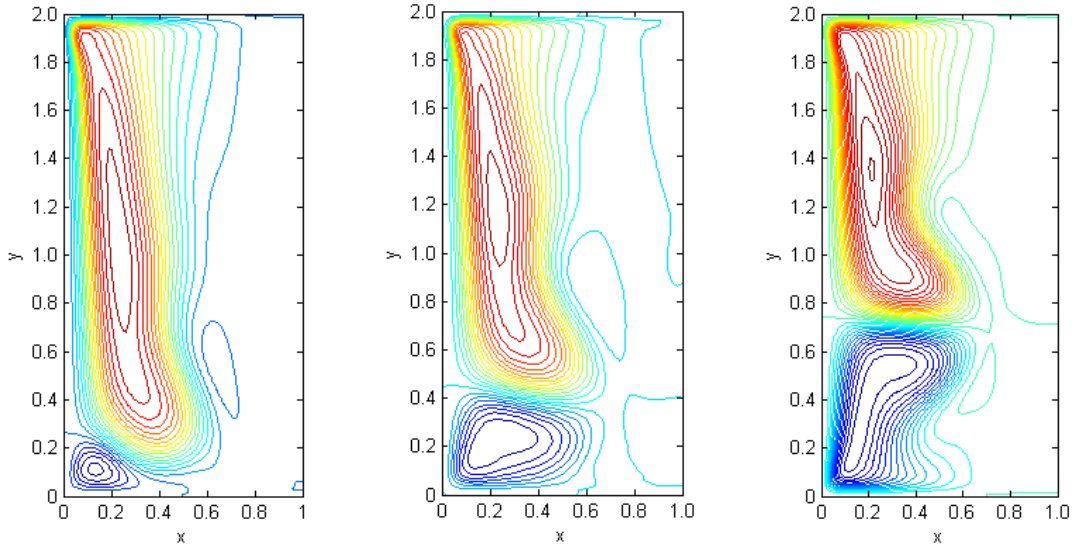

Figure 7.33 Streamlines for co-rotating cylinder at different Reynolds number and ratio of angular velocities: (a) Re=3300, $\xi = 0.3$; (b) Re=3250, $\xi = 0.4$; (c) Re=2800, $\xi = 0.7$.

Meanwhile, in order to investigate the flow behaviours around $\xi = 0.7$, the co-rotation velocities were slightly increased from $\xi = 0.3 \sim 0.7$. Form Fig 7.33, it can be seen that the size of the middle bubble increases and the separation zone appears along the edge of the bottom wall. When increasing the angular velocity up to $\xi = 0.7$, the lower separation zone also increased and push the upper bubble back toward the top wall.

From Fig 7.34, the history of the axial velocity confirms that the flow is periodic. The streamlines shown in Fig 7.35 are obtained from the unsteady flow pattern at Re=4400. It can be seen from Fig 7.35, the flow structures are dominated by the large scale fluctuation form both top and bottom of the cylinder.

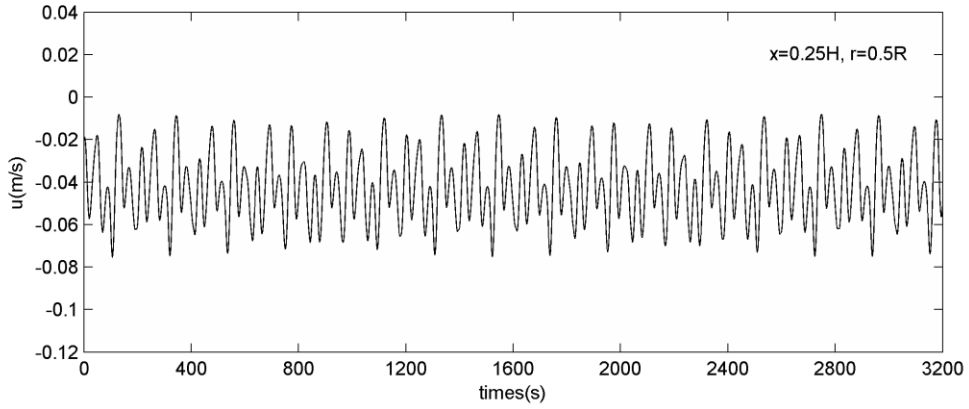

Figure 7.34 History of the axial velocity at point $(x = 0.25H,\ r = 0.5R)$.

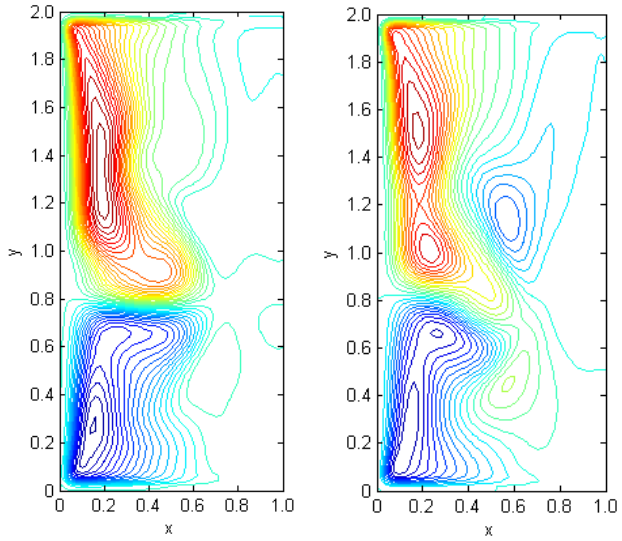

(a) (b)

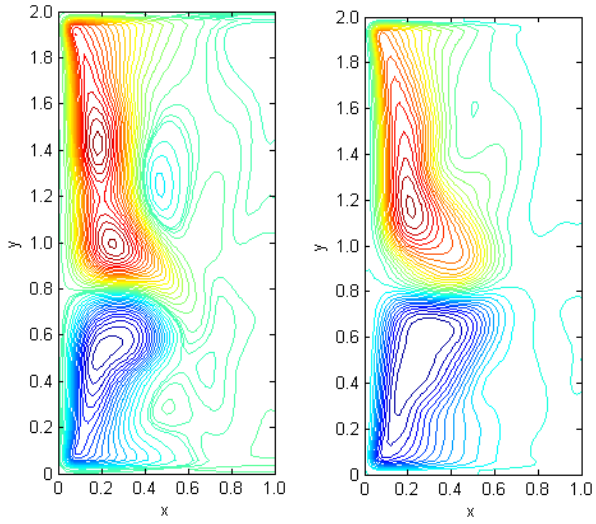

(c) (d)

Figure 7.35 Stream lines for unsteady swirl flow in a cylinder with co-rotating bottom at Re=4400, and $\xi = 0.7$. Four different time in a period (a) $t = t_0$ (b) $t = t_0 + T/4$ (c) $t = t_0 + T/2$ (d) $t = t_0 + 3T/4$.

Chapter 8: Applications to non-Newtonian Fluid Flows

8.1 Introduction of Taylor Couette Flow

Taylor–Couette flow, which has been the subject of many experimental, numerical and analytical studies for many years, is flow in an annulus with a rotating inner cylinder, a stationary outer cylinder and two end plates. Due to its industrial applications such as water purification, journal bearing and oil drilling, it is very interesting to simulate and predict its flow characteristics.

8.2 Simulation to Newtonian and non-Newtonian Fluid Taylor Couette Flow

As most applications of the flows involve non-Newtonian fluids, the AxLAB® was extended to model the non-Newtonian Taylor-Couette flows. The same problem as that used by Khali *et al*. [137] is applied to the validation and is shown in Fig. 8.1. The ratio of inner cylinder radius to out cylinder radius was chosen to be η= 0.5 and the aspect ratio $\Gamma = H / D_w$ was set to 3.8, H been the height of the cylinder and D_w is the gap between inner and outer cylinders. Initially, a constant azimuthal velocity $u_\phi = 0.15$ was set for the inner cylinder and the flow field was set to be stationary with a constant density ρ_0. The Reynolds number is defined as $\mathrm{Re} = u_\phi R_1 D_w / v$, where v is the fluid kinematic viscosity and R_1 is the radius of the inner cylinder. The Taylor number, Ta, which relates the centrifugal forces to the viscous forces, may be defined in different ways, here $Ta = u_\phi^{\,2} R_1 D_w^{\,3} / v^2$ is used [165]. From their definitions, there is a relationship between the Reynolds and Taylor numbers, $Ta = \mathrm{Re} \cdot u_\phi D_w^{\,2} / v$, which indicates that they have similar effect on the flows. For comparisons with the results available in literature, the Reynolds number is used in the study and several Reynolds number were selected for different cases. After steady solutions were obtained, the numerical results were compared with those of Liu [166] who proposed differential quadrature method to solve the vorticity-stream function

formulation in the cylindrical polar system, and Khali *et al*. who used the method of Huang *et al*. [99] to simulate similar cases.

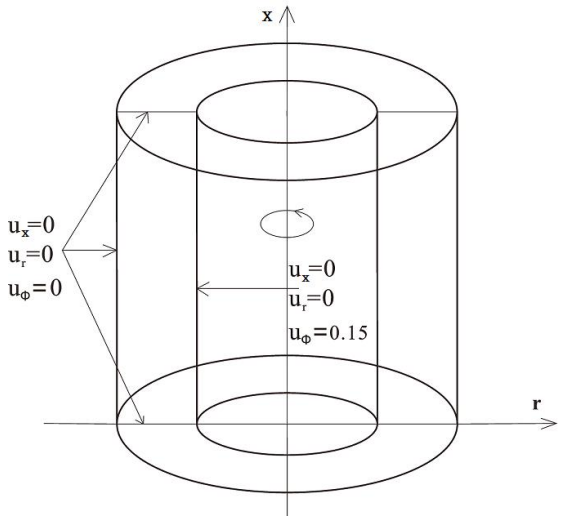

Figure 8.1 Sketch of Taylor-Couette Flow

In simulations, it is assumed that the fluid in the annular gap is incompressible, laminar and axisymmetric. In the theory, when n=1, Eq. (4.1) describes the Newtonian fluid. When 0<n<1, the effective viscosity reduces with the fluid shear rate which is called "shear-thinning" or "pseudoplastic" fluid. When $n>1$, the effective viscosity increases with the shear rate, and the fluid called "shear-thickening" or "dilatant" fluid.

There are two types of boundary conditions used in simulations. For the two end plates and outer cylinder wall, the standard bounce back rule was implemented to represent the nonslip boundary conditions. For the inner cylinder wall, all of the distribution functions are set to their respective local equilibrium distribution functions, $f_\alpha = f_\alpha^{eq}$ and $\overline{f}_\alpha = \overline{f}_\alpha^{eq}$, which is proposed by Zhou [50] and demonstrated to produce accurate solutions to rotational axisymmetric flows.

Table 8.1 Comparison of the maximum stream function $\psi_{\max}$ for Taylor-Couette flow with $\mathrm{Re} = 85,100,150$ against literature results.

Re	85	100	150
Results by AxLAB®	4.862×10^{-2}	5.556×10^{-2}	6.452×10^{-2}
Khali *et al*. [131]	4.903×10^{-2}	5.553×10^{-2}	6.361×10^{-2}
Huang *et al*. [93]	4.810×10^{-2}	5.501×10^{-2}	6.427×10^{-2}
Niu *et al*. [37]	4.859×10^{-2}	5.580×10^{-2}	6.387×10^{-2}
Liu *et al*. [161]	4.854×10^{-2}	5.542×10^{-2}	6.439×10^{-2}
average errors by Khali *et al*.	1.28%	0.22%	0.90%
average errors by AxLAB®	0.43%	0.27%	0.52%

To verify the accuracy of the developed axisymmetric lattice Boltzmann model, both Newtonian and non-Newtonian Taylor-Couette flows were tested. For the Newtonian cases, a 40×76 grid was used for three different Reynolds numbers, which are the same as those used by Huang *et al*., [99]. Comparisons of the maximum stream function values in the $r-z$ plane for cases with Re = 85, 100 and 150 are listed in Table 8.1, showing that the present model compares well with average values from the literature [42,99,166]. The average errors of the present method are smaller than those of Khali *et al*. for Re = 85 and 150 and similar for Re = 100.

The contours of the stream function and vorticity for Newtonian fluids (n=1), for Re=50, 70, 80 and 100 are illustrated in Fig. 8.2, which shows the effect of the Reynolds number on the flows. The flow structure at Re=50 (Fig. 8.2 (a)) is characterized by the so-called Ekman vortices at the end of the walls because of the non-slip boundary condition. When Re increases from 50 to 70, another pair of cells is going to form in the centre of the cylinder, which can be seen in Fig. 8.2 (a, b). The

critical Reynolds number at the beginning of Taylor vortex flow is $\mathrm{Re}_c = 68.4$ where the flow starts to switch to the four-cell regime. When $\mathrm{Re} > \mathrm{Re}_c$, the centrifugal force has more effective in the annulus than the viscous forces and the flow is dominated by the laminar unstable regime, and as Re further increases to 100, the flow structure switches completely from two-cell to four-cell. In each figure, the stream lines and vorticity contours are presented to show the effect of the Reynolds number.

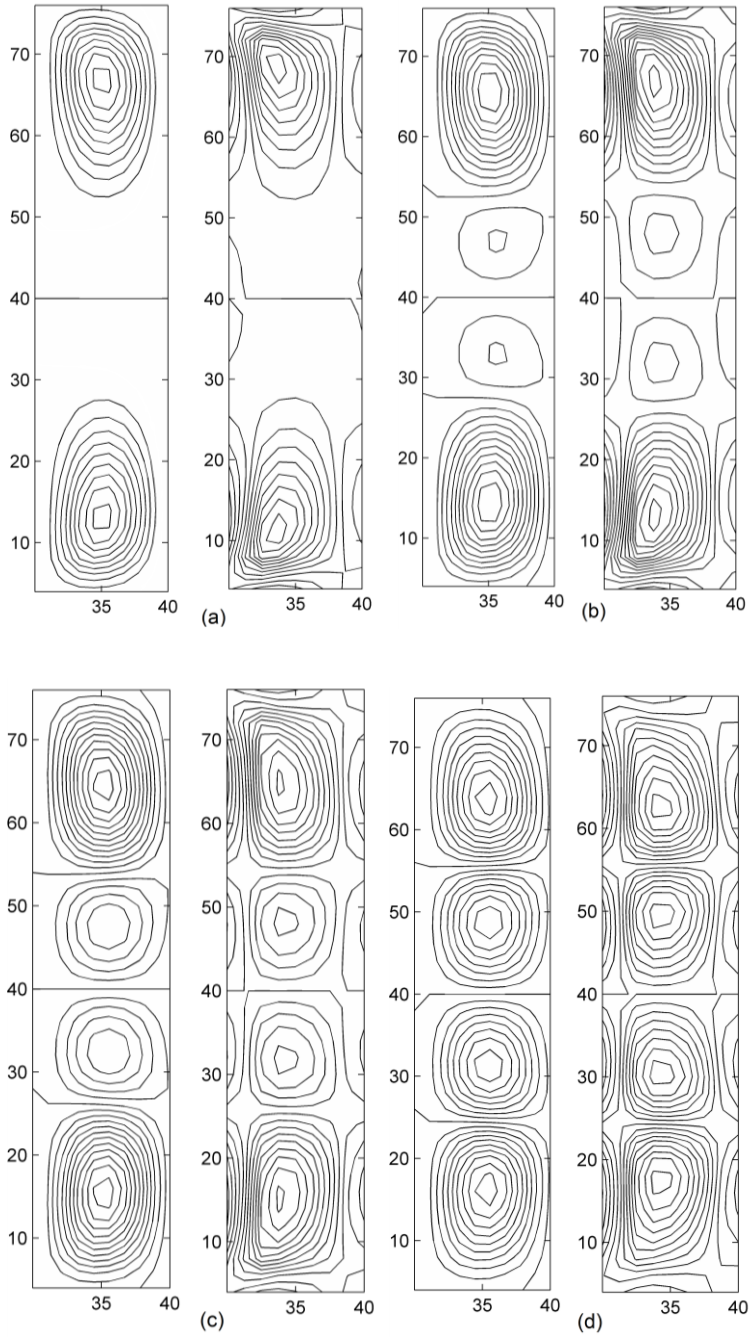

Figure 8.2 Stream function and vorticity contours for Newtonian fluids (*n*=1): (a) Re=50, (b) Re=70, (c) Re=80, (d) Re=100.

For non-Newtonian fluid flows, the exponent n is set to values of 0.5 and 1.5, with the Reynolds number chosen to be in the range 65-150, which is the same as in the study of Khali *et al*. [137]. Fig. 8.3 and 8.4 show the combined effects of Reynolds number and the power-law index on the stream function and azimuthal vorticity. For the Newtonian fluid flow chart, there is an Ekman cell forming at Re=70, but for the non-Newtonian fluid (n=0.5) the middle two cells are forming at about Re=65 (Figure 8.3(a)); when n=1.5, this transition occurs at approximately Re=75. For a further increase in Reynolds number, the two cells flow pattern is fully developed to four cells pattern at Re=80 for n=0.5 and Re=150 for n=1.5, respectively. Moreover, it can be noted that when the Reynolds number increases to 111.5 the flow structure changes from four-cell to two-cell regimes when n=0.5, which is same as those reported by Khali *et al*.[137].

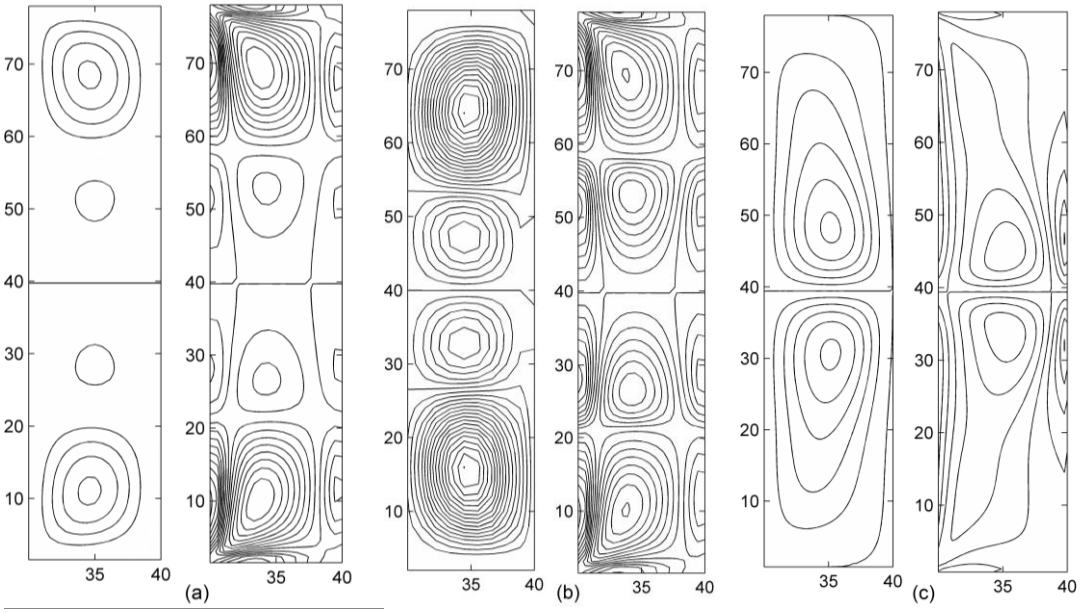

Figure 8.3 Stream function and vorticity contours for Newtonian fluids (n=0.5): (a) Re=65, (b) Re=80, (c) Re=111.5.

Fig. 8.5 compares velocity profiles from AxLAB® and the model of Khali *et al*.: when n increases from 0.5 to 1.5, both the radial and axial velocity decreases due to the rheological behaviour of the non-Newtonian fluid. According to the comparisons, it is clear that the axisymmetric lattice Boltzmann model (AxLAB®) and the model of Khali *et al*. produce very similar results.

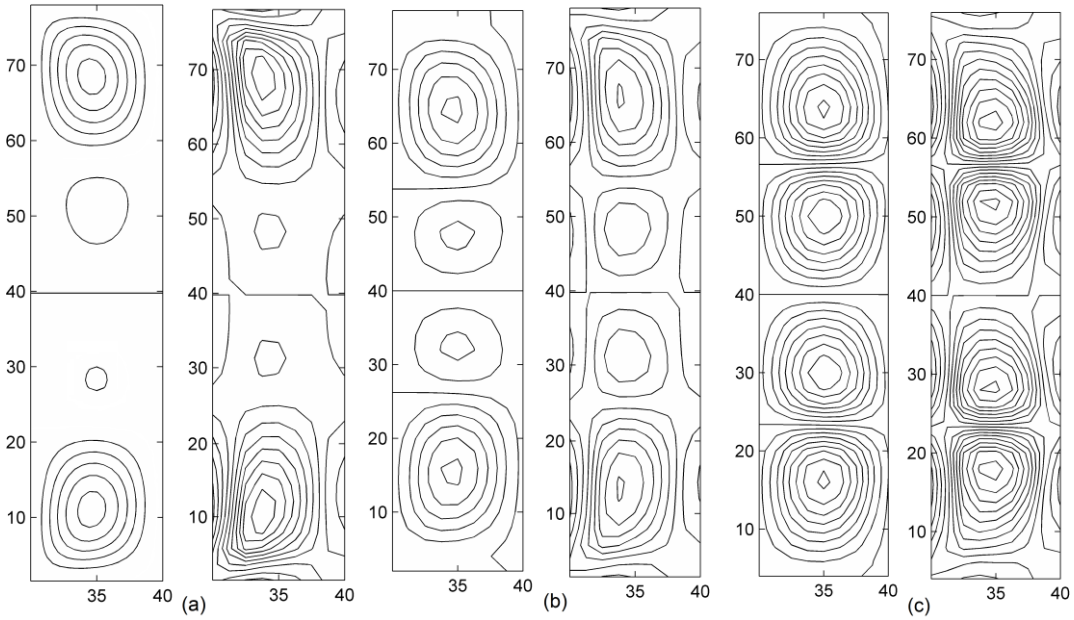

Figure 8. 4 Stream function and vorticity contours for Newtonian fluids (n=1.5): (a) Re=75, (b) Re=80, (c) Re=150.

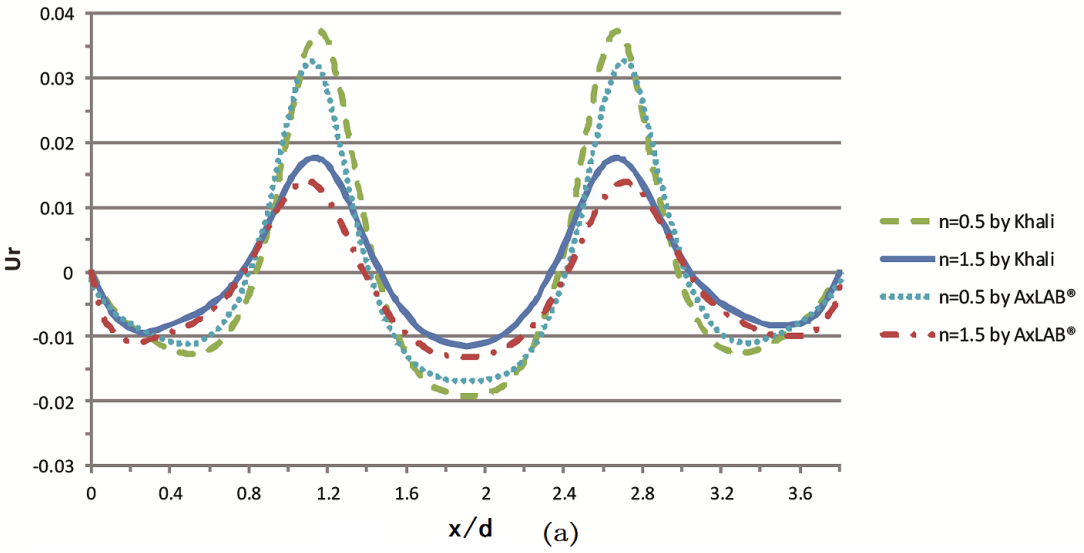

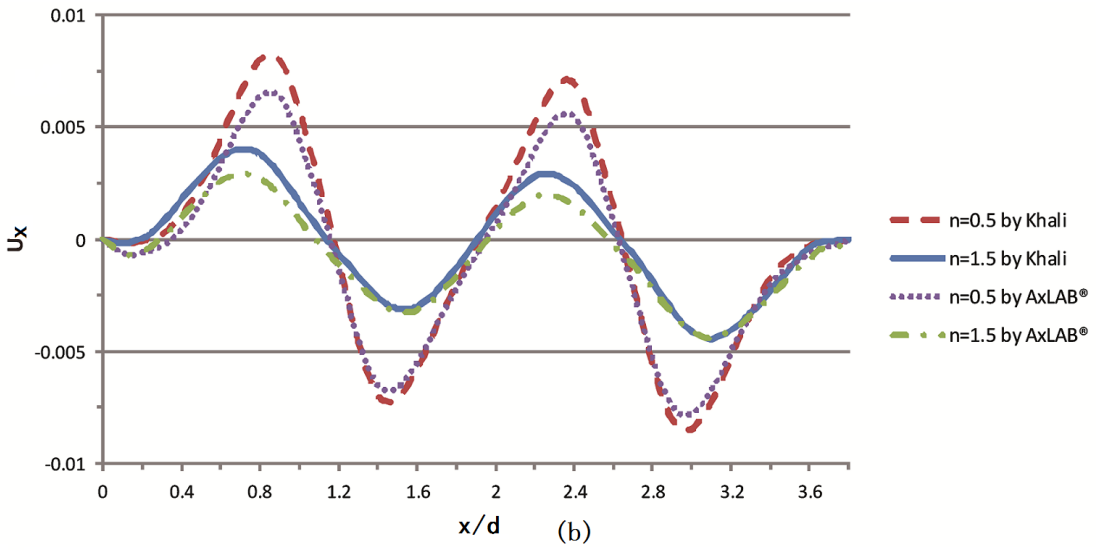

Figure 8.5 Comparison of velocity profiles with the results of Khali *et al*. for different values of *n* at Re =100: (a) radial velocity profile along *x/d*; (b) axial velocity profile along *x/d*.

The enhanced axisymmetric lattice Boltzmann method AxLAB® is presented and extended to model the Newtonian and non-Newtonian Taylor Couette flows. The effect on the flow pattern of several parameters such as the Reynolds number and the power-law index n are analysed. The results show that when $\mathrm{Re} \geq \mathrm{Re}_c$, the flow changes from the stable laminar regime to the unstable laminar regime and its structure switches from the two-cells to four-cell mode for both Newtonian (n=1.0) and dilatant fluids (n=1.5). On the other hand, for pseudoplastic fluids (n=0.5), the flow shows from two-cells to four-cells and switches again to the two-cell configuration. The results are compared with those reported in the literature. It is found that the AxLAB® model is easy and simple to simulate non-Newtonian fluid flows; it can predict complex axisymmetric flows and capture the typical features efficiently at the comparable accuracy to other conventional methods. Using the local equilibrium distribution function as the boundary conditions is also simple and can produce the accurate results to the Taylor-Couette flow.

Chapter 9: Applications to Turbulent Flows

9.1 Flows through an Abrupt Axisymmetric Constriction

The first case is a simulation of turbulent flow through an axisymmetric constriction that was reported by Andersson [167]. A schematic representation of the flow geometry is shown in Fig. 9.1. The length of the computational domain is $5D$, where D is the diameter of the cylindrical domain. The axisymmetric constriction is given by the shaded area in Fig. 9.1 and the constriction height and length are H and l, respectively. The relation between H and l is $H = 0.5l = 0.25D$. At the inlet and the outlet, as described in Andersson [167], the flow is generated as a laminar Poiseuille flow with added random disturbances to generate turbulent transition. It is driven by an axial pressure gradient at the inlet of the pipe which keeps the bulk flow constant at U_b. The Reynolds number is 22000, which is same as Wang [168]. The similar experiment was also studied and described in the report by Wang [168], in which a closed-circuit pipe flow was generated. The long inlet and outlet provided fully developed turbulent flow within the test section. A slip boundary condition is implemented at the top and bottom walls of the domain. Simulations were performed on uniform lattices of 500×100; the time step Δt is 0.2s, and the Smagorinsky constant $C_s = 0.3$ is used. The numerical results are compared with the experimental data [168] to validate the present model, where all lengths and velocities are nondimensionalized by D and U_b, respectively.

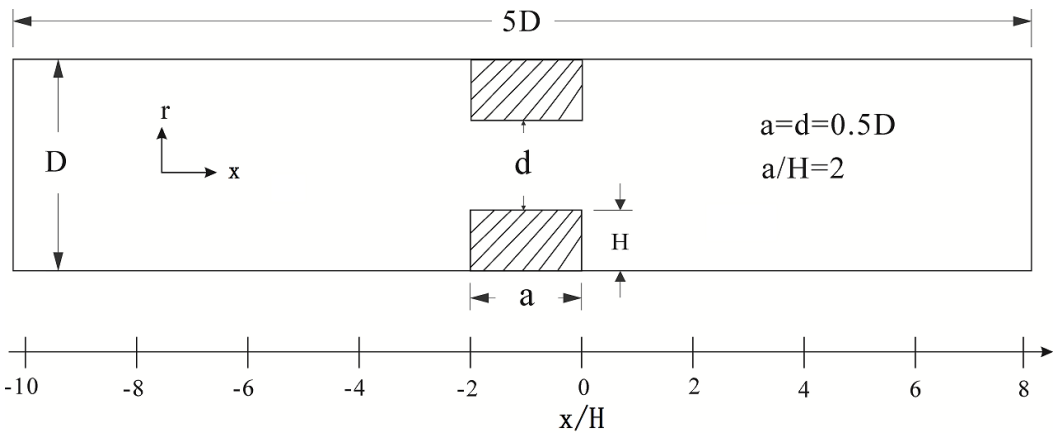

Figure 9.1 A schematic representation of the flow geometry.

The centreline velocity profile for the pipe flow is shown in Fig. 9.2, which is similar to that obtained using a different numerical study by Andersson [167]. The point $x/H=0$ is selected at the end of the shaded rectangle in Fig.9.1. According to Fig. 9.2 the flow shows a sudden acceleration just before of the constriction and thereafter decelerates as the high speed jets exit from the annular ring. But, before the point $x/H=-5$, the flow has developed fully as normal pipe flow which is also confirmed by the experiment data. Comparisons of the mean axial velocity profiles at four different locations downstream of the constriction are shown in Fig. 9.3, which indicate good agreements with the experiments by Wang [168]. In the comparison at $x/H=12$ in the figure, there are some relatively larger errors at the area near the wall; which may be due to the effect of the boundary condition used in this situation. The velocity histories at two typical points across the channel are plotted in Fig. 9.4, showing velocities fluctuation around the mean velocity, and their averaged velocity over sufficient long time period is constant. This confirms that turbulence modelling based on a subgrid-scale stress model can provide more details than a time average turbulence model such as the $k-\varepsilon$ model [56].

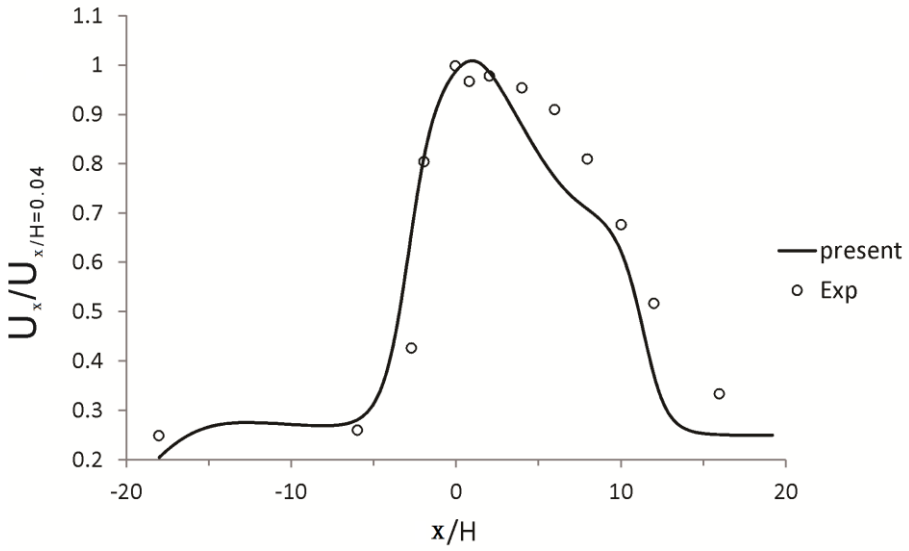

Figure 9.2 Comparison of axial distributed mean streamwise velocities at the centreline.

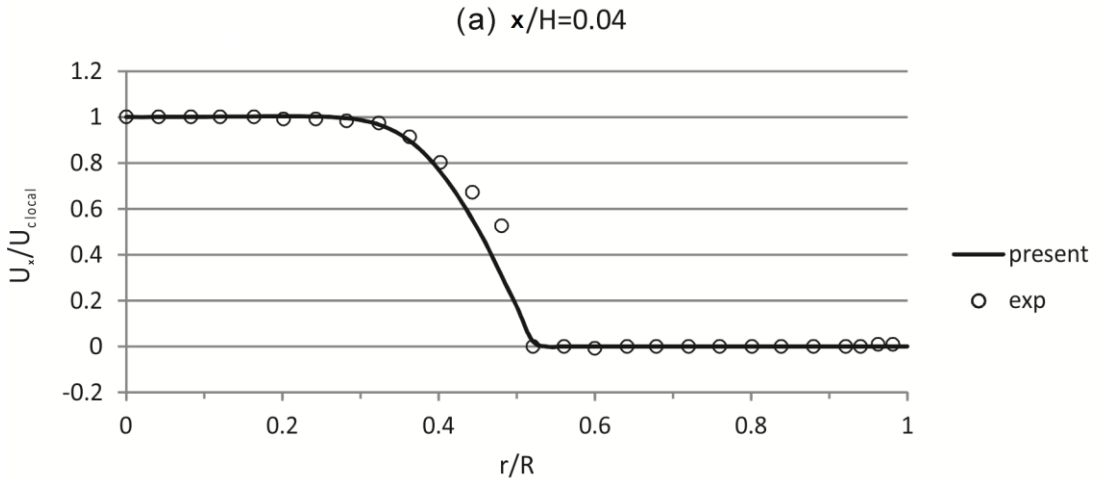
(a) x/H=0.04
1.2
1
0.8
0.6
0.4
0.2
0
-0.2
0
0.2
0.4
0.6
0.8
1
r/R
U_x/U_{clocal}
present
exp

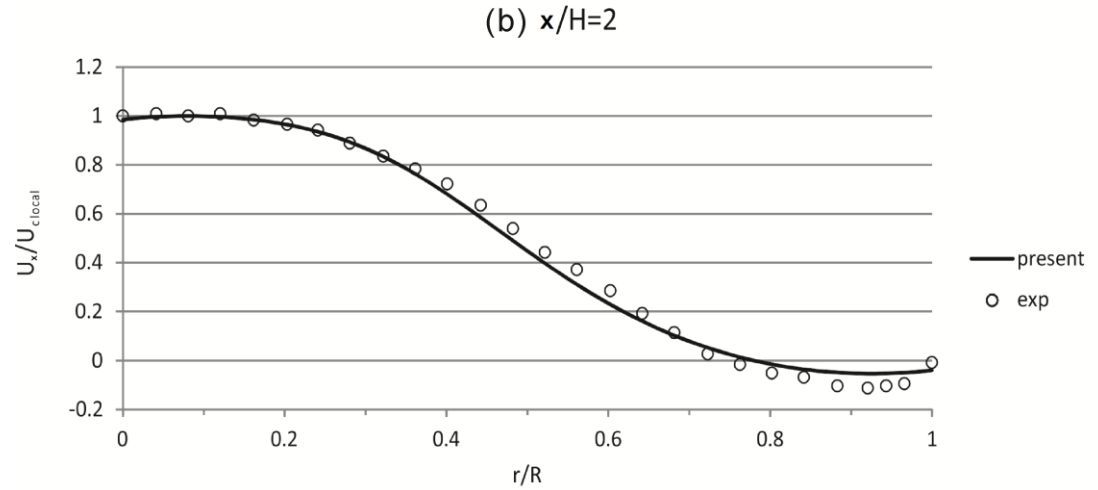
(b) x/H=2
1.2
1
0.8
0.6
0.4
0.2
0
-0.2
0
0.2
0.4
0.6
0.8
1
r/R
U_x/U_{clocal}
present
exp

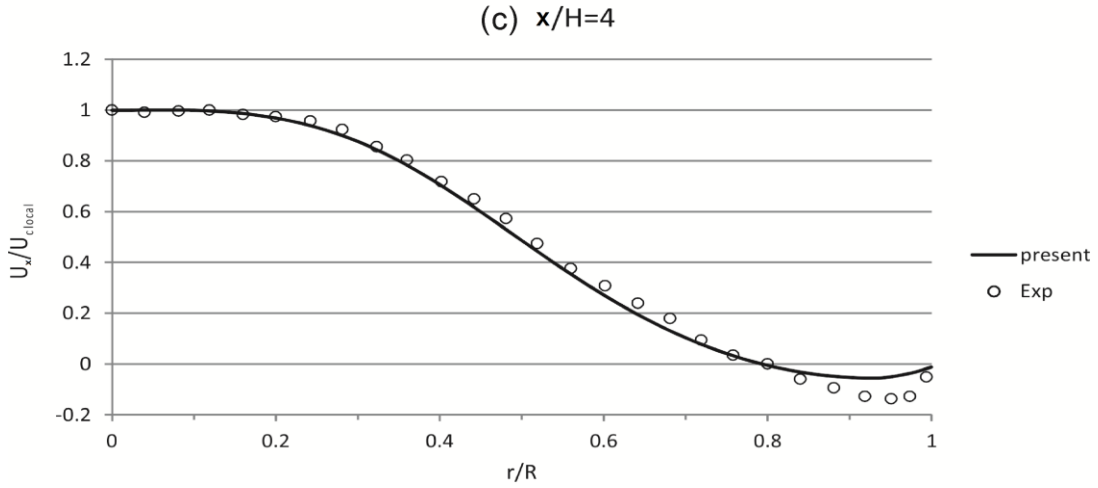
(c) x/H=4
1.2
1
0.8
0.6
0.4
0.2
0
-0.2
0
0.2
0.4
0.6
0.8
1
r/R
U_x/U_{clocal}
present
Exp

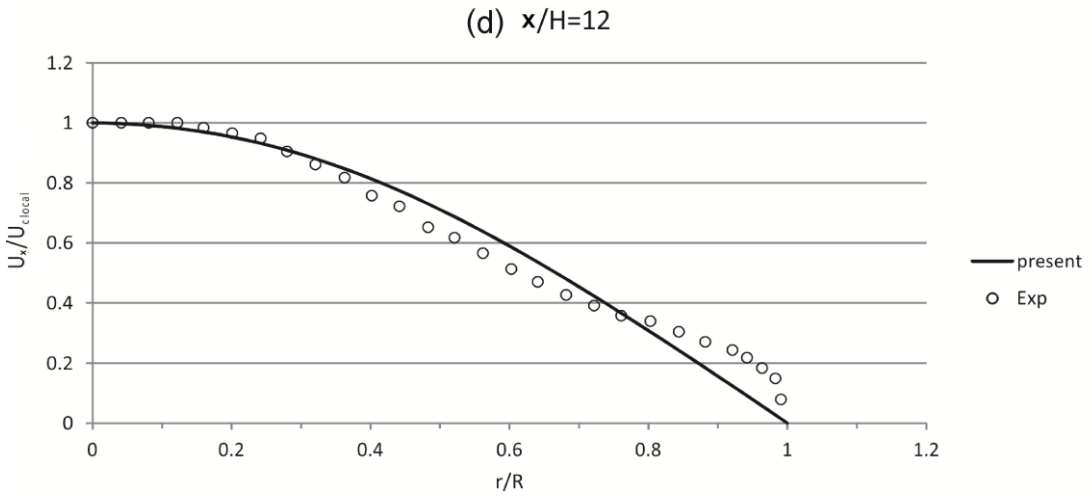

Figure 9. 3 Comparison of the mean axial velocity profiles at different locations, (a) $x/H = 0.04$, (b) $x/H = 2$, (c) $x/H = 4$, and (d) $x/H = 12$.

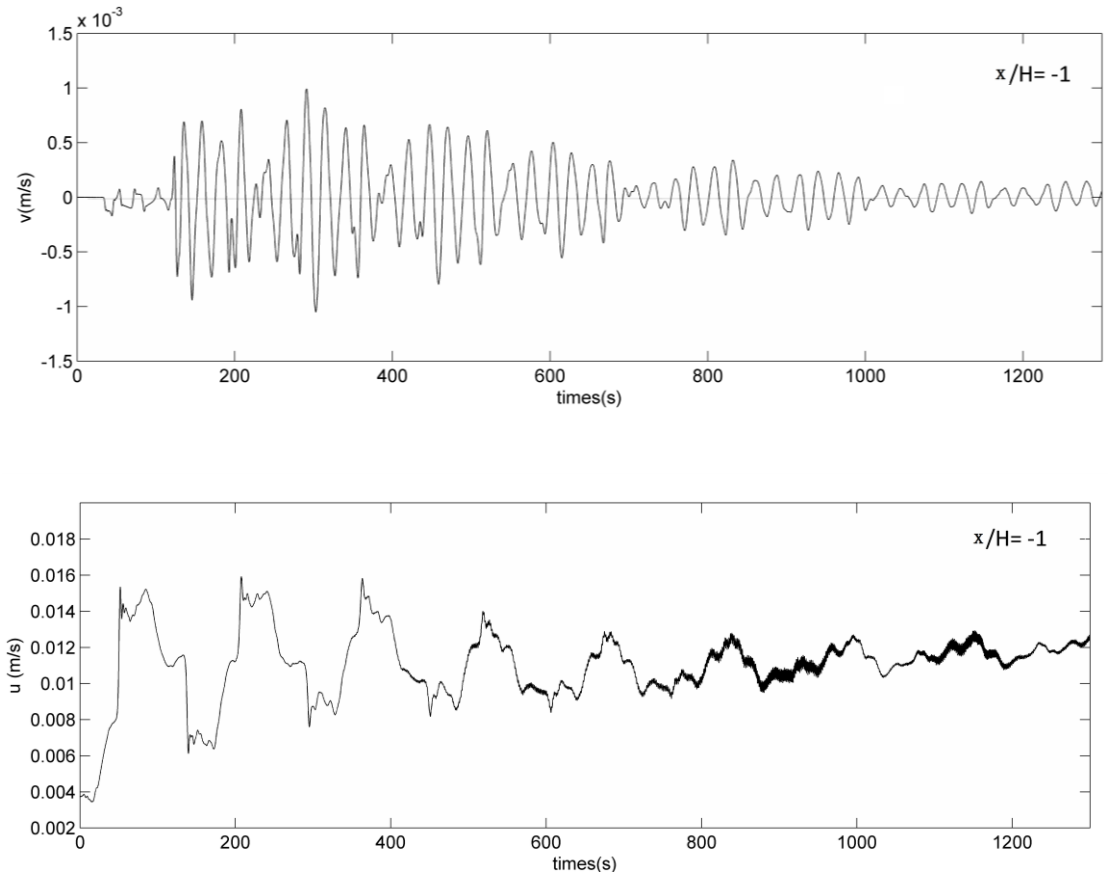

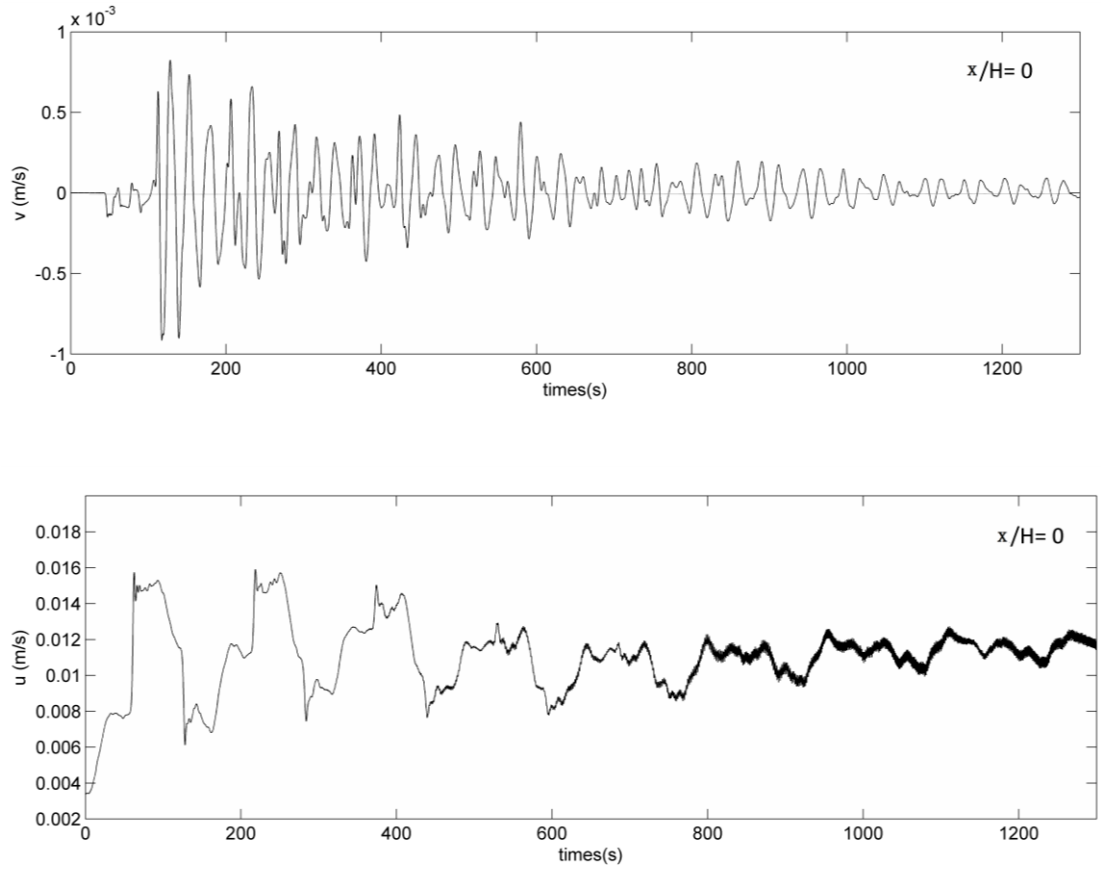

Figure 9.4 Histories of centreline longitudinal and latitude velocities at two points: $x/H = -1$ and $x/H = 0$.

9.2 Axisymmetric Separated and Reattached Flow

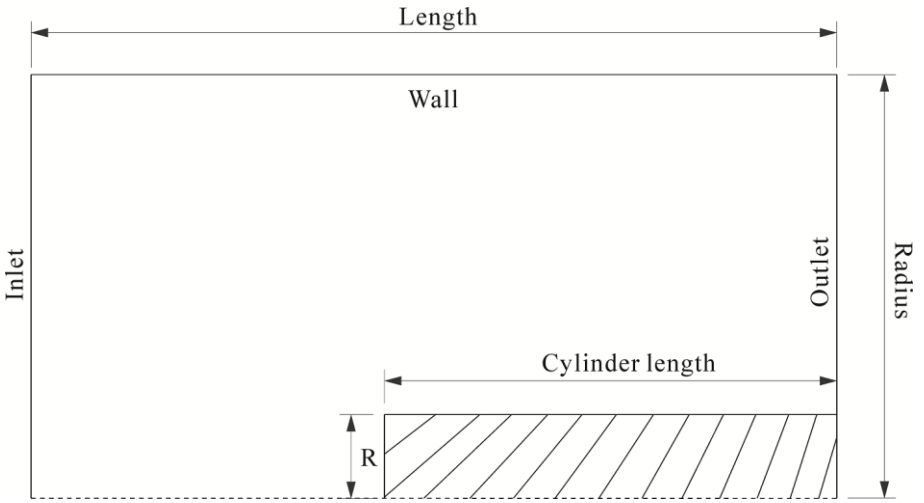

Figure 9.5 Computational domain and boundary conditions.

An axisymmetric separated and reattached turbulent flow has been well reported by Rastgou and Saedodin [169] and used as the second test case for the present model. In this case, the axisymmetric flow past a longitudinal circular cylinder with blunt leading edge is simulated. The schematic configuration of the computational domain and the boundary conditions are shown in Fig.9.5. The radius of the cylinder is R; the domain length was set to 40R; the domain radius is 30R from the axis; and the head of the cylinder was located at 25R from the inlet. The computations are carried out using 800×600 lattices, where the wall is treated using no-slip boundary conditions. The Reynolds number for flow is 6000 that is same as the study by Rastgou and Saedodin [169].

Comparisons of velocities with those using other numerical solutions are shown in Figs. 9.6 and 9.7, indicating reasonably good agreement at the similar accuracy to that by Rastgou and Saedodin [169]. Furthermore, the comparisons between the experimental results of Ota [170] (Re=56200) and Kiya *et al*. [171] (Re=10^5) also confirm that small discrepancy may exist in the reverse flow region depending on the Reynolds number. One of the key characteristics in study of Rastgou and Saedodin is the reattachment length, which is defined as the distance between the separation point and the reattachment point. The experimental results by Ota [170] and Kiya *et al*. [171] reveal that the reattachment length of turbulent separated shear layer is independent of Reynolds number, which is about 1.6 times the diameter. Figs. 9.8 and 9.9 show the streamlines and the mean velocity vector field in the neighbourhood of the separated and reattaching flow region, respectively. It can be seen from the figures that the present model results in a reattachment length of 1.62 times the diameter, which also shows good agreement with the experimental data, suggesting that the present model has a good performance in simulating complex flows in the logarithmic region.

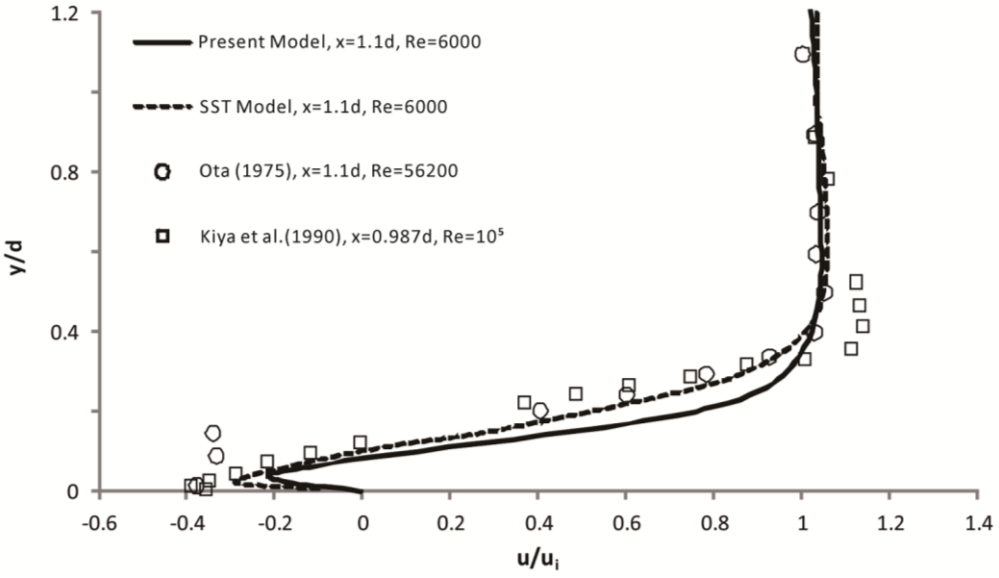

Figure 9.6 Distribution of mean velocity at a section in the separation region.

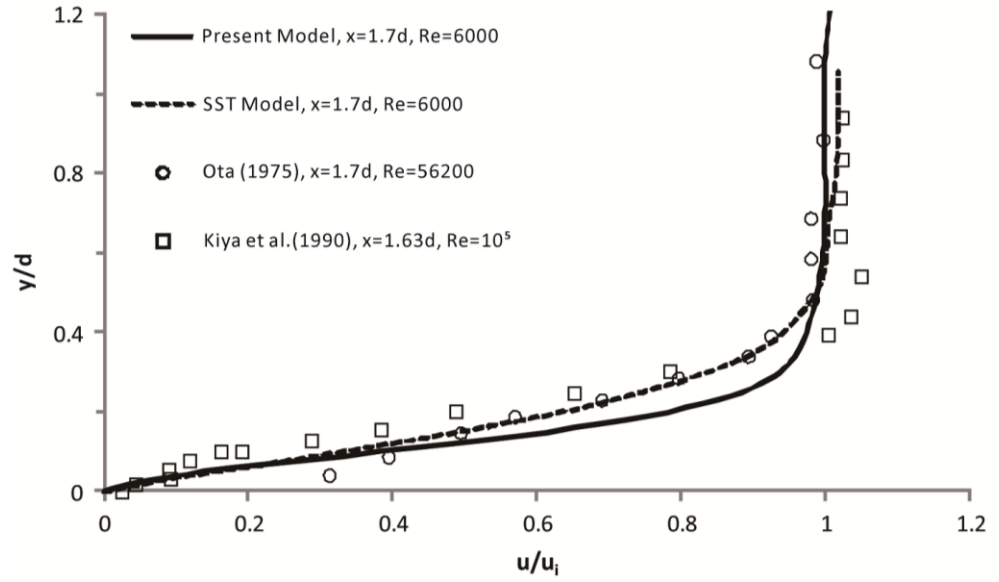

Figure 9.7 Distribution of mean velocity at a section out of the separation region.

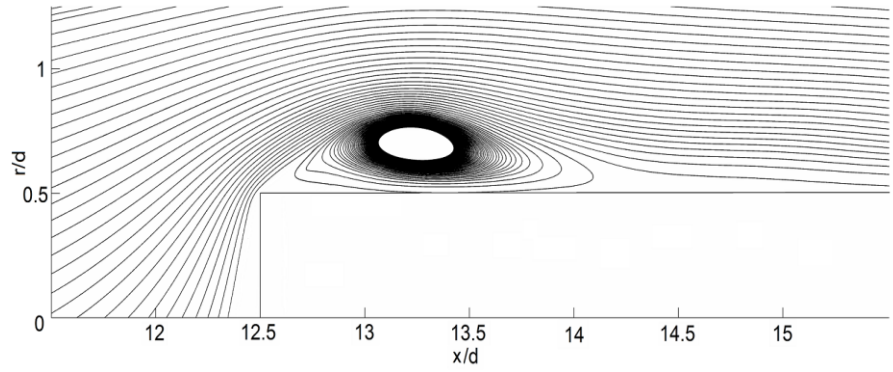

Figure 9.8 Streamlines using the AxLAB® with turbulent.

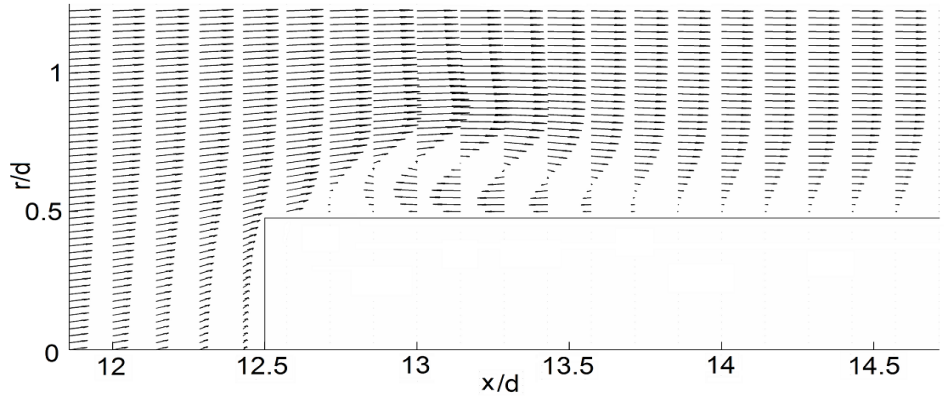

Figure 9.9 Velocity vector field using the AxLAB® with turbulent.

9.3 Pulsatile Flows in a Stenotic Vessel

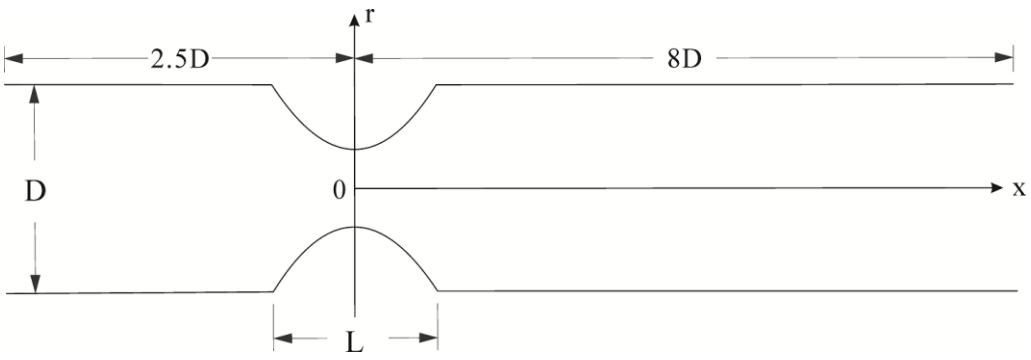

Figure 9.10 Geometry for the smooth stenosis vessel.

The pulsatile stenotic flow was investigated using experiment by Ahmed and Giddens [172]. This is also simulated as the last test, which was also studied by Varghese and Frankel [173] using the Low Re $k-\omega$ model. In this test, the time periodic period, T, is calculated in terms of the angular frequency, ω, as $T=2\pi/\omega$. In the numerical simulation, a periodic boundary condition was applied to the inlet of the tube and outlet; the inflow velocity is set to

$$U=U_0+U_m\sin(\omega t), \tag{9.1}$$

where U_0 is the mean velocity set as 0.04254 (m/s) and U_m is taken as a fraction of U_0 set as 0.02808 (m/s), and ω =0.314 (rad/s). The density of the flow is $\rho=1000(kg/m^3)$ and the viscosity is μ=$3.614\times10^{-3}(Pa\cdot s)$. Fig. 9.10 is the

geometry of the stenosis vessel with the diameter of $D = 0.0508\ m$ and the stenosis is described by the following function:

$$S(x) = s_0 r_0 \left\{1 - \cos\left[2\pi\left(x - x_1\right)/\left(x_2 - x_1\right)\right]\right\}/2, \tag{9.2}$$

where s_0 is the % stenosis severity with x_1 and x_2 $\left(x_1 < x < x_2\right)$ specifying the position and length of the stenosis. A 75% axisymmetric stenosis was used in this test. Pulsatile flow was set at a mean Reynolds number of 600 and a Womersley number of $\alpha = D/2\sqrt{(\omega/\nu)} = 7.5,$ which is the same as that in the experiment by Ahmed and Giddens [172] and the study by Varghese and Frankel [173].

The flow input waveform and the times at which the results are presented are shown in Fig 9.11 which is the same as Varghese's research. A flat inlet velocity profile was proposed 2.5 times the diameter before the stenosis throat. Computed velocities at five different locations were compared with the experiment data and Varghese's results during the peak inlet flow (T2) as shown in Fig 9.12. From the figure, it can be seen that all of the five velocities results from the present model have more accuracy than Varghese's results. Also they have good reasonable trend to the experiment data. But in the experiment the entrance length of the tube before the constriction was 96 times the diameter [172]. The streamlines at different times computed by present model are plotted in Fig 9.13, which indicates a region of flow vortex just after the stenosis, which is also consistent with the reverse flow reported by Ahmed and Giddens [172].

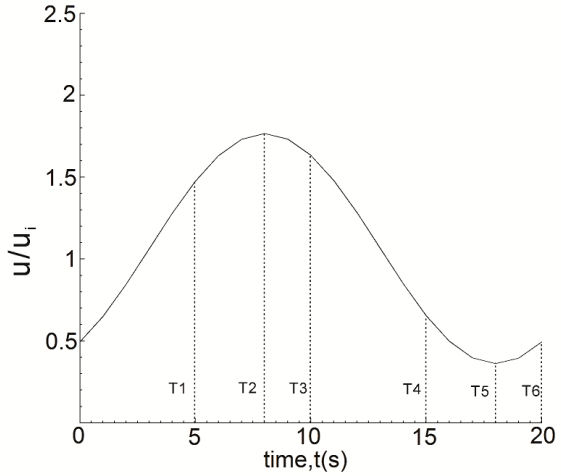

Figure 9.11 Flow inlet waveform for the smooth stenosis.

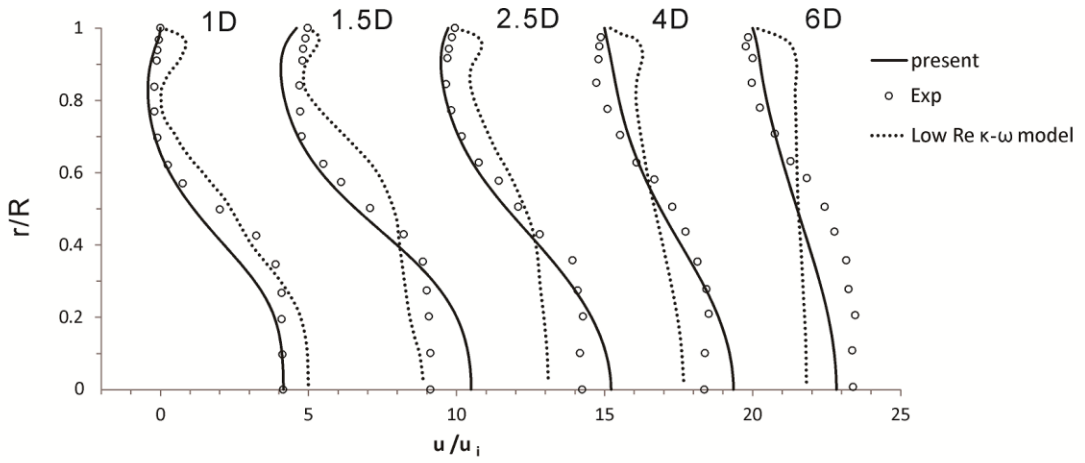

Figure 9.12 Comparisons of the radial velocity profiles at five different locations among the two models and the experimental results.

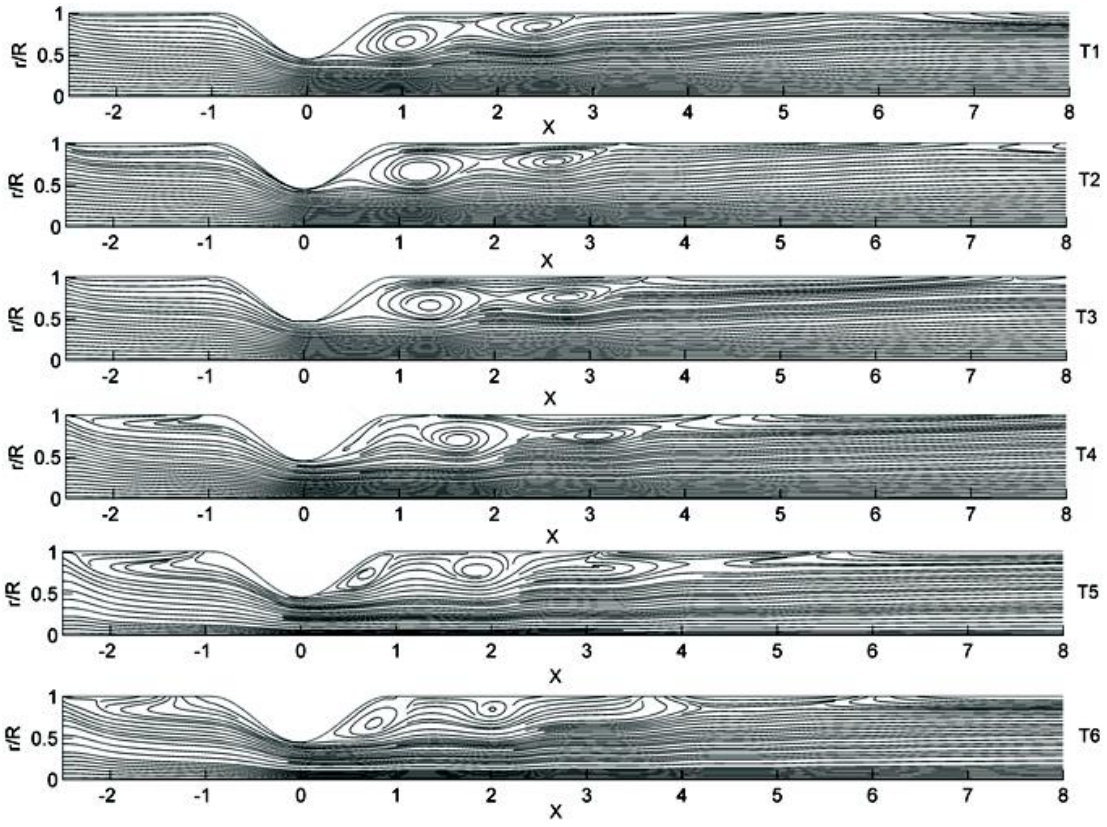

Figure 9.13 Streamline for the smooth stenosis from the present model at the different phases in the flow cycle.

Chapter 10: Conclusions and Future Work

10.1 Introduction

The axisymmetric lattice Boltzmann method is a relatively new CFD method based on the resolution of physics at a microscopic level. It is often used as a numerical simulation tool that is particularly suitable for simulate complex axisymmetric flows. This thesis aims to present the further power and capability the AxLAB® in modelling complicated axisymmetric flows. The main objectives of this study are to develop the AxLAB® to simulate axisymmetric rotation flows, turbulent flow and non-Newtonian fluid flows as well as more complex flows with complicated boundary conditions. To achieve this objective, the evolution of the lattice Boltzmann method (LBM) is reviewed firstly. Then the theory about the LBM for the axisymmetric flow equations (AxLAB®) is thoroughly studied. The numerical method is applied to a number of typical axisymmetric flow problems, including both laminar and turbulent cases. The numerical results are compared with either experimental data or analytical solutions. Based on the work, the following section presents the major contributions and findings.

10.2 Conclusions

In this thesis, the lattice Boltzmann method for axisymmetric flows, namely AxLAB® for laminar flow, AxLAB® are derived and discussed for non-Newtonian fluid flow and AxLAB® for turbulent flow respectively in detail. The popular two-dimensional nine velocities (D2Q9) lattice pattern is preferred as it is easier to use in numerical computations. Various boundary conditions are used in different tests. The most significant part of this thesis is the results analysis and comparison. From the analytical tests, it is found that when certain parameters of the models are adjusted, they generate stable results. Many simulation tests were done to verify this.

The key achievements and findings of the present study are summarized in the following paragraphs.

- AxLAB® Applications for Complex Laminar Flows

The numerical models were tested through a number of cases for which the analytical solution or experimental data were already known. The numerical results have shown a good accuracy and efficiency. After being validated, the models were implemented to several complex axisymmetric flow problems, including the steady cylindrical cavity flows, pulsatile 3D Womersley flow, the axisymmetric cold-flow jets and swirling flow in a cylinder with rotating top and bottom. In addition to the relatively new numerical theories of the AxLAB®, the numerical simulations of these cases with such type models have been originally presented in this thesis.

- Improvement of the AxLAB® for non-Newtonian Fluid Flows

The AxLAB® is extended to model the non-Newtonian fluid flows. Its accuracy is verified by simulating Newtonian and non-Newtonian Taylor-Couette flows, the combined effects of the Reynolds number, the radius ratio, and the power-law index n on the flow characteristics were analysed for an annular space of finite aspect ratio. From the comparisons with other literatures results, good agreements were obtained to prove the present model is stable and can be used to predict complex non-Newtonian fluid flows.

- Development of the AxLAB® for Turbulent Flows

Moreover, the AxLAB® is further developed to simulate the turbulent flows. The turbulent flow is efficiently and naturally simulated through incorporation of the standard subgrid-scale (SGS) stress model into the axisymmetric lattice Boltzmann equation in a consistent manner with the lattice gas dynamics. The model is verified by applying it to three typical cases in engineering. The numerical results obtained using the present methods are compared with experimental data and other available numerical solutions, indicating good agreements. This confirms that turbulence modelling based on a subgrid-scale stress model can provide more details than a time average turbulence model such as the $k-\omega$ model.

It is known that, lots of research used the axisymmetric LBM to simulate various flows but no one has developed and applied the models to simulate the turbulent flows especially the pulsatile blood flows in a stenotic vessel. This study suggests that LBM can also be a useful tool to study the blood flows and micro-tube flows. This study also demonstrates that AxLAB® can be used to study complex non-Newtonian fluid flows. In addition, a new simple boundary condition for the distribution function was used in the most simulation applications which also shown very good results.

10.3 Future Research

As one of the novel CFD methods, AxLAB® has not been explored comprehensively. It still requires further research to improve its modelling ability and calculation stability. Hence, the following suggestions can be made for improving and enhancing this model.

1. Further study on incompressible LBM is needed to improve the results of unsteady flows, since the compressibility of LBM model still affects the accuracy of the results especially for the unsteady flow cases.

2. The extension of this model would be to develop a multi-relaxation time formulation. This could be achieved either by adding the source terms to the right-hand side of main equation or by defining the moments of the generalised LBE such that the source terms are satisfied. Both procedures would be beneficial as they would enable the stability properties of the AxLAB® to be analysed in detail and allow the model to be extended to higher Reynolds number flows.

3. Simulate the turbulent non-Newtonian fluid flow. In chapter 8 and 9, the non-Newtonian fluid flow and turbulent flow were studied by improved AxLAB® separately. However, in practice, some axisymmetric flows are both turbulent and non-Newtonian fluids. As a result, the presented model needs to be extended into this situation for more practical engineering.

4. Parallel Computation and GPU Technique for AxLAB®. In order to simulate the real life complex axisymmetric flows, huge numbers of grid are needed. Therefore,

parallel computing and GPU technic are desirable for numerical simulation. With today's high performance graphic cards specialized in parallel computations, this will create opportunities to reach performance only possible with parallel supercomputers in the past. It is known that, one of most attractive advantages for the lattice Boltzmann method is the inherent feature of the parallel computation. It is recommended that parallel computation of above three models can be implemented in the future studies.

References

1. X. Chen, A three-dimensional hydrodynamic model for shallow waters using unstructured Cartesian grids. *International Journal for Numerical Methods in Fluids*, **66**(7): 885-905, 2011.
2. F. Rueda and S. Schladow, Quantitative Comparison of Models for Barotropic Response of Homogeneous Basins. *Journal of Hydraulic Engineering*, **128**(2): 201-213, 2002.
3. AGARD Report 787, Special Course on Unstructured Grid Methods for Advection Dominated Flows, France, 1992.
4. J. Y. Murthy and S.R. Mathur. Radiative heat transfer in axisymmetric geometries using an unstructured finite-volume method, *Numerical Heat Transfer Part B-Fundamentals*, **33**(4): 397-416, 1998.
5. P. R. M. Lyra, R de C.F. de Lima, C.S.C. Guimar ães, and D.K.E. de Carvalho, An edge-based unstructured finite volume procedure for the numerical analysis of heat conduction applications, *J. of the Braz. Soc. of Mech. Sci. & Eng.*, **26**(2): 160-169, 2004.
6. S. Wolfram. Statistical mechanics of cellular automata. *Rev. Mod. Phys*. 55:601-644, 1983.
7. A. Pires, D. P. Landau and H. Herrmann. *Computational Physics and Cellular Automata*. World Scientific, 1990.
8. B. Chopard and M. Droz. *Cellular Automata Modeling of Physical Systems.* Cambridge University Press, UK, 1998.
9. K. Zuse. *Calculating Space*. Technical Report, MIT Project MAC, AZT-70-164-GEMIT, 1970.
10. J. Hardy, Y. Pomeau and O. de Pazzis. Time evolution of a two-dimensional model system I. Invariant states and time correlation functions. *J. Math. Phys.*, **14**(2):1746–1759, 1973.
11. M. Gardner. The fantastic combinations of John Conway's new solitaire game of life. *Scientific American*, 220, 1970.
12. S. Wolfram. *Theory and Application of Cellular Automata*. World Scientific, 1986.
13. S. Wolfram. *Cellular Automata and Complexity*. Reading, MA, 1994.

14. J. G. Zhou. Lattice Boltzmann Methods for Shallow Water Flows. Springer, Berlin, Germany, 2004.
15. U. Frisch, B. Hasslacher and Y. Pomeau. Lattice-gas automata for the Navier-Stokes equation. *Phys. Rev. Lett.*, **56**(14):1505-1508, 1986.
16. B. Chopard and M. Droz. *Cellular Automata Modelling of Physical Systems*. Cambridge University Press, UK, 1998.
17. G. R. McNamara, G. Zanetti. Use of Lattice Boltzmann equation to simulate Lattice Gas Automata, *Physical Review Letters*, 1988.
18. S. Chen, G. D. Doolen. Lattice Boltzmann method for fluids flows. *Annual review of fluid mechanics*, 1998.
19. G. McNamara and G. Zanetti. Use of the Boltzmann Equation to Simulate Lattice-Gas Automata, *Phys. Rev. Lett.*, 61, 2332, 1988.
20. F. Higuera and J. Jimenez. Boltzmann Approach to Lattice Gas Simulations. *Europhys. Lett.*, 9, 663, 1989.
21. S. Succi. *The Lattice Boltzmann Equation for Fluid Dynamics and Beyond*, Oxford, London, 2001.
22. M. C. Sukop and D. T. J. Thorne. *Lattice Boltzmann Modelling: An Introduction for Geoscientists and Engineers*, Springer Verlag, Berlin, 2006.
23. Q. Chang and T. Yang. A Lattice Boltzmann Method for Image Denoising, *IEEE Trans. Image Proc.*18, 2797, 2009.
24. M. Mendoza, B. M. Boghosian, H. J. Herrmann, and S. Succi. Fast Lattice Boltzmann Solver for Relativistic Hydrodynamics, *Phys. Rev. Lett*.105, 014502, 2010.
25. M. R. Swift, W. R. Osborn and J. M. Yeomans. Lattice Boltzmann Simulation of Nonideal Fluids, *Phys. Rev. Lett.* 75, 830, 1995.
26. J. G. Zhou. A lattice Boltzmann model for the shallow water equations. *Computer Methods in Applied Mechanics and Engineering,* 191: 3527-3539, 2002.
27. J. G. Zhou. A rectangular lattice Boltzmann method for groundwater flows. *Modern Physics Letters B,* **21**(9): 531-542, 2007.
28. P. J. Love and C. Donato. From the Boltzmann equation to fluid mechanics on a manifold, *Proc. R. Soc. A,* 369, 2362-2370, 2011.

29. M. Mendoza, J.-D. Debus, S. Succi and H. J. Herrmann. Lattice kinetic scheme for generalized coordinates and curved spaces, *Int. J. Mod. Phys. C*, 25, 1441001, 2014.
30. A. Klales, D. Cianci, Z. Needell, D. A. Meyer and P. J. Love. Lattice gas simulations of dynamical geometry in two dimensions, *Phys. Rev. E*, 82, 046705, 2010.
31. M. Mendoza, S. Succi and H. J. Herrmann. Flow through Randomly Curved Manifolds, *Sci. Rep.* 3, 3106, 2013.
32. X. He and G. Doolen, Lattice Boltzmann method on curvilinear coordinates system: flow around a circular cylinder, *J. Comput. Phys.* 134, 306-315, 1997.
33. S. Y. Chen, D. Martinez, and R. W. Mei. On boundary conditions in lattice Boltzmann methods. Physics of Fluids, 8(9): 2527-2536, 1996.
34. K. N. Premnath and J. Abraham. Lattice Boltzmann model for axisymmetric multiphase flows, *Physical Review E*, **71**(5), 056706, 2005.
35. R. S. Maier, R. S. Bernard and D. W. Grunau. Boundary conditions for the lattice Boltzmann method, *Phys. Fluids* 8, 1788, 1996.
36. R. Mei, W. Shyy, D. Yu, L.-S. Luo. Lattice Boltzmann Method for 3-D Flows with Curved Boundary, *Journal of Computational Physics*, **161**(2):680-699, 2000.
37. A. M. Artoli, A. G. Hoekstra, and P. M. A. Sloot. 3D pulsatile flow with the lattice Boltzmann BGK method, *Int. J. Mod. Phys. C* 13, 1119, 2002.
38. J. M. Buick and C. A. Greated. Gravity in a lattice Boltzmann model, *Phys. Rev. E* 61, 5307, 2000.
39. Z. Guo, C. Zheng and B. Shi. Discrete lattice effects on the forcing term in the lattice Boltzmann method, *Phys. Rev. E*, 65, 046308, 2002.
40. L. S. Luo. Unified theory of lattice Boltzmann models for nonideal gases, *Phys. Rev. Lett.*81, 1618, 1998.
41. I. Halliday, A. L. Hammond, C. M. Care, K. Good, and A. Stevens. Lattice Boltzmann equation hydrodynamics, *Phys. Rev. E* 64, 011208, 2001.
42. Y. Peng, C. Shu, Y.T. Chew, J. Qiu. Numerical investigation of flows in Czochralski crystal growth by an axisymmetric lattice Boltzmann method, *Journal of Computational Physics*, **186**(1): 295-307, 2003.

43. X. D. Niu, C. Shu, and Y. T. Chew. An axisymmetric lattice Boltzmann model for simulation of Taylor-Couette flows between two concentric cylinders, *Int. J. Mod. Phys. C*, 14, 785, 2003.
44. T. S. Lee, H. Huang and C. Shu. An axisymmetric incompressible lattice BGK model for simulation of the pulsatile flow in a circular pipe, *International Journal for Numerical Methods in Fluids*, **49**(1):99-116, 2005.
45. T. S. Lee, H. Huang, and C. Shu. An axisymmetric incompressible lattice Boltzmann model for pipe flow, *Int. J. Mod. Phys. C*, 17, 645, 2006.
46. T. Reis and T. N. Phillips. Modified lattice Boltzmann model for axisymmetric flows, *Phys. Rev. E*, 75, 056703, 2007.
47. S. Chen, J. Tölke, and M. Krafczyk. Simulation of buoyancy-driven flows in a vertical cylinder using a simple lattice Boltzmann model, *Phys. Rev. E*, 79, 016704, 2009.
48. Z. Guo, H. Han, B. Shi and C. Zheng. Theory of the lattice Boltzmann equation: Lattice Boltzmann model for axisymmetric flows, *Phys. Rev. E*, 79, 046708, 2009.
49. Q. Li, Y. L. He, G. H. Tang, and W. Q. Tao. Improved axisymmetric lattice Boltzmann scheme, *Phys. Rev. E*, 81, 056707, 2010.
50. J. G. Zhou. Axisymmetric lattice Boltzmann method revised, *Physical Review E*, **84**(3), 036704, 2011.
51. J. G. Zhou. Axisymmetric lattice Boltzmann method, *Phys. Rev. E*, 78, 036701, 2008.
52. C. M. Teixeira. Incorporating Turbulence Models into the Lattice-Boltzmann Method, *Int. J. Mod. Phys. C*, 09, 1159, 1998.
53. J. Smagorinsky. General circulation experiments with the primitive equations I: the basic experiment. *Monthly Weather Review*, **91**(3):99-164, 1963.
54. M. Tutar, A. E. Hold. Computational modelling of flow around a circular cylinder in sub-critical flow regime with various turbulence models. *International Journal for Numerical Methods in Fluids*, 35:763-784, 2001.
55. S. Hou, J. Sterling, S. Chen, G. D. Doolen. A lattice Boltzmann subgrid model for high Reynolds number flows. *Fields Institute Communications*, 6, 151-166, 1996.
56. J. G. Zhou. A lattice Boltzmann model for the shallow water equations with turbulence modelling. *Int. J. Mod. Phys. C*, **13** (8):1135-1150, 2002.

57. H. Liu, M. Li and A. P. Shu. Large eddy simulation of turbulent shallow water flows using multi-relaxation-time lattice Boltzmann model, *Int. J. Numer. Meth. Fluids*, 70:1573-1589, 2012.
58. C. Golia and N. A. Evans. Flow separation through annular constrictions in tubes - From an experimental investigation, correlations have been obtained for the onset of separation and length of the separation zone caused by a symmetric, stenosis-type constriction in tube flow, *Exper. Mech*. 157, 1973.
59. C. Clark. The fluid mechanics of aortic stenosis--I. Theory and steady flow experiments. *J. Biomech.*, 9, 521, 1976.
60. C. Clark. The fluid mechanics of aortic stenosis - II. Unsteady flow experiments, *J. Biomech*., 9, 567, 1976.
61. K. D. Stephanoff, Ian J. Sobey and B. J. Bellhouseet. On flow through furrowed channels. Part 2. Observed flow patterns, *J. Fluid Mech*., 96, 27, 1980.
62. J. C. F. Chow and K. Soda. Laminar Flow in Tubes with Constriction, *Phys. Fluids*, 15, 1700, 1972.
63. R. T. Cheng. Numerical Solution of the Navier-Stokes Equations by the Finite Element Method, *Phys. Fluids*, 15, 2098, 1972.
64. J. S. Lee and Y. C. Fung. Flow in locally constricted tubes at low Reynolds numbers, *J. Appl. Mech.*, 37, 9, 1970.
65. L. C. Cheng, M. E. Clark and J. M. Robertson. Numerical calculations of oscillating flow in the vicinity of square wall obstacles in plane conduits. *J. Biomech.*, 5, 467, 1972.
66. D. F. Young and F. Y. Tsai. Flow characteristics in models of arterial stenoses. I. Steady flow, *J. Biomech.*, 6:395-410, 1973a.
67. A. M. Artoli, A. G. Hoekstra, P. M. Sloot, Accuracy of 2D Pulsatile flow in the lattice Boltzmann BGK method, *Lecture notes in computer science*, 2329:361-370, 2002.
68. J. A. Cosgrove, J. M. Buick, S. J. Tonge, C. G. Munro, C. A. Greated and D. M. Campbell. Application of the lattice Boltzmann method to transition in oscillatory channel flow. *J. Phys. A: Math. Gen*, 36, 2609, 2003.
69. A. M. Artoli, D. Kandhai, H. C. J. Hoefsloot, A. G. Hoekstra, P. M. A. Sloot. Lattice BGK simulations of flow in a symmetric bifurcation, *Future Generation Computer Systems*, **20**(6):909-916, 2004.

70. M. Bouzidi, M. Firdaouss and P. Lallemand. Momentum transfer of a Boltzmann-lattice fluid with boundaries, *Phys. Fluids*, **13**(11):3452-3459, 2001.
71. N. Beratlis, E. Balaras, B. Parvinian and K. Kiger. A numerical and experimental investigation of transitional pulsatile flow in a stenosed channel, *J Biomech Eng* **127**(7):1147-1157, 2005.
72. J. Chen and X. Y. Lu. Numerical investigation of the non-Newtonian pulsatile blood flow in a bifurcation model with a non-planar branch, Journal of Biomechanics, **39**(5):818-832, 2006.
73. M. X. Li, J. J. Beech-Brandt, L. R. John, P. R. Hoskins, W. J. Easson. Numerical analysis of pulsatile blood flow and vessel wall mechanics in different degrees of stenoses, *Journal of Biomechanics*, **40**(16): 3715-3724, 2007.
74. H. Fang, Z. Lin, and Z. Wang. Lattice Boltzmann simulation of viscous fluid systems with elastic boundaries, *Phys. Rev. E* 57, R**25**(R), 1998.
75. Z. Guo, C. Zheng and B. Shi. An extrapolation method for boundary conditions in lattice Boltzmann method, *Phys. Fluids*, 14:2007-2010, 2002.
76. H. P. Fang, Z.W. Wang, Z. F. Lin and M. R. Liu. Lattice Boltzmann method for simulating the viscous flow in large distensible blood vessels, *Physical Review E*, 65, 051925, 2002.
77. J. M. Lopez. Axisymmetric vortex breakdown Part 1. Confined swirling flow. *Journal of Fluid Mechanics*, 221, 533- 552, 1990.
78. A. Y. Gelfgat, P. Z. Bar-Yoseph and A. Solan. Three-dimensional instability of axisymmetric flow in a rotating lid-cylinder enclosure, *Journal of Fluid Mechanics*, 438: 363- 377, 2001.
79. H. U. Vogel. Experimentelle Ergebnisse ber die laminare Strmung in einem zylindrischen Gehuse mit darin rotierender Scheib, MPI Bericht 6, 1968.
80. B. Ronnenberg. Ein selbstjustierendes 3-Komponenten-Laserdoppleranemometer nach dem Vergeichsstrahlvefahren, angewandt auf Untersuchungen in einer stationaren zylinder- sym- metrischen Drehstr̈omung mit einen R̈uckstr̈omgebiet. *Max-Planck-Institut f̈ur Str̈omungsfors- chung G̈ottingen, Bericht*,19, 1977.
81. M.P. Escudier. Observations of the flow produced in cylindrical container by a rotating end wall, *Experiments in Fluids*, **2**(4):189-196, 1984.

82. A. Spohn, M. Mory and E. J. Hopfinger. Experiments on vortex breakdown in a confined flow generated by a rotating disk, *Journal of Fluid Mechanics*, 370: 73-99, 1998.
83. F. Sotiropoulos, D. R. Webster and T. C. Lackey. Experiments on Lagrangian transport in steady vortex-breakdown bubbles in a confined swirling flow, *Journal of Fluid Mechanics*, 466: 215- 248, 2002.
84. G. L. Brown and J. M. Lopez. Axisymmetric vortex breakdown. Part 2. Physical mechanisms, *Aerodynamics Report* 174, Melbourne, Victoria.
85. J. M. Lopez and A. D. Perry. Axisymmetric vortex breakdown, Part 3: Onset of periodic flow and chaotic advection, *Journal of Fluid Mechanics*, 234:449-471, 1992.
86. F. Sotiropoulos and Y. Ventikos. The three-dimensional structure of confined swirling flows with vortex breakdown, *J. Fluid Mech.*, 426:155-175, 2001.
87. F. Sotiropoulos, Y. Ventikos and T. C. LACKEY. Chaotic advection in three-dimensional stationary vortex-breakdown bubbles: Sil'nikov's chaos and the devil's staircase, *Journal of Fluid Mechanics*, 444:257- 297, 2001.
88. K. G. Roesner. *Recirculation zones in a cylinder with rotating lid*. In Proceedings of the IUTAM Symposium on Topological Fluid Mechanics edited by A. Tsinober and H. K. Moffat University of Cambridge, Cambridge, 699, 1989.
89. G. Gautier, P. Gondret, F. Moisy and M. Rabaud. Instabilities in the flow between co- and counter-rotating disks, *Journal of Fluid Mechanics*, 473, 1-21, 2002.
90. K. Fujimura, H. S. Koyama and J. M. Hyun. An experimental study on vortex breakdown in a differentially-rotating cylindrical container, *Experiments in Fluids*, **36**(3):399-407, 2004.
91. D. T. Valentine and C. C. Jahnke. Flows induced in a cylinder with both walls rotating, *Phys. Fluids* 6, 2702, 1994.
92. J. M. Lopez. Unsteady swirling flow in an enclosed cylinder with reflection symmetry, *Phys. Fluids* 7, 2700, 1995.
93. G. I. Taylor. Stability of a Viscous Liquid Contained between Two Rotating Cylinders, *Phil. Trans. R. Soc. Lond. A*, 223, 289-343, 1923.
94. T. B. Benjamin. Bifurcation Phenomena in Steady Flows of a Viscous Fluid. I. Theory, *Proc. R. Soc. Lond. A*: 359, 1-26, 1978.

95. T. B Benjamin. Bifurcation Phenomena in Steady Flows of a Viscous Fluid. II. Experiments, *Proc. R. Soc. Lond. A:* 359 27-43, 1978.
96. R. C. DiPrima, P. M. Eagles and B. S. Ng. The effect of radius ratio on the stability of Couette flow and Taylor vortex flow, *Phys. Fluids*, 27, 2403, 1984.
97. M. Yoshino, Y. Hottaa, T. Hirozanea, M. Endob. A numerical method for incompressible non-Newtonian fluid flows based on the lattice Boltzmann method, *Journal of Non-Newtonian Fluid Mechanics*, **147**(1-2): 69-78, 2007.
98. D. Wang and J. Bernsdorf. Lattice Boltzmann simulation of steady non-Newtonian blood flow in a 3D generic stenosis case, *Computers & Mathematics with Applications,* **58**(5):1030-1034, 2009.
99. H. Huang, T. S. Lee and C. Shu, Hybrid lattice Boltzmann finite-difference simulation of axisymmetric swirling and rotating flows, *International Journal for Numerical Methods in Fluids*, **53**(11):1707-1726, 2007.
100. H. Huang, Z. Li, S. Liu and X. Lu, Shan-and-Chen-type multiphase lattice Boltzmann study of viscous coupling effects for two-phase flow in porous media, *International Journal for Numerical Methods in Fluids*, **61**(3):341-354, 2009.
101. H. Huang, Theoretical and numerical study of axisymmetric lattice Boltzmann models, *Phys. Rev. E* 80, 016701, 2009.
102. H. Huang. Lattice–BGK simulation of steady flow through vascular tubes with double constrictions, *International Journal of Numerical Methods for Heat & Fluid Flow*, **16**(2): 185-203, 2006.
103. H. Huang, Lattice Boltzmann method simulation gas slip flow in long microtubes, I*nternational Journal of Numerical Methods for Heat & Fluid Flow*, **17**(6): 587-607, 2007.
104. X. He and L. S. Luo, Lattice Boltzmann Model for the Incompressible Navier–Stokes Equation, *Journal of Statistical Physics*, **88**(3-4): 927-944, 1997.
105. H. An, C. Zhang, J. Meng, Y. Zhang. Analytical solution of axi-symmetrical lattice Boltzmann model for cylindrical Couette flows, *Physica A: Statistical Mechanics and its Applications*, 391, 8-14, 2012.
106. H. Tennekes and J. Lumley. *A First Course in Turbulence*. The MIT Press. Cambridge, Massachusetts, and London, England, 1972.

107. O. Reynolds. An experimental investigation of the circumstances which determine whether the motion of water shall be direct or sinuous, and of the law of resistance in parallel channels, *Philosophical Transactions of the Royal Society of London*, 174:935-982, 1883.

108. J. D. Sterling and S. Chen, Stability Analysis of Lattice Boltzmann Methods, *Journal of Computational Physics*, **123**(1): 196-206, 1996.

109. R. Benzi, S. Succi and M. Vergassola, The lattice Boltzmann equation: theory and applications, *Phys. Reports*, 222: 145-197, 1993.

110. Y. H. Qian and S. A. Orszag, Lattice BGK Models for the Navier-Stokes Equation: Nonlinear Deviation in Compressible Regimes, *Europhys. Lett.*, 21:255, 1993.

111. M. Krafczyk, J. Tölke, and L.-S. Luo, Large-eddy simulations with a multiple-relaxation-time LBE model, *Int. J. Mod. Phys. B* 17, 33, 2003.

112. H. Yu, L. S. Luo and S. S. Girimaji, LES of turbulent square jet flow using an MRT lattice Boltzmann model, *Computers & Fluids*, **35**(8-9):957-965, 2006.

113. J. Boussinesq. Théorie de l'Écoulement Tourbillant. *Mem. Présente par Divers Savants Acad. Sci. Inst. Fr.*, 23:46-50, 1877.

114. D. C. Wilcox. *Turbulence Modeling for CFD*. DCW Industries, Inc., California, U.S, 3 edition, 2004.

115. B. E. Launder and D. B. Spalding, The numerical computation of turbulent flows, *Computer Methods in Applied Mechanics and Engineering*, **3**(2): 269-289, 1974.

116. C. D. Scott-Pomerantz. *The k-epsilon model in the theory of turbulence*. PhD thesis, University of Pittsburgh, 2004.

117. B. E. Launder, G. J. Reece, and W. Rodi. Progress in the development of a Reynolds-stress turbulent closure. *Journal of Fluid Mechanics*, **68**(3):537-566, 1975.

118. F. J. Higuera and J. Jimenez. Boltzmann approach to lattice gas simulations. *Euro physics Letters.* **9** (7):663, 1989.

119. D. R. Noble, S. Chen, J. G. Georgiadis, R. O. Buckius. A consistent hydrodynamic boundary condition for the lattice Boltzmann method. *Physics of Fluids.* **7**(1):203, 1995.

120. V. V. Titov and C. E. Synolakis. Modeling of breaking and nonbreaking long-wave evolution and runup using VTCS-2. *Journal of Waterway, Port, Coastal & Ocean Engineering - ASCE.* **121**(6):308-316, 1995.

121. D. R. Fuhrman and P. A. Madsen. Simulation of nonlinear wave runup with a high-order Boussinesq model. *Coastal Engineering*. **55**(2):139-154, 2008.

122. P. L. Bhatnagar, E. P. Gross and M. Krook. A model for collision processes in gases. i:small amplitude processes in charged and neutral one-component system. *Phys. Rev*. **94**:511, 1954.

123. J. M. V. A. Koelman. A simple lattice Boltzmann scheme for Navier-Stokes fluid flow. *Europhys. Lett.,* **15**(6):603-607, 1991.

124. Y. H. Qian. *Lattice gas and lattice kinetic theory applied to the Navier-Stokes equations*. PhD thesis, University of Marie Curie, Paris, 1990.

125. P. A. Skordos. Initial and boundary conditions for the lattice Boltzmann method. *Physical Review E,* 48:4823-4842, 1993.

126. J. G. Zhou. An elastic-collision scheme for lattice Boltzmann methods. *International Journal of Modern Physics C,* **12**(3):387-401, 2001.

127. U. Frisch, D. d'Humieres, B. Hasslacher, P. Lallemand, Y. Pomeau, and J. P. Rivet. Lattice gas hydrodynamics in two and three dimensions. *Complex Systems,* 1:649-707, 1987.

128. X. He and L.-S. Luo. A priori derivation of lattice Boltzmann equation. *Physical Review E,* 55:R6333-R6336, 1997.

129. D. H. Rothman and S. Zaleske. *Lattice-Gas Cellular Automata*. Cambridge University Press, London, 1997.

130. T. Toffoli and N. Margolus. Invertible cellular automata: A review. *Physica D,* 45:229-253, 1990.

131. H. Chen, S. Chen, and W. H. Matthaeus. Recovery of the Navier-Stokes equations using a lattice-gas Boltzmann method. *Phys. Rev. A.,* 45:R5539-42, 1992.

132. G. W. Yan. A lattice Boltzmann equation for waves. *J. Comp.Phys.*, 161:61-69, 2000.

133. S. Chen, J. Tölke, S. Geller, and M. Krafczyk. Lattice Boltzmann model for incompressible axisymmetric flows, *Phys. Rev. E* 78, 046703, 2008.

134. S. Ponce Dawson, S. Chen and G. D. Doolen. Lattice Boltzmann computations for reaction-diffusion equations, *J. Chem. Phys*. 98, 1514, 1993.

135. J. G. Zhou. A lattice Boltzmann method for solute transport, *International Journal for Numerical Methods in Fluids*, **61**(8):848-863, 2009.

136. J. D. Sterling and S. Chen. Stability Analysis of Lattice Boltzmann Methods. *Journal of Computational Physics*, **123**(1): 196-206, 1996.

137. S. Khali, R. Nebbali. Numerical investigation of non-Newtonian fluids in annular ducts with finite aspect ratio using lattice Boltzmann method, *Physical Review E*, 87, 053002, 2013.

138. H. Liu. *Lattice Boltzmann simulations for complex shallow water flows*, University of Liverpool, PhD thesis, 2009.

139. D. R. Noble, S. Chen, J. G. Georgiadis and R. O. Buckius. A consistent hydrodynamic boundary-condition for the lattice Boltzmann method. *Physics of Fluids*, **7**(1):203-209, 1995.

140. Q. S. Zou and X. Y. He. On pressure and velocity boundary conditions for the lattice Boltzmann BGK model. *Physics of Fluids*, **9**(6): 1591-1598, 1997.

141. Z. L. Guo, C. G. Zheng and B. C. Shi. Non-equilibrium extrapolation method for velocity and pressure boundary conditions in the lattice Boltzmann method. *Chinese Physics*, **11**(4): 366-374, 2002.

142. O. Filippova, and D. Hänel. Grid Refinement for Lattice-BGK Models. *Journal of Computational Physics*, **147**(1): 219-228, 1998.

143. M. Bouzidi, M. Firdaouss and P. Lallemand. Momentum transfer of a Boltzmann-lattice fluid with boundaries. *Physics of Fluids*, **13**(11): 3452-3459, 2001.

144. P. A. Skordos. Initial and boundary conditions for the lattice Boltzmann method. *Physical Review E*, **48**(6): 4823-4842, 1993.

145. I. Ginzburg and D. d'Humières. Multire flection boundary conditions for lattice Boltzmann models. *Physical Review E*, **68**(6): 066614, 2003.

146. M. S. Ghidaoui, J. Q. Deng, W. G. Gray and K. Xu. A Boltzmann based model for open channel flows. *Int. J. Numer. Methods Fluids*, **35**(4): 449-494, 2001.

147. F. H. Harlow and J. E. Welch. Numerical calculation of time dependent viscous incompressible flow of fluid with free surface. *Physics of Fluids*. **8**(12): 2182-2189, 1965.

148. D. Yu, R. Mei, L. Luo and W. Shyy. Viscous flow computations with the method of lattice Boltzmann equation. *Progress in Aerospace Sciences*. **39** (5):329, 2003.

149. C. Pan, L. Luo, C. T. Miller. An evaluation of lattice Boltzmann schemes for porous medium flow simulation. *Computers & Fluids*. **35** (8):898-909, 2006.

150. A. J. C. Ladd. Numerical simulation of particular suspensions via a discretized Boltzmann equation. Part 2. Numerical results. *J. Fluid Mech*., 271:311-339, 1994.

151. J. F. Douglas, J. M. Gasiorek, J. A. Swaffield. *Fluid Mechanics*. Harlow, Longmans Scientific, 1995.

152. J. G. Zhou and I. M. Goodwill. A finite volume method for steady state 2D shallow water flows. *International Journal of Numerical Methods for Heat and Fluid Flow*. **7**(1):4-23, 1997.

153. Z. Guo, C. Zheng and B. Shi. Non-equilibrium extrapolation method for velocity and pressure boundary conditions in the Lattice Boltzmann method, *Chinese Phys.*, **11**(4): 366-74, 2002.

154. F. M. White, *Fluid Mechanics*, 4th ed., McGraw-Hill, Boston, 1999.

155. K. M. Smith, L. C. Moore and H. E. Layton. Advective transport of nitric oxide in a mathematical model of the afferent arteriole. *Am. J. Physiol. Renal. Physiol.* 284, F1080-F1096, 2003.

156. H. Huang, T.S. Lee and C. Shu. Lattice-BGK simulation of steady flow through vascular tubes with double constrictions, *International Journal of Numerical Methods for Heat & Fluid Flow*, **16**(2): 185-203, 2006.

157. Q. Zou and X. He. On pressure and velocity boundary conditions for the Lattice Boltzmann BGK model. *Phys. Fluids*, **9**(6): 1591-1598, 1997.

158. Q. Li, Y. L. He, G. H. Tang, and W. Q. Tao. Improved axisymmetric lattice Boltzmann scheme, *Phys. Rev. E* 81, 056707, 2010.

159. K. Fujimura, H. Yoshizawa, R. Iwatsu, and H. Koyama. Velocity Measurements of Vortex Breakdown in an Enclosed Cylinder, *J. Fluids Eng*, **123**(3): 604-611, 2001.

160. S. Bhaumik and K. Lakshmisha. Lattice Boltzmann simulation of lid-driven swirling flow in confined cylindrical cavity, *Comput. Fluids*, 36:1163-1173, 2007.

161. V. V. Barve, O. A. Ezekoye, and N. T. Clemens. Numerical study of evolution of strongly forced axisymmetric laminar cold-flow jets, *AIAA Journal*, **44**(8), 2006.

162. S. I. Pai and T. Hsieh. Numerical Solution of Laminar Jet Mixing With and Without Free Stream, *Applied Scientific Research*, **27**(1): 39-62, 1972.

163. W. Z. Shen, J. Nørkær Sørensen and J. A. Michelsen. Numerical study of swirling flow in a cylinder with rotating top and bottom, *Physics of Fluids,* 18, 064102, 2006.

164. A. Y. Gelfgat, P. Z. Bar-Yoseph, and A. Solan. Steady state and oscillatory instability of swirling flow in a cylinder with rotating top and bottom. *Phys. Fluids*, **8**: 2614, 1996.

165. M. F. White. Fluid Mechanics, 3rd edn, McGraw-Hill. New York, US, 1994.

166. Y. Liu. *Numerical simulation of flows in Czochralski crystal growth and Taylor vortices*. M. Eng. Thesis, National University of Singapore, 1998.

167. F. Nygård-H. I. Andersson. Numerical Simulation of Turbulent Pipe Flow Through an Abrupt Axisymmetric Constriction. *Flow Turbulence Combust*, 91, 1-18, 2013.

168. A. B. Wang. *Strömungen in Röhren mit ringformigem Hindernis.* PhD thesis, Der Technischen Fakultät der Universität Erlangen-Nürnberg, 1991.

169. H. Rastgou, S. Saedodin. Numerical simulation of an axisymmetric separated and reattached flow over a longitudinal blunt circular cylinder, *Journal of Fluids and Structures*, 42: 13-24, 2013.

170. T. Ota. An axisymmetric separated and reattached flow on a longitudinal blunt circular cylinder. *Journal of Applied Mechanics*, 42, 311-315, 1975.

171. M. Kiya, O. Mochizuki, T. Tamura, R. Ishikawa. Turbulence properties of an axisymmetric separation-and-reattaching flow. *AIAA Journal, 29,* 936-941, 1991.

172. S. A. Ahmed and D. P. Giddens. Pulsatile poststenotic flow studies with laser Doppler anemometry, *J. Biomech*., 17:695-705, 1984.

173. S. S. Varghese and S. H. Frankel. Numerical Modelling of Pulsatile Turbulent Flow in Stenotic Vessels, *Journal of Biomechanical Engineering*, 125:445-460, 2003.